MUSCULOSKELETAL MODELING OF THE HUMAN ELBOW JOINT

A DISSERTATION IN
Engineering
and
Mathematics

Presented to the Faculty of the University
of Missouri – Kansas City in partial fulfillment of
the requirements for the degree

DOCTOR OF PHILOSOPHY

by
MUNSUR RAHMAN

M.S., University of Missouri-Kansas City, 2013

Kansas City, Missouri
2017

MUSCULOSKELETAL MODELING OF THE HUMAN ELBOW JOINT

Munsur Rahman, Candidate for the Doctor of Philosophy Degree

University of Missouri – Kansas City, 2017

ABSTRACT

Comprehensive knowledge of the *in vivo* loading of elbow structures is essential in understanding the biomechanical causes associated with elbow diseases and injuries, and to find appropriate treatment. Currently, in vivo measurements of ligament, and muscle forces, and cartilage contact pressures during elbow activities is not possible. Therefore, computational models needs to be employed for prediction. A dynamic computational model in which muscle, ligament and articular surface contact forces are predicted concurrently would be the ideal tool for patient specific pre-operative planning, computer-aided surgery and rehabilitation. Computational models of the elbow have been developed to study joint behavior, but all of these models have limited applicability because the joint structure was modeled as an idealized joint (e.g. hinge joint) rather than a true anatomical joint. Three dimensional studies of elbow passive motion showed that the elbow does not function as a simple hinge joint. An accurate elbow model should reflect the intrinsic laxity of the elbow especially for clinical applications. Presented here are methods for developing an anatomically based computational model of the human elbow joint that replicates the mechanical behavior of the joint and is capable of concurrent prediction of articular contact, ligament, and muscle forces under dynamic conditions. The model performance was evaluated in both a cadaveric study and a living human subject experiment. The validated models were then used to investigate the effects of medial and lateral collateral ligament deficiency on elbow joint kinematics, ligament loads, and articular contact pressure distribution.

The faculty listed below, appointed by the Dean of the School of Graduate Studies, have examined the dissertation titled “Musculoskeletal Modeling of The Human Elbow Joint,” presented by Munsur Rahman, candidate for the Doctor of Philosophy degree, and certify that in their opinion it is worthy of acceptance.

Supervisory Committee

Antonis P. Stylianou, Ph.D., Committee Chair and Discipline Advisor
Department of Civil & Mechanical Engineering

Majid Bani-Yaghoub, Ph.D., Co-discipline Advisor
Department of Mathematics and Statistics

Ganesh Thiagarajan, Ph.D.
Department of Civil & Mechanical Engineering

Gregory W. King, Ph.D.
Department of Civil & Mechanical Engineering

Naveen K. Vaidya, Ph.D.
Department of Mathematics and Statistics

TABLE OF CONTENTS

LIST OF ILLUSTRATIONS

LIST OF TABLES

ACKNOWLEDGMENTS

The projects were partially funded by the Franklin D. Dickson endowment from School of Medicine, and from School of Graduate Studies research grant program, University of Missouri- Kansas City (UMKC).

I would like to acknowledge many people who have helped and provided support for me during this project. To begin with my advisor Dr. Stylianou, who has provided a great opportunity to work in the Musculoskeletal Biomechanics Research Laboratory and enabled me to have a fulfilling research experience. He opened the door to a subject that I have become passionate about. His guidance, support, and wisdom have also been indispensable. I would also like to acknowledge Dr. Akin Cil for his support and guidance to successfully finish this research. I would like to thank Dr. Trent Guess and Dr. Mahbube K Siddiki for their contribution to this project. I want to thank my lab partners Mohsen Sharifi Renani and Jonathan Parman for helping troubleshoot problems.

Finally, I would also like to thank my wife Mashruba for her unwavering support and care throughout this process.

CHAPTER 1

INTRODUCTION

This manuscript presents a synopsis of elbow anatomy and four separate studies involving the computational modeling of the human elbow joint. The chapter 2 describes the anatomy of the elbow joint including the bones, ligaments, joint capsule, and musculature surrounding the joint, followed by the biomechanics of the joint. This chapter provides some basic ideas about the terminology of elbow joint anatomy along with their functions that would be helpful throughout the manuscript.

The published study in Chapter 3 presents the advanced technique of computational multibody model development to calculate the contact pressure distribution of elbow joint during dynamic conditions. Computational multibody musculoskeletal models of the elbow joint that are capable of simultaneous and accurate predictions of muscle and ligament forces, along with cartilage contact mechanics can be immensely useful in clinical practice. As a step towards producing a musculoskeletal model that includes the interaction between cartilage and muscle loading, the goal of this study was to develop subject- specific multibody models of the elbow joint with discretized humerus cartilage representation interacting with the radius and ulna cartilages through deformable contacts. The contact parameters for the compliant contact law were derived using simplified elastic foundation contact theory. The elbow joint was constraint by non-linear ligaments that include the ligament wrapping around the bony structures. The models were then validated by placing the model in a virtual mechanical tester for flexion-extension motion similar to a cadaver experiment, and the resulting kinematics were compared. Two cadaveric upper limbs were used in this study. The humeral heads were subjected to axial motion in a mechanical tester and the resulting kinematics from three bones were recorded for model validation. After model validation, a lateral ulnar collateral ligament (LUCL) deficient condition was simulated and, contact pressures and kinematics were compared to the intact elbow model.

The published study in Chapter 4 presents the modeling technique to investigate the effects of lateral collateral ligament deficiency on elbow joint kinematics, ligament loads, and articular contact pressure distribution. A computational model capable of predicting the effects of lateral collateral ligament deficiency of the elbow joint would be a valuable tool for surgical planning and prediction of the long-term consequences of ligament deficiency. The purpose of this study was to simulate lateral collateral ligament deficiency during passive flexion using a computational multibody elbow joint model and investigate the effects of ligament insufficiency on the kinematics, ligament loads and articular contact characteristics (area, pressure). The elbow was placed initially at approximately 20° of flexion and a 345 mm vertical downward motion profile was applied over 40 seconds to the humerus head. The vertical displacement induced flexion from the initial position to a maximum flexion angle of 135°.The study included simulations for intact, radial collateral ligament deficient, lateral ulnar collateral ligament deficient, and combined radial and lateral ulnar collateral ligament deficient elbow. For each condition, relative bone kinematics, contact pressure, contact area, and intact ligament forces were predicted.

Chapter 5 presents the subject specific computer modeling technique to investigate the effect of medial collateral ligament deficiency on elbow joint stability. Computational elbow joint models capable of simulating medial collateral ligament deficiency can significantly improve surgical efficiency through analysis of virtual surgeries of ligament reconstruction strategies. The goal of this project was to investigate the effect of medial collateral ligament deficiency on elbow joint stability in subject specific computer models. Two subject specific joint models were passively flexed by applying a vertical downward motion on the humeral head that induced the final joint flexion of about 135^0 for both specimens. The motion profile was identical for all simulations. This project investigated the condition of intact, isolated medial collateral ligament anterior bundle deficiency, isolated medial collateral ligament posterior bundle deficiency, and entire medial collateral ligament deficiency. For each simulated condition, relative bone kinematics, contact characteristics (area, pressure), and intact ligament forces were computed.

Chapter 6 presents the study of developing the three-dimensional musculoskeletal model of the human elbow joint. Detailed knowledge of the in-vivo loading of elbow structures is essential in understanding the biomechanical causes associated with both chronic (degenerative joint disease) and acute injuries, and for improving design, and implementation of therapeutic interventions. Since direct measurement of the in-vivo joint loads is not feasible, computational models have to be implemented for predictions. This study developed the computational musculoskeletal model of the human elbow joint where the joint was constrained by multiple ligament bundles and deformable articular cartilage contacts. The model was verified by comparing the bone kinematics of a muscle driven forward dynamics with a motion driven inverse kinematics. The muscle activation patterns were also compared to experimental data. The validated model can be used for better understanding of biomechanics and tissue function of the elbow joint, along with the subject specific intervention strategies aimed at modifying upper extremity movement for targeted outcomes, such as reducing articular cartilage stress. Furthermore, the validated model can be used to analyze the biomechanical consequences of surgical reconstructive procedures and can be used for patient-specific preoperative planning, or rehabilitation. In this way, it can mitigate the need for large sample sizes in clinical trials, and can work at a fraction of the cost of cadaveric models.

Chapter 7 provides a discussion of this manuscript, as well as conclusion and future directions for this research.

CHAPTER 2

BACKGROUND

2.1 Elbow anatomy

Upper extremity function depends largely on the elbow joint. The elbow joint serves as a link in the lever arm system that produces the complex motions of the forearm needed for positioning and orienting the hand in three-dimensional space. Careful examination of elbow anatomy is important to understand the significant influences of various components on joint structure and behavior. The effect of the elbow structure is exceptionally prominent since it makes the elbow joint one of the most congruous joints in the body (Alcid, Ahmad, & Lee, 2004). The anatomical structures of the elbow that govern and affect elbow motion are discussed in details such as osteology (bony structures), ligaments, capsules, and muscle.

2.1.1 Osteology

As the most important joint of the upper extremity (Alcid et al., 2004), the elbow joint complex incorporates all three long bones of the arm; humerus, radius, and ulna (Fig. 2.1a). The bones form three articulations between them: the ulnohumeral, radiohumeral, and proximal radioulnar articulations (Fig. 2.1b). These articulations allow the elbow joint for its complex motion of flexion-extension and forearm rotation (pronation-supination).

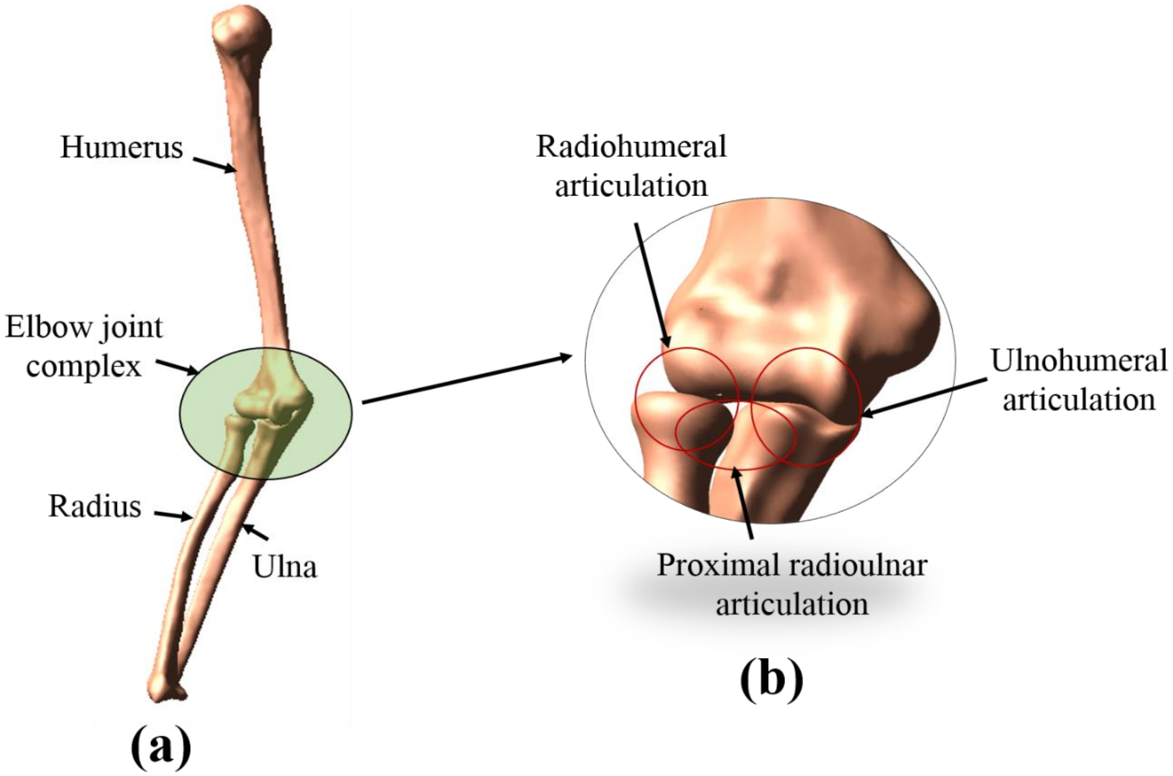

Figure 2.1. (a) The view of right upper extremity, and (b) the articulations of elbow joint.

2.1.1.1 Humerus

The humerus is the longest bone of the upper arm and is associated with articulation of both the shoulder and elbow joint. The distal humerus contains many intricate structures necessary for elbow function. The distal humerus widens on both sides inferiorly and forms medial and lateral epicondyles (Fig. 2.2). The more prominent medial epicondyle serves as a source of attachment sites for the medial ulnar collateral ligaments and flexor-pronator group of the muscle. The lateral ulnar collateral ligament and the supinator-extensor muscle group are attached to the irregular surface of the lateral epicondyle.

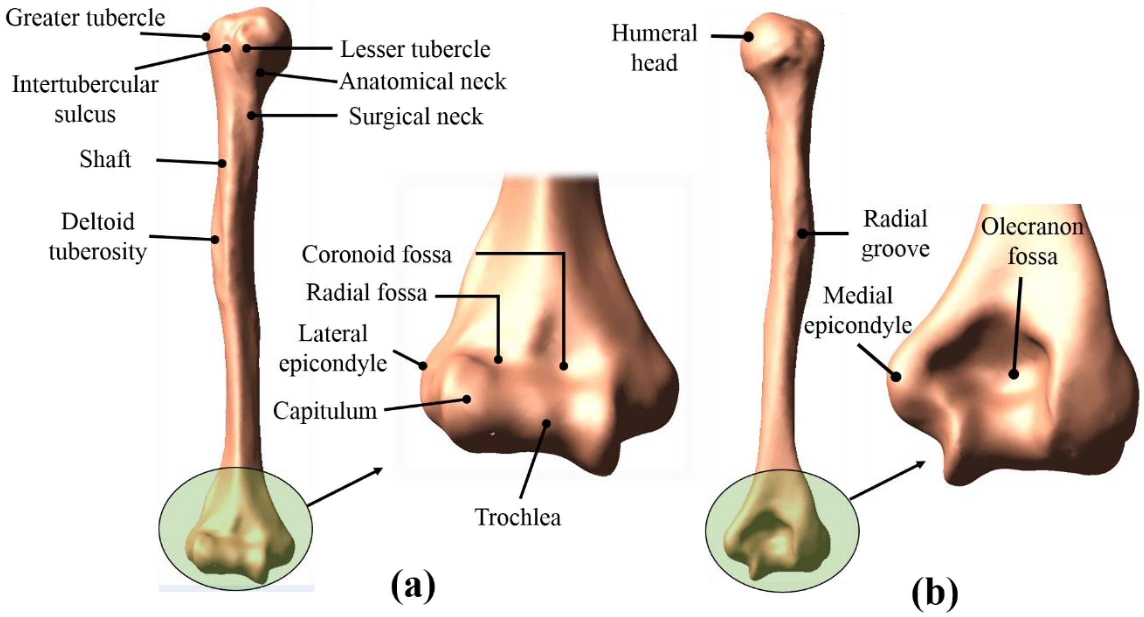

Figure 2.2. Osteology of the humerus. (a) Anterior, and (b) posterior view of the right arm.

Adjacent to the medial epicondyle is the spool-shaped surface of the trochlea (Fig. 2.2). The trochlea surface articulates with the greater sigmoid notch of the ulna and is covered by 300^0 of articular cartilage (Chuang, Wu, Lin, & Lur, 2012; Morrey, 2000). The trochlea surface has a circular cross-section in the sagittal plane containing the trochlear sulcus at the center. The trochlear sulcus with the medial and lateral lips form a track that provides an articular bearing surface for flexion-extension motion and keeps the greater sigmoid notch of the ulna centered. Lateral to the trochlea is the nearly half sphere shape structure of the capitulum that provides the articulation with the concave dish of the radial head. The capitulum is covered with articular cartilage by approximately 180^0 (Ferreira, 2011) and provides a bearing for both elbow flexion-extension and forearm pronation-supination. The two grooved structures located superior to the trochlear and the capitulum are called the coronoid fossa and radial fossa respectively. These fossae provide clearance for the coronoid process and the radial head at elbow high flexion. The big depression region on the posterior distal humerus is the olecranon fossa that provides clearance of the ulna’s olecranon at high elbow extension.

The humerus shaft is cylindrical at the proximal end, and becomes wedge shaped distally and contains some important bony landmarks such as the deltoid tuberosity, the radial groove, and muscle attachment sites (Fig. 2.2). The deltoid tuberosity is the rough surface on the lateral side of the humerus shaft and works as an attachment site of the deltoid muscle. The shallow depression region that runs diagonally down the posterior surface of the humerus and parallel to the deltoid tuberosity, is called the radial groove. This groove works as a passage for the radial nerve and the profunda brachii artery. The humeral head is a complexly contoured half spheroid shape and is covered with articular hyaline cartilage that articulates with the scapula to form the shoulder joint. The humeral head, anatomical and surgical neck, greater and lesser tubercles, and intertubercular sulcus are the important anatomical features of the proximal humerus. These sites are significantly important for the attachment of muscles and ligaments.

2.1.1.2 Radius

Structures of the proximal radius include several crucial features that are necessary for proper elbow operation. At its most proximal aspect is the discoid-shaped radial head, which is secured to the ulna by the annular ligament (Fig.2.3). Distal to the radial head, the bone tapers and forms the radial neck. The bony outcropping distal to the radial neck is the radial tubercle that serves as the insertion site for the biceps tendon (Morrey, 2000). The axis of the radial head and the adjacent neck make a 15^0 angle with the radius shaft and orient in a direction opposite to the radial tuberosity (Morrey, 2000).The proximal radial head is a concave structure and forms a shallow cup, called the radial dish. The radial dish is fully enveloped with articular cartilage and provides articulation with the capitulum to allow elbow flexion-extension and forearm pronation-supination. The circumference of the radial head is also covered with hyaline cartilage by 240^0 (Ferreira, 2011). This cartilage contributes to articulation with the lesser sigmoid notch of the proximal ulna and forms the proximal radioulnar joint.

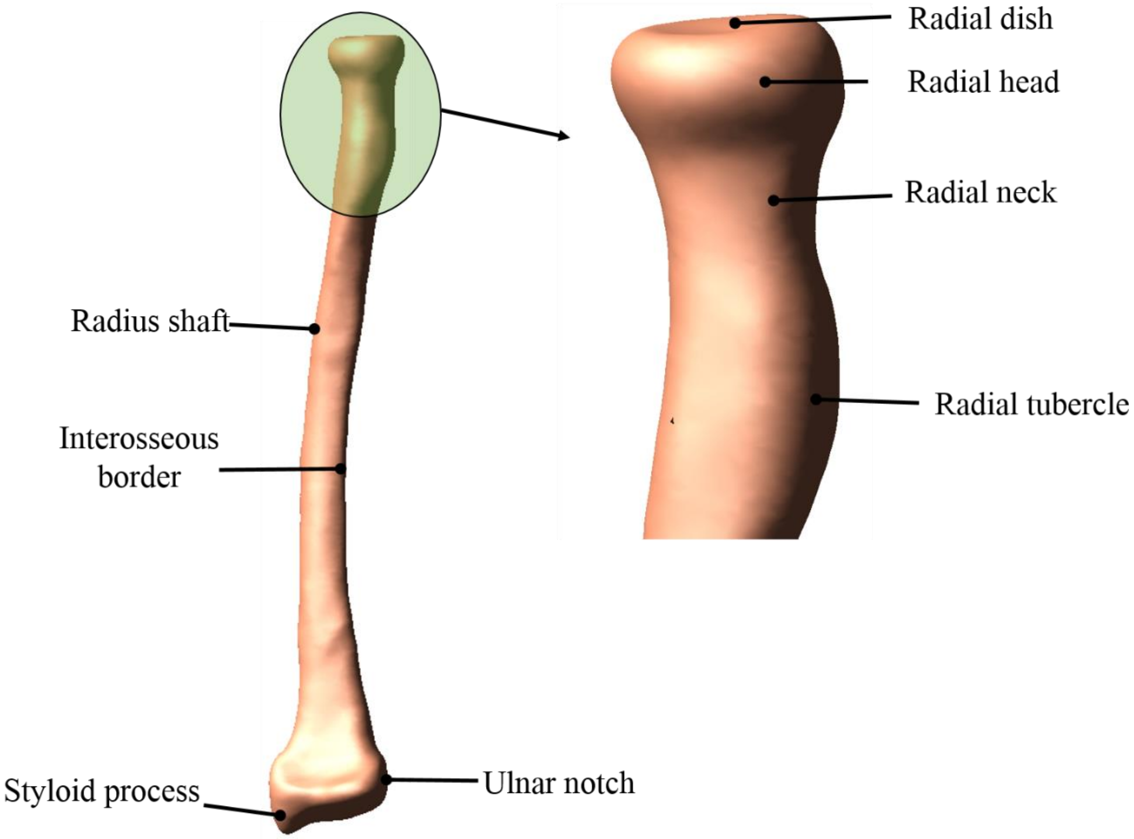

Figure 2.3. Osteology of the radius. Anterior view is shown of the right arm.

Elbow function is also influenced by skeletal features of the distal radius (Fig.2.3). The radius shaft is triangular in cross section and the shaft diameter increases as it runs distally. The radius runs parallel to the ulna to the distal end where they form the wrist joint. Interosseous margin areas are located at the medial boundaries of the supinated radius and serve as an attachment site of the interosseous membrane. At the distal end of the radius, the bone extends laterally to form the radius styloid process. The styloid process provides attachments for the ligaments of the wrist. At the medial surface of the distal end, the concavity is called the ulnar notch which articulates with the head of the ulna, forming the distal radioulnar joint.

2.1.1.3 Ulna

The proximal ulna also has many significant structures for proper elbow function. Most superiorly, the ulna bone comes forward and forms an approximating beak like structure which is called the olecranon process (Fig. 2.4). The posterior aspect of the olecranon process serves as the insertion site of the triceps tendon. Distal from the olecranon process, the anteriorly extended surface is called coronoid process. The cortical surfaces of the coronoid process serve as insertion sites for the brachialis muscle and the oblique cord. The olecranon and coronoid process fit into their corresponding fossae during full elbow flexion and extension. The cartilage enveloped region of the proximal ulna is divided into two articular surfaces; the greater and lesser sigmoid notch. The guiding ridge of the greater sigmoid notch fits into the track of the trochlear sulcus of the humerus and generates articulations with the distal humerus. The lesser sigmoid notch has 60-80° of articular cartilage that articulates with the radial head to form the proximal radioulnar joint (PRUJ) to enhance the forearm pronation-supination (Ferreira, 2011). Medial to the greater sigmoid notch is the sublime tubercle that serves as an attachment site for the medial collateral ligament. Distal to the lesser sigmoid notch is the supinator crest and a tuberosity that serves as attachment to the supinator muscle, and the lateral ulnar collateral ligament respectively.

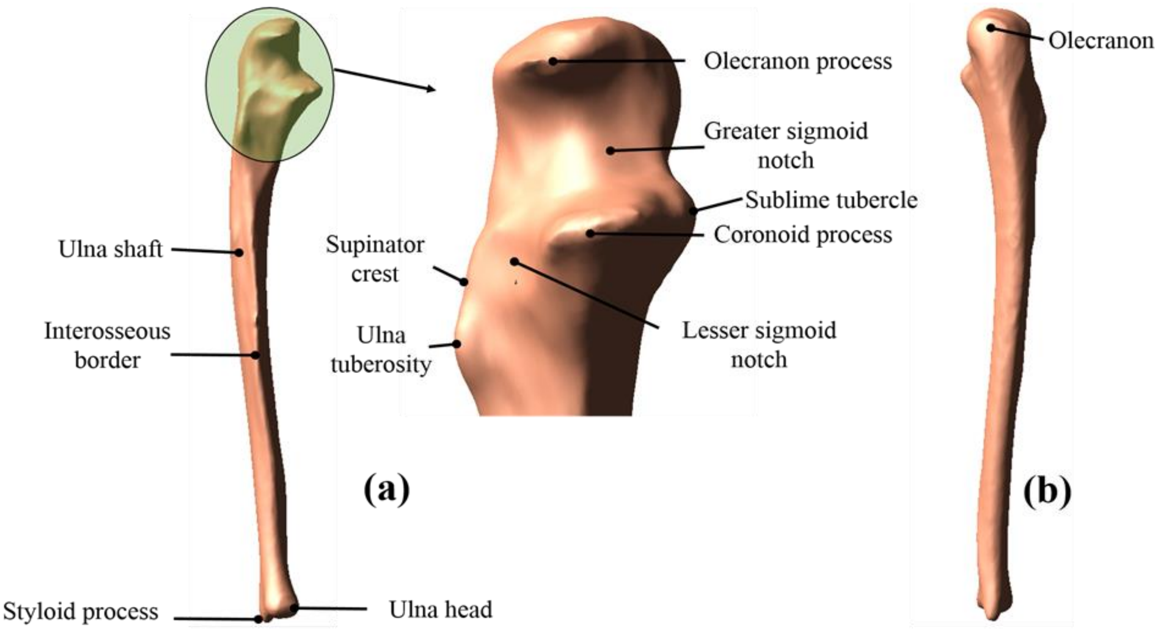

Figure 2.4. Osteology of the ulna. (a) Anterior and (b) Posterior view of the right arm

The diaphysis shaft of the ulna is triangular in cross section and runs almost parallel to the radius (Fig. 2.4). The diaphysis shaft has three borders and three surfaces and the diameter of the shaft decreases as it moves distally. The three surfaces are anterior, posterior, and medial and work as attachment sites for many muscles of the lower arm. The three borders are posterior, anterior, and interosseous. Where the posterior border is substantial along the entire length of the forearm posteriorly, the anterior border is unremarkable. The Interosseous surface is located at the lateral boundaries of the ulna diaphysis and serves as attachment sites of interosseous membrane. The distal ulna is much smaller in diameter than the proximal ulna and terminates at its small distal head known as ulnar styloid process. The styloid process of the ulna provides attachments for ligaments of the wrist. At the distal end, the cartilage covered knoblike head articulates laterally with a notch on the radius and forms the distal radioulnar joint. This joint, together with the proximal radioulnar joint, provides articulation for forearm rotational motion.

2.1.2 Ligaments

The bony structures of the elbow joint are restrained and stabilized by other passive structures. Predominantly, the medial and lateral collateral ligaments are two major ligamentous structures that contribute to primary stabilization of the elbow. The forearm is largely stabilized by the interosseous membrane between the ulna and radius. Distal radioulnar ligaments, located at distal radioulnar joint, can also influence elbow behavior.

The medial collateral ligament (MCL) complex consists of three segments: the anterior, posterior, and transverse bundle (M. S. Cohen & Bruno, 2001; Fuss, 1991; Morrey & An, 1985). The anterior bundle of the MCL is the most discrete component that originates from the medial epicondyle of the humerus and attaches to the sublime tubercle on the coronoid process of the ulna (Fig. 2.5). The posterior bundle also originates from the humerus medial epicondyle, however, its ulnar attachments are much broader. Though the attachment site is less defined, it generally inserts more distally onto the medial aspect of the olecranon. The width of the anterior bundle is about 4 to 5mm where the posterior bundle width is about 5 to 6mm at the mid portion of its fan-shaped structure. The anterior and posterior bundles of the medial collateral ligament have a substantial effect on joint stability in response to valgus movement. It also plays a significant role in limiting elbow flexion and extension. The transverse ligament bundle originates and attaches to the ulna only, and so far has no known function (Morrey, 2000).

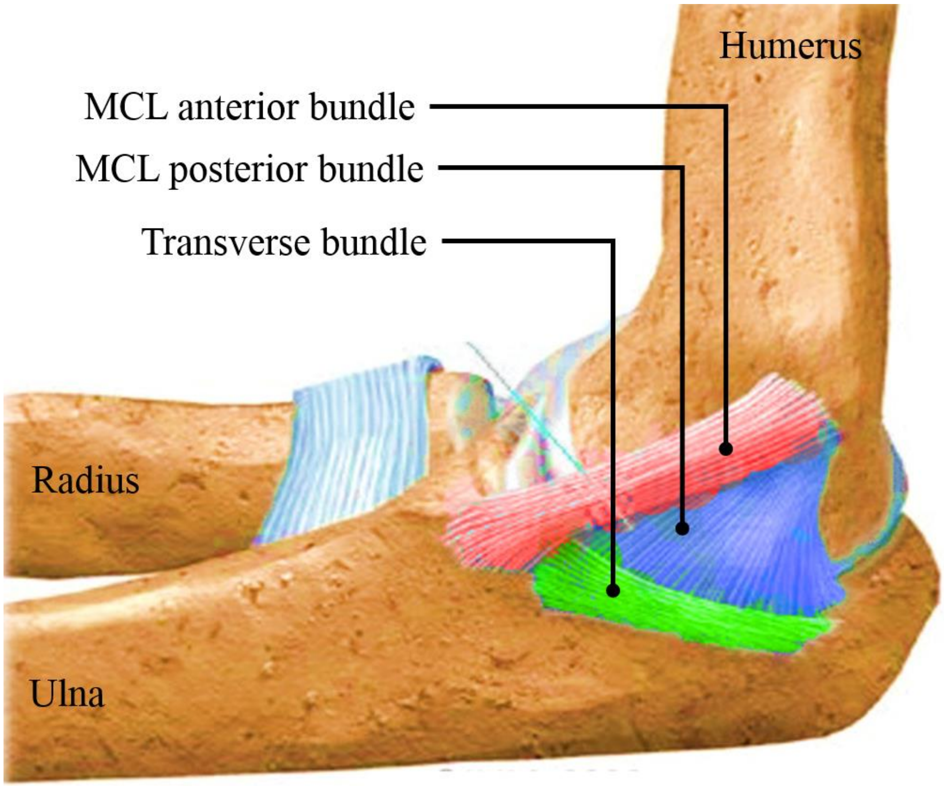

Figure 2.5. Medial collateral ligament complex.

The lateral collateral ligament (LCL) is less discrete in structure and generally varied among individuals. Typically four components make up the LCL complex: (i) lateral ulnar collateral ligament (LUCL), (ii) a variably present accessory lateral collateral ligament, (iii) radial collateral ligament (RCL), and (iv) annular ligament (Morrey, 2000;

Morrey & An, 1985). The overall shape of the complex is considered to be roughly 'Y' where the arms are attach to the anterior and posterior aspect of the semilunar notch (Fig. 2.6). The lateral ulnar collateral ligament originates from the lateral epicondyle of the humerus, and inserts in the crista supinatorum tubercle of the ulna and superficially blends with the annular ligament. The variable accessory lateral collateral ligament attaches to the crista supinatorum and blends proximally with the distal lateral rim of the annular ligament (Morrey, 2000). The radial collateral ligament originates from the lateral epicondyle of the humerus, fans out at its distal end, and blends with the lateral portion of the annular ligament. The ring-shaped annular ligament attaches to the anterior rim of the lesser sigmoid notch, wraps around approximately 80% of the radial head and attaches to the posterior rims of the lesser sigmoid notch (Fisk, 2007).

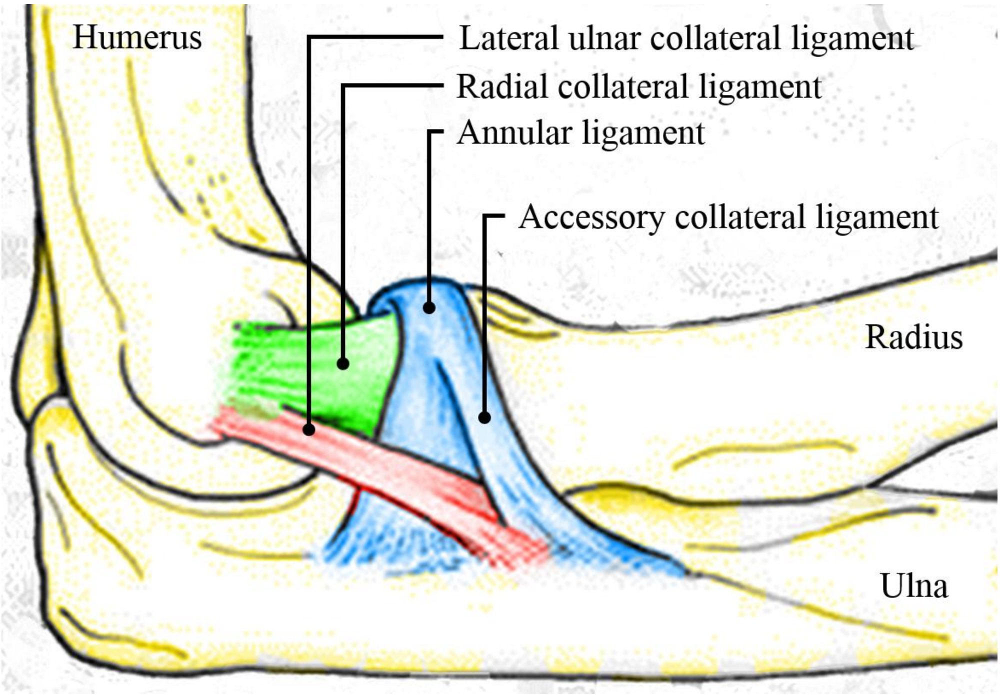

Figure 2.6. Lateral collateral ligament complex.

The interosseous membrane (IOM) is the sturdy thin collagenous sheet that usually attaches on the interosseous borders of the radius and ulna (Fig. 2.7). It consists of several bands: proximal band, central band, accessory bands, and distal membranous band (McGinley & Kozin, 2001; Skahen, Palmer, Werner, & Fortino, 1997). Other than the proximal band, all interosseous membrane bands run distally and medially from their radial origins to their ulnar insertions. The fiber bands make an average 21^0 angle with the long axis of the ulna (Skahen et al., 1997). The proximal band is an oblique structure that attaches proximally to the ulna and distally to the radius. The central band shares the insertion with proximal band and is approximately twice as thick as other bands (Amis, Dowson, & Wright, 1979). Several other bands are located inferior to the central band; distal to these bands are areas of membranous tissue. Researchers have suggested that the interosseous membrane also acts as a stabilizer of the distal radioulnar joint (Schuind et al., 1991).

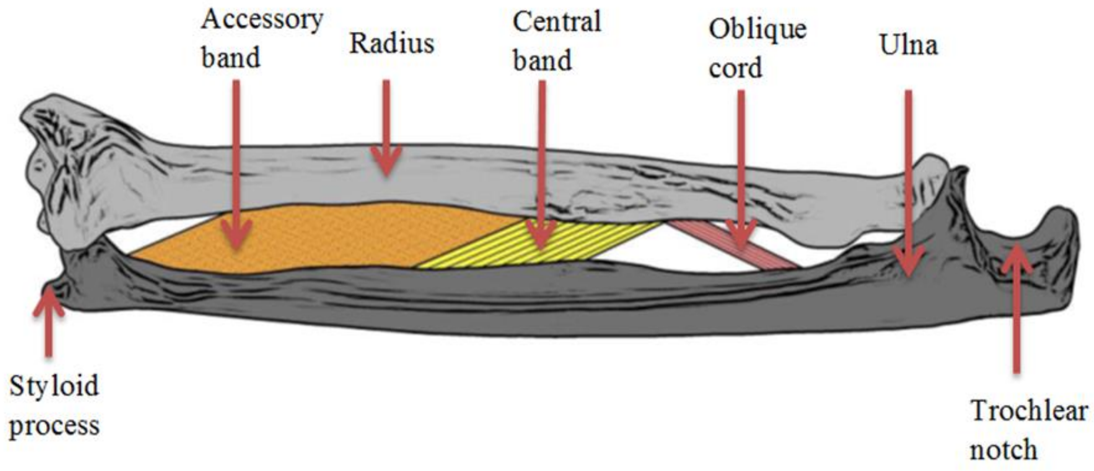

Figure 2.7. Interosseous membrane of the forearm (Fisk, 2007).

Ligaments are viscoelastic (An, 2005), making the ligament mechanical characteristics dependent on the direction of load and also on loading rate. Each ligament bundle has fibers oriented in different directions according to the primary tensile force. The collateral ligaments are heterogeneous structures which are composed of a combination of collagen and elastin that provide stability of the ligament in various directions.

2.1.3 Elbow joint capsule

The single soft tissue structure of the elbow joint capsule covers all three articulations of the joint. The capsule is normally thin transparent structure, but integrating with the ligament provides significant strength in transverse and oblique directions. The anterior joint capsule inserts proximally above the coronoid and radial fossae, and distally to the anterior margin of the coronoid medially as well as to the annular ligament laterally (Fig. 2.8). The anterior joint capsule encapsulates the radial head, radial neck, and coronoid process (Ferreira, 2011). Posteriorly, the capsule attaches just above the olecranon fossa distally along the supracondylar bony column, and around the perimeter of the olecranon process of the ulna. The posterior joint capsule encloses the olecranon fossa of the humerus (Morrey, 2000). The joint capsule works as a secondary static elbow stabilizer and the greatest contribution occurs with the elbow extended (de Haan et al., 2011). Morrey and An (1983) reported that the anterior and posterior capsule provide 32% varus and 33% valgus elbow stability respectively at full extension.

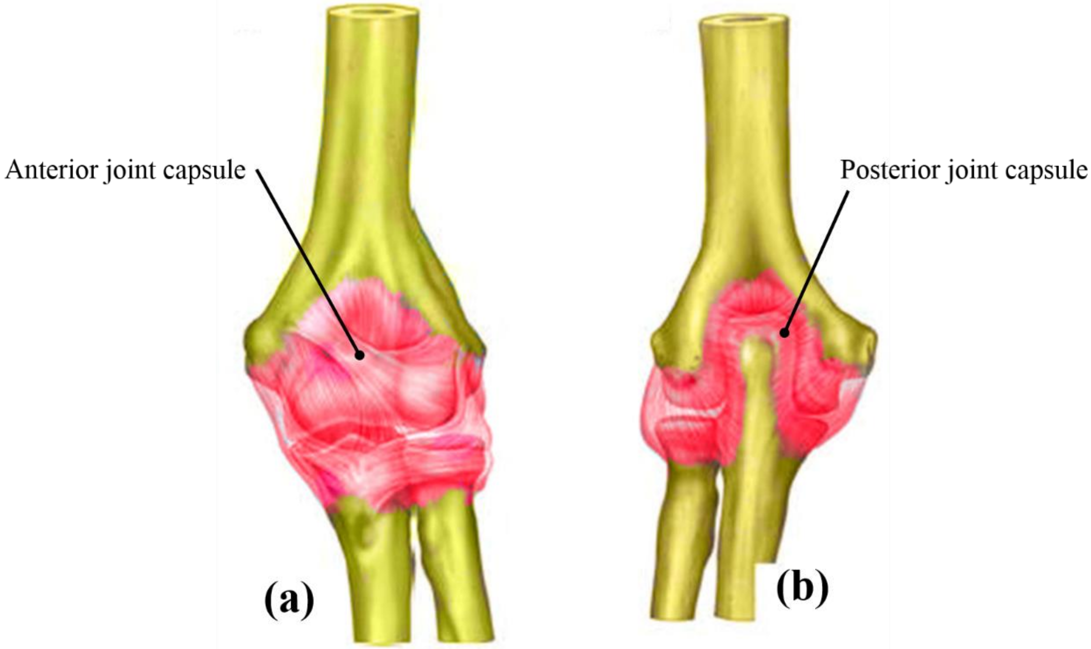

Figure 2.8. Joint capsule of the elbow joint. (a) Anterior and, (b) posterior view of the left arm (Cavalheiro et al., 2015).

2.1.3 Muscle anatomy

Twenty four distinct muscles cross the elbow joint and these muscles originate from the distal humerus and insert on the forearm and hand (Morrey, 2000; Pigeon, Yahia, & Feldman, 1996). These muscles produce flexion-extension, forearm pronation-supination, and flexion-extension of the wrist and fingers. Although all of the muscles are essential for proper elbow function, only a select subset of muscles that significantly influence elbow operation will be discussed here.

2.1.3.1 Elbow Flexors

Biceps brachii, brachialis, and brachioradialis are the three muscles that cross the elbow joint to generate flexion moment (Fig 2.9). The biceps brachii has two origins (its name is derived from the Latin word biceps which means “two heads”) and positioned more superficially on the anterior aspect of the upper arm. The long head originates from the superior glenoid tubercle of the scapula and wraps around the humeral head and runs down to the intertubercular sulcus of the humerus. The short head originates from the apex of the coronoid process of scapula and blends with the long head approximately 7 centimeters proximal to the elbow to form a single tendon which inserts at the bicipital tuberosity of the proximal radius (Fisk, 2007). The biceps brachii has a distinct large cross section and insertion on the medial aspect of the radius, as a result, the biceps works as a powerful forearm supinator. Particularly, when the forearm is supinated, biceps brachii works as a significant elbow flexor and has an intermediate mechanical advantage since it passes relatively close to the axis of rotation (Shiba et al., 1988). The brachialis originates broadly on the anterior, distal half of the humerus and converges to insert more discretely on the ulnar tuberosity and base of the coronoid process. The muscle also has a large cross sectional area, but has poor mechanical advantage since it crosses very close to the joint axis of rotation. The brachioradialis originates from the lateral supracondylar ridge of the humerus and inserts distally at the radial styloid (Morrey, 2000). The origin separates the lateral head of the triceps from the brachialis muscle. Brachioradialis has the longest moment arm of elbow flexion, but due to its small cross section, the brachioradialis works as the weakest of the three flexor muscles (Hotchkiss, An, Sowa, Basta, & Weiland, 1989; Murray, Delp, & Buchanan, 1995; Shiba et al., 1988).

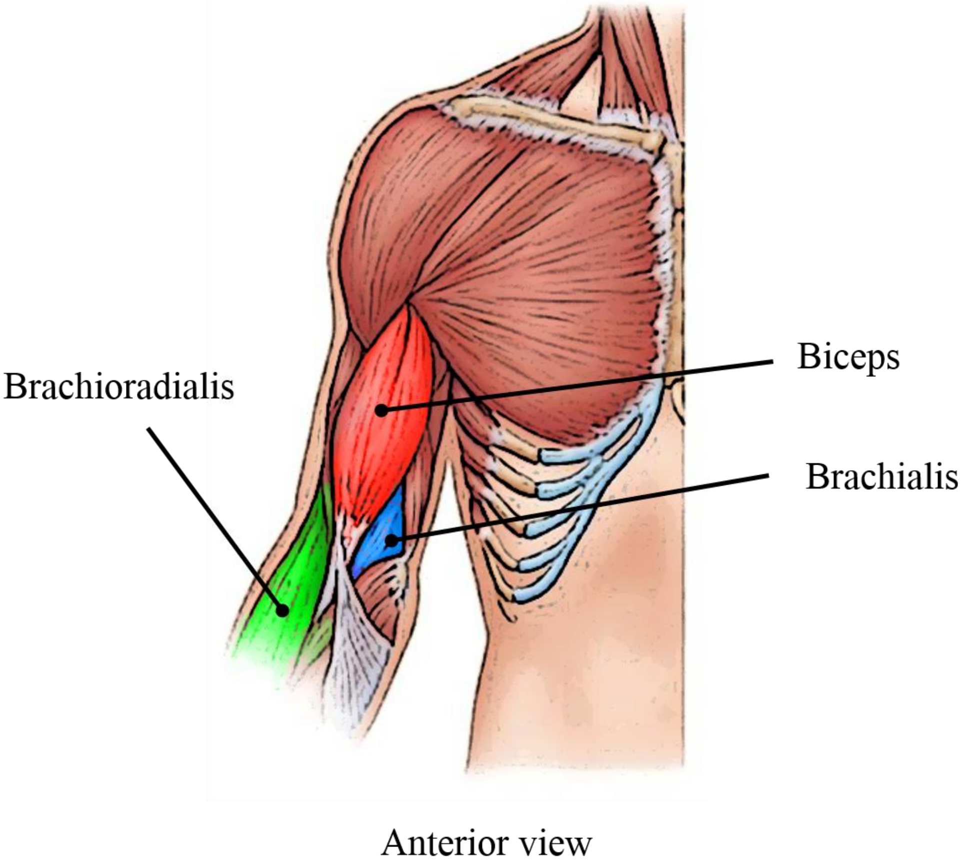

Figure 2.9. Major muscles produce elbow flexion (Marieb & Hoehn, 2013).

2.1.3.2 Elbow Extensor

The triceps is the only muscle that generates elbow extension moment (Fig. 2.10). It covers the entire posterior musculature of the arm. It has three heads, as its name implies. The long head has the most medial attachment and originates from the scapula at the infraglenoid tubercle. The lateral head originates on the lateral intermuscular septum and passes along a thin linear strip superior to the radial groove. The medial head has a broad origin and attaches to the posteromedial humeral shaft and medial intermuscular septum. Thus each head originates distal to each other and has progressively larger area of origin. In proximal direction, all three heads begin to converge in the middle of the muscle and ultimately merge to form a single large tendon that inserts at the olecranon process of the ulna (Morrey, 2000).

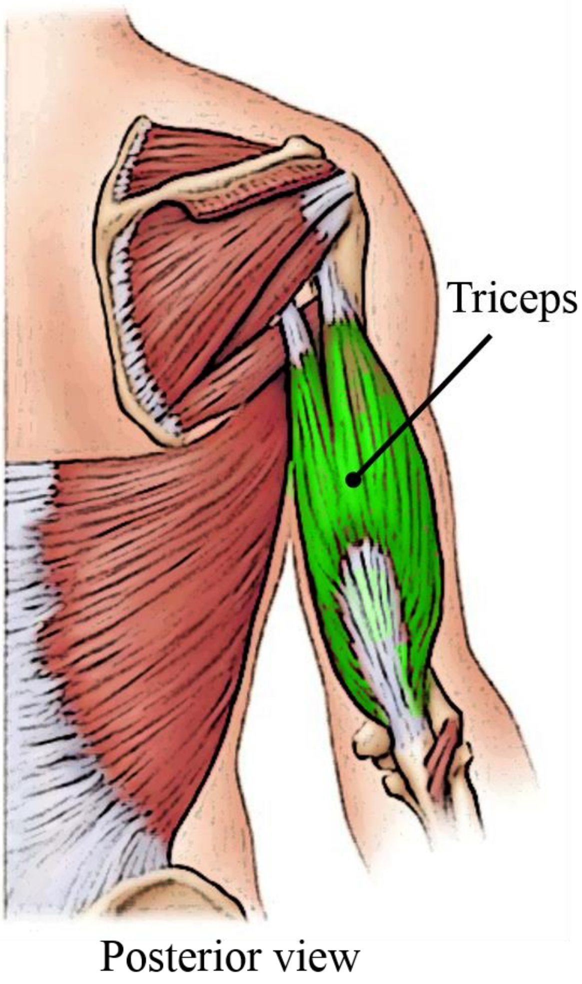

Figure 2.10. Major muscles produce elbow extension (Marieb & Hoehn, 2013).

2.1.3.3 Elbow Pronator

Forearm pronation is generated by two muscle groups: the pronator teres and the pronator quadratus (Fig. 2.11). The pronator teres has two heads of origins, the largest one arises from the anterosuperior aspect of the medial epicondyle and the other one is at the coronoid process of the ulna. The muscle proceeds beneath the brachioradialis radially and distally, inserting at the junction of middle and proximal thirds of the radius by a discrete board tendinous insertion into a tuberosity on the lateral aspect of the bone. It is a strong pronator, but considered a weak flexor of the elbow joint (Morrey, 2000). The pronator quadratus is a square shaped short muscle that running from the most distal quarter of the anterior ulna to the distal quarter of the radius. It has two heads: the superficial head originates at the anterior distal ulna and inserts at the anterior distal radius. The deep head has the same origin, but inserts proximal to the ulnar notch. It is a weak pronator, however, it provides stability through compression of the distal radioulnar joint (Gordon, Kedgley, Ferreira, King, & Johnson, 2006; Morrey, 2000)

2.1.3.4 Elbow supinator

Elbow supination is also generally created by two muscle groups: the biceps brachii and the supinator. Because of the large cross-sectional area and the medial insertion on the radius, the biceps works as a strong supinator in the pronated position. The supinator is a broad muscle in the posterior compartment of the forearm and wraps laterally around the proximal ulna to its broad insertion on the posterior aspect of the proximal radius (Morrey, 2000)(Fig. 2.11). The supinator originates from the three sites above and below the elbow: (i) the anterolateral aspect of the lateral epicondyle, (ii) the lateral collateral ligament, and (iii) the crista supinatorum of the ulna. This muscle is not as strong supinator as the biceps brachii, but its effectiveness is not altered by the position of elbow flexion.

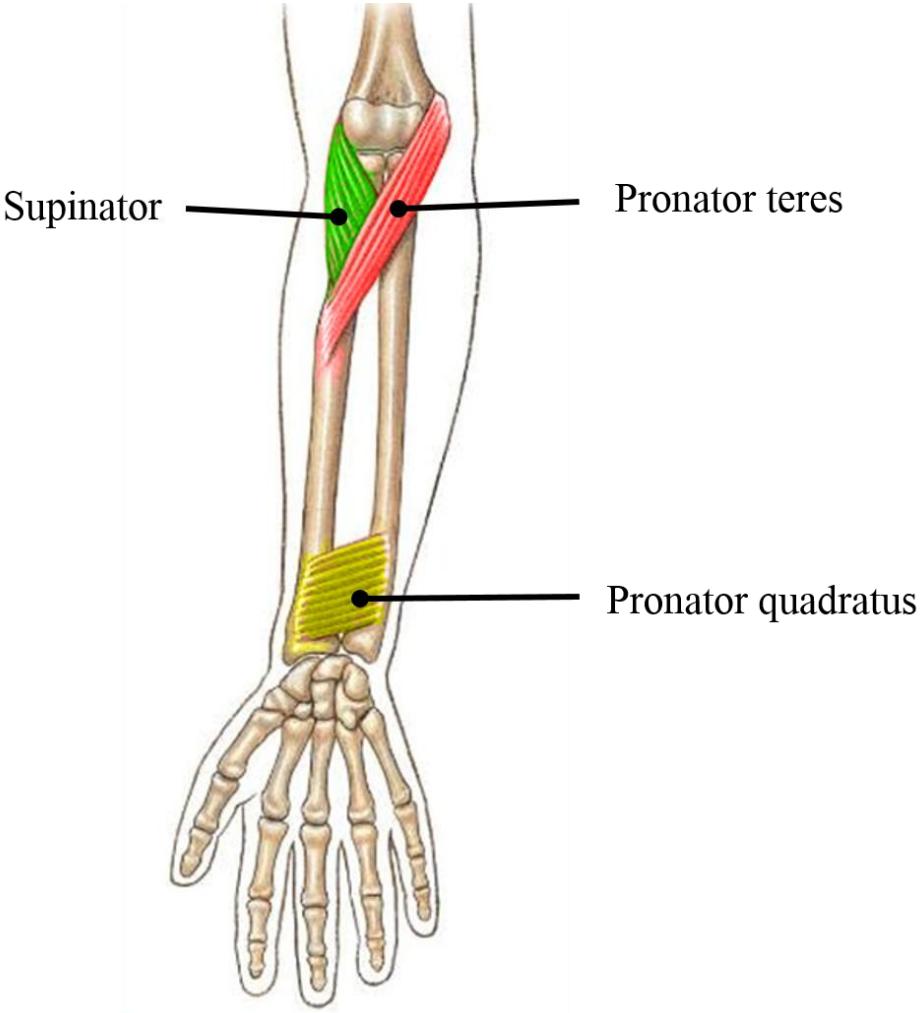

Figure 2.11. Major muscles produce arm pronation-supination

2.2 Joint kinematics

Kinematics is an important branch of biomechanical analysis that describes the motion of the bodies’ parts without considering the forces associated with it. Many studies have used joint kinematics to examine the biomechanical characteristics of the elbow joint both *in-vivo* and *in-vitro* conditions (Dunning, Zarzour, Patterson, Johnson, & King, 2001; Ferreira, King, & Johnson, 2011; King, Morrey, & An, 1993; Morrey & An, 1983; Olsen, Sojbjerg, Dalstra, & Sneppen, 1996). Elbow kinematic measurements have also been utilized for better prosthetic designs and for surgical repair and reconstruction strategies. Implant misalignment to the natural joint axis of rotation or articular surfaces can be quantified by the joint kinematics. Non-physiological joint kinematics can gradually lead to osteoarthritis development, muscle and ligament strain, and damage of the joint structure. Abnormal joint kinematics can also cause bone shielding to normal joint compression, which can further produce bone weakening by losing bone density due to resorption. Overall, much can be learned and examined by observing elbow kinematics.

The elbow is described as a trochoginglymoid joint of upper extremities (Morrey, 2000) that constructs two distinct forms of motion: flexion-extension and pronation-supination (Fig.2.12). The articulating surfaces make three articulations in the joint: the ulnohumeral, the radiohumeral, and the radioulnar. The flexion and extension motion is primarily produced by the ulnohumeral joint formed by the trochlea of the distal humerus articulating with the trochlear notch of the proximal ulna. The motion axis for flexion-extension is defined as an axis through the centers of the capitellum and the trochlear sulcus of the humerus (Amis, Dowson, Wright, & Miller, 1979; Currier, 1972). The full flexion range for normal subjects is approximately from 0° (full extension) to 145° (full flexion) (Figure 2.7a) (Morrey, 2000). Sometimes the hyperextension obtained from a subject is indicated by a negative flexion angle. The actual flexion range for an individual can be affected by many factors such as prior disease or trauma, the bulk of soft tissue presence, and the ligamentous laxity or looseness.

Forearm pronation-supination is generated by the incorporation of the radiohumeral, proximal radioulna, and distal radioulnar articulation. To produce this motion, the ulna remains stationary and the radius pronates and supinates around it. Rather than circling the whole radius about the ulna, the distal radius encircles the distal ulna and the proximal radius pivots about its own center on the capitulum surface. For a normal subject, the attainable forearm rotation range is about 150°-160° (Figure 2.7b) (Morrey, 2000), but it may vary depending on subject joint condition. Along with rotation, the radius moves proximally with pronation and distally with supination in the sagittal plane (Morrey, 2000). The proximal ulna rotates few degree externally with forearm pronation and internally with forearm supination.

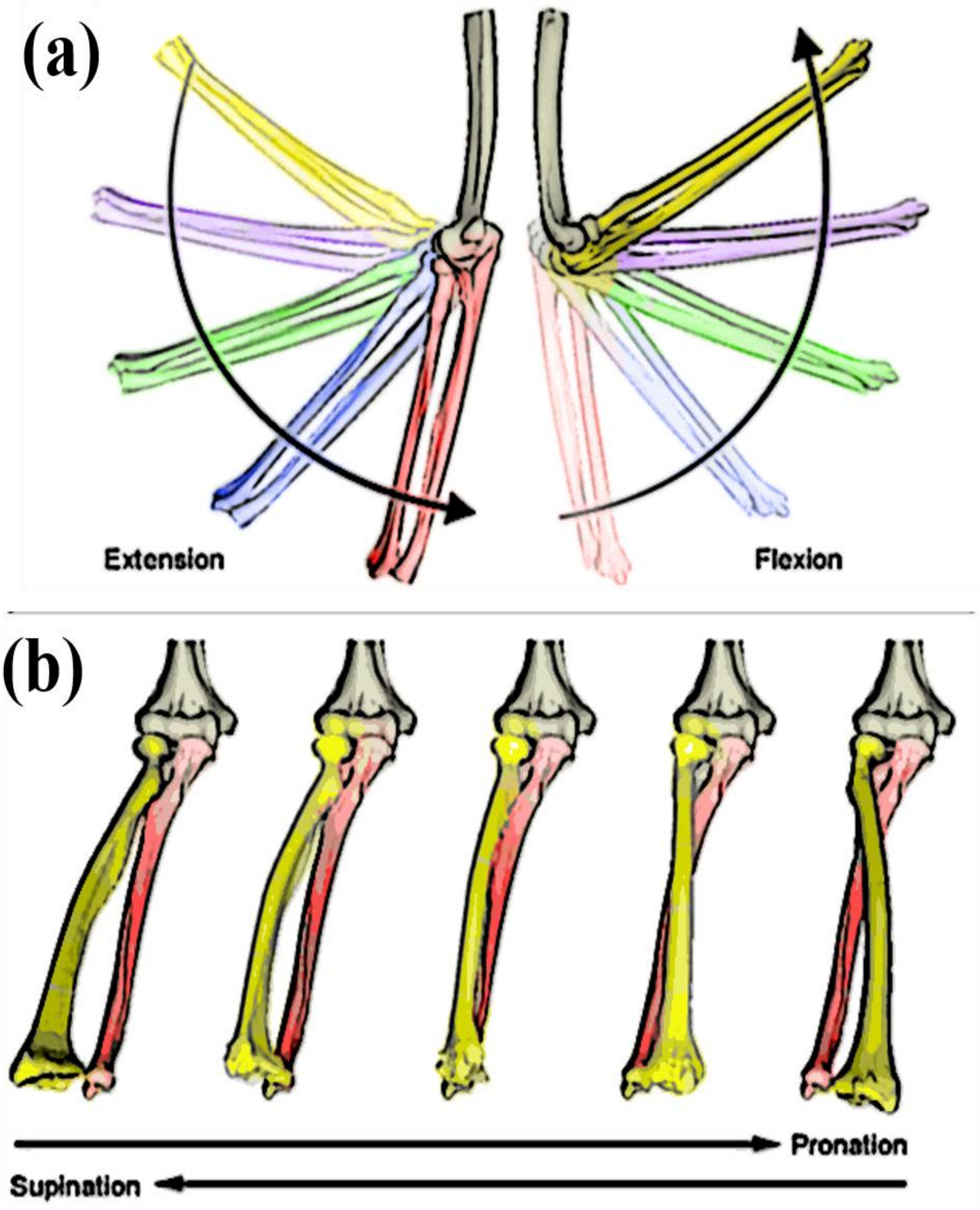

Figure 2.12. (a) The flexion-extension and (b) pronation supination view of forearm. Right arm is shown (Ferreira, 2011).

In addition to the above mentioned principal motions, the forearm bones also exhibit other motion patterns. Varus-valgus rotation of the elbow is an important kinematic measurement to elbow performance and its stability. It is the angular movement of the forearm toward-away from the body relative to the upper arm in a sagittal plane (Fig. 2.13a). The varus-valgus rotation of a normal elbow is about 5 to 10º (Podgorski, Kordasiewicz, Urban, Michalik, & Pomianowski, 2012). Internal external rotation is another useful kinematic descriptor for the elbow joint. It is the ulnar rotation about its own long axis relative to humerus, not to be confused with pronation-supination which is the radius rotation relative to ulna (Fig. 2.13b). For a healthy elbow joint the internal-external rotation is about 5 to 6º (de Haan et al., 2011).

The elbow forearm bones also exhibit some linear translation relative to the upper arm bone. The translations are defined as superior-inferior, anterior-posterior, and medial-lateral directions (Fig. 2.13c-2.13d).

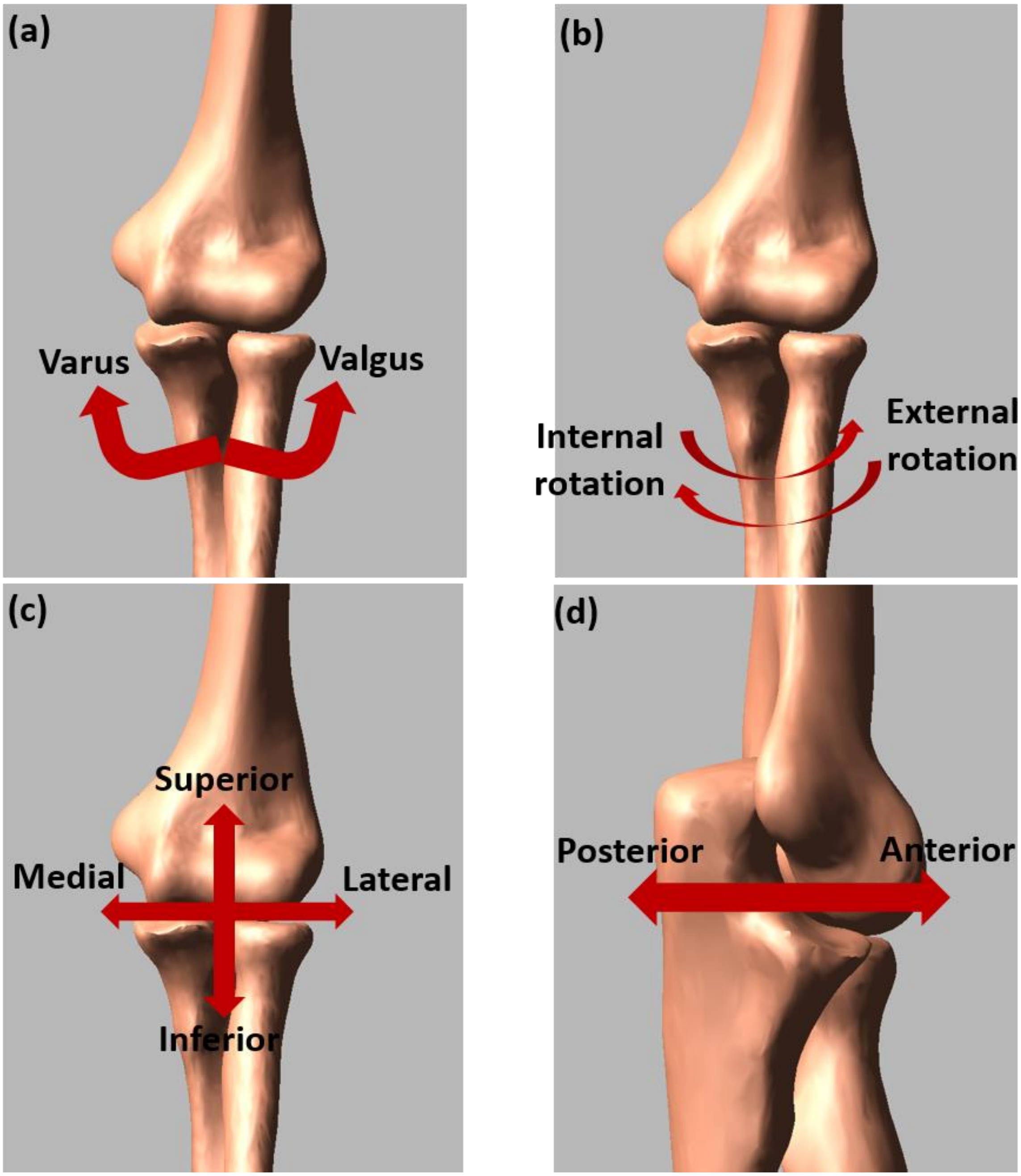

Figure 2.13. Kinematic direction and description of the elbow motion. (a) Varus-valgus rotation, (b) internal-external rotation, (c) superior-inferior and medial-lateral translation, and (d) anterior-posterior translation.

CHAPTER 3

PREDICTION OF ELBOW JOINT CONTACT MECHANICS IN THE MULTIBODY FRAMEWORK (Rahman, et al., 2016)

3.1 Introduction

The elbow joint, recognized as the most important joint of the upper extremity serves as a fulcrum of the forearm lever that greatly enhances the spatial positioning of the hand. This compound joint is formed by dual articulations of the humerus with the radius and ulna. Stabilization of the joint is achieved through the interactions of bone geometries, ligament constraints and muscular contractions (Morrey, 2000; Morrey & An, 1985; Regan, Korinek, Morrey, & An, 1991). Articular cartilage within the elbow joint withstands repetitive mechanical forces which are about 50% body weight during activities of daily living and may reach up to 3 times body weight at about 90° of elbow flexion (Eckstein, Hudelmaier, & Putz, 2006; Safran, Ahmad, & Elattrache, 2005). The elbow is the most commonly dislocated joint in children and second most commonly dislocated joint in adults often resulting in significant damage to bones and ligaments (Mehta & Bain, 2004). Forty nine percent of these dislocations are complex (dislocation associated with a fracture) which often result in long-term loss of function, chronic stiffness, instability, and posttraumatic osteoarthritis (Hildebrand, Patterson, & King, 1999; Morrey, 2000). Loss of elbow function can cause significant deficits in upper extremity mobility and jeopardize independence.

Comprehensive knowledge of the *in vivo* loading environment of the elbow structures is essential in understanding the biomechanical causes associated with elbow diseases and injuries, and in finding appropriate treatments. Currently, measuring the in *vivo* ligament, tendon and articular contact forces during elbow activities is not possible therefore, computational models have to be employed for predictions. Models can also enhance our understanding of the interrelationships between joint structures and the musculature, facilitating the development of patient specific surgical and conservative treatment strategies, and refining elbow prosthetic design.

Computational models of the elbow have been developed to study joint behavior (Garner & Pandy, 2001; Gonzalez, Hutchins, Barr, & Abraham, 1996; Holzbaur, Murray, & Delp, 2005; Lemay & Crago, 1996; Raikova, 1996), but most of these models have limited applicability because the joint structure was modeled as an idealized joint (e.g. hinge joint) rather than a true anatomical joint. Although in some circumstances such simplification is helpful for understanding joint kinematics and muscle function, it is not always appropriate to assume the human joint as a generalized mechanical joint (Benham, Wright, & Bibb, 2001). For example, three-dimensional measurements of simulated active elbow motion revealed the amount of potential varus–valgus laxity that occurs during elbow flexion to average about 3–4°, which is ignored in an idealized joint definition (Tanaka, An, & Morrey, 1998). Omission of this normal laxity into the implant design was one of the reasons behind the failure of fully constraint elbow replacement implants due to increased transfer of stresses to the implant-cement-bone interfaces resulting in aseptic loosening (O'Driscoll, An, Korinek, & Morrey, 1992). Recently, there has been an effort to develop and validate a computational model of the elbow whereby joint behavior is dictated by the three-dimensional articular contact, ligament constraints, muscle loading

(Fisk & Wayne, 2009; Spratley & Wayne, 2011). In this model, articular cartilage was not included, and bone-to-bone contact and ligament tension was used to constrain joint motion. A recent study has shown that the coronoid cartilage height at the tip of the bony coronoid was 2.96 mm, and the thickness at the tip was 2.63mm which are significant for varus stability and coronoid fracture fixation, so cartilage is too significant to exclude (Rafehi, Lalone, Johnson, King, & Athwal, 2012). Moreover, joint contact forces can be erroneously predicted since the extra conforming cartilage surface is omitted. In the previous models, the ligament tension was assumed to vary linearly with elongation and may decrease the accuracy of the model since the ligament force-length relationship is not linear.

A review of the literature also reveals few models where elbow joint cartilage contact area and contact forces have been examined. Traditional techniques such as using pressure sensitive films in a cadaver joint can give some indication of cartilage contact mechanics (Brown, Rudert, & Grosland, 2004; Stormont, An, Morrey, & Chao, 1985), but that technique has difficulty in measuring the contact of curved surfaces and also measurements may be compromised by joint fluid exposure. Several other techniques such as dynamic MRI and CT imaging (Choi et al., 2013; Kaiser, Bradford, Johnson, Wieben, & Thelen, 2013; Raghuraman et al., 2013), stereophotogrammetric (SPG) analysis (Ateshian et al., 1995; Soslowsky et al., 1992), fluoroscopy and biplane radiographic imaging (Anderst & Tashman, 2003), and tracking systems (Kura, Kitaoka, Luo, & An, 1998; Lalone et al., 2013) have been employed to measure the cartilage contact area. Recently, Willing et al. (2013, 2014) created a finite element (FE) model of the elbow to investigate articular contact mechanics (Willing, Lalone, Shannon, Johnson, & King, 2013; Willing, Lapner, Lalone, King, & Johnson, 2014). The model was validated in a static condition. Finite element models are computationally expensive and are typically used to study isolated tissues or joints in static or quasi-static conditions.

A computational musculoskeletal model with an anatomical elbow joint capable of concurrent predictions of muscle, ligament, and cartilage contact forces in dynamic conditions can be immensely useful (Guess, Liu, Bhashyam, & Thiagarajan, 2013). Such models can be effectively used to predict joint loads during activities of daily living, to study the mechanisms of joint elbow injuries such as terrible triad injuries, and to assist in designing better prosthetic implants. The multibody framework is the ideal computational platform to be used for such concurrent, dynamic simulations because of its computational efficiency. In general, contact mechanics in multibody models are greatly simplified and do not allow predictions of contact pressure and contact areas. Detailed knowledge of the contact mechanics during dynamic activities can provide insight into the mechanics of both acute and chronic injuries. The purpose of this study was to develop an anatomically correct elbow joint model with non-linear ligaments that include wrapping around bony structures, and discrete cartilage in the multibody framework, and evaluate the performance of this model in predicting bone segment kinematics against experimental measurements. After kinematic validation, a lateral ulnar collateral ligament (LUCL) deficient condition was simulated and; contact pressures and kinematics were compared to the intact elbow. This model is the first step in the development of a full musculoskeletal model of the elbow joint capable of contact pressure estimation under dynamic conditions.

3.2 Method

3.2.1 Cadaver elbow measurements

Two fresh frozen cadaver elbow specimens were used in this study (Elbow#1, 61 year old, male, right arm; Elbow#2, 42 years old, male, right arm). The elbows were thawed at room temperature for 24 h before testing. The elbow donors had never been diagnosed with major elbow diseases and the elbows appeared normal and intact during visual inspection. The elbows were imaged with both computed tomography (CT) scans and magnetic resonance imaging (MRI). The entire arm was CT scanned to obtain the complete bone lengths. Three mutually perpendicular CT sequences were taken using Siemens SOMATOM definition flash CT scanner (Siemens, Siemens Medical Solutions, PA) with the following parameters: slice thickness of 2 mm, imaging frequency 63.68 Hz, image resolution 512 × 512, and group lengths 192. MRIs were obtained using a Siemens 3T machine with a narrow field fine resolution setting. The parameters used for MRI were: TR:1200, TE:38, image resolution 320 × 320, slice thickness 0.5 mm, imaging frequency 123.17 Hz, and group lengths 178. Before imaging, a custom made ABS plastic localizer containing two perpendicular tubes and packed with mustard (visible during medical imaging) was rigidly attached with titanium screws to each bone segment (humerus, ulna and radius) to assist in global coordinate registration later in the experiment (Stylianou, Guess, & Cook, 2014). Following medical imaging, the joint capsule, ligaments, interosseous membrane, brachialis tendon, biceps tendon, triceps tendon, wrist joint and hand were kept intact, and the remaining tissues were removed by a shoulder and elbow fellowship trained orthopaedic surgeon. After dissection, the elbows were mounted in a biaxial Instron 8821 (Instron, Norwood, MA, USA) mechanical testing machine (Fig. 3.1a). The humerus head was cemented inside a cup that was attached by a hinge joint to the top ram of the mechanical tester. The intact hand was placed and secured on a slider that could slide horizontally in a single axis. Three rigid-body motion markers (each containing three infrared emitting diodes) were firmly attached to the humerus, radius, and ulna localizers. The slider plate also had a rigid motion marker added to it to measure its movement and to aid in computational model alignment. An Optotrak Certus motion capture system (Northern Digital Inc, Waterloo, Ontario, Canada) was used to track the motion of each bone segment during experimental testing.

A laxity test was then performed to calculate ligament bundle zero-load lengths (the lengths at which ligament bundles first become taut). The humerus was held in a fixed position while the ulna and radius were manually moved through their full range of motion with minimal force applied (as judged by the experimenter) (Guess, Thiagarajan, Kia, & Mishra, 2010). The kinematic envelope of motion (KEM) was measured from the corresponding bone segments using the attached Optotrak markers and camera system. The zero-load length for each ligament is determined by calculating the maximum straight-line distance between insertion and origin sites of the individual ligaments throughout the range of motion and then multiplying by a correction factor of 0.8 (Bloemker, Guess, Maletsky, & Dodd, 2012). The purpose of the correction factor is to reduce the error inadvertently introduced by the experimenter during the laxity test when a small amount of force was applied to the ligaments.

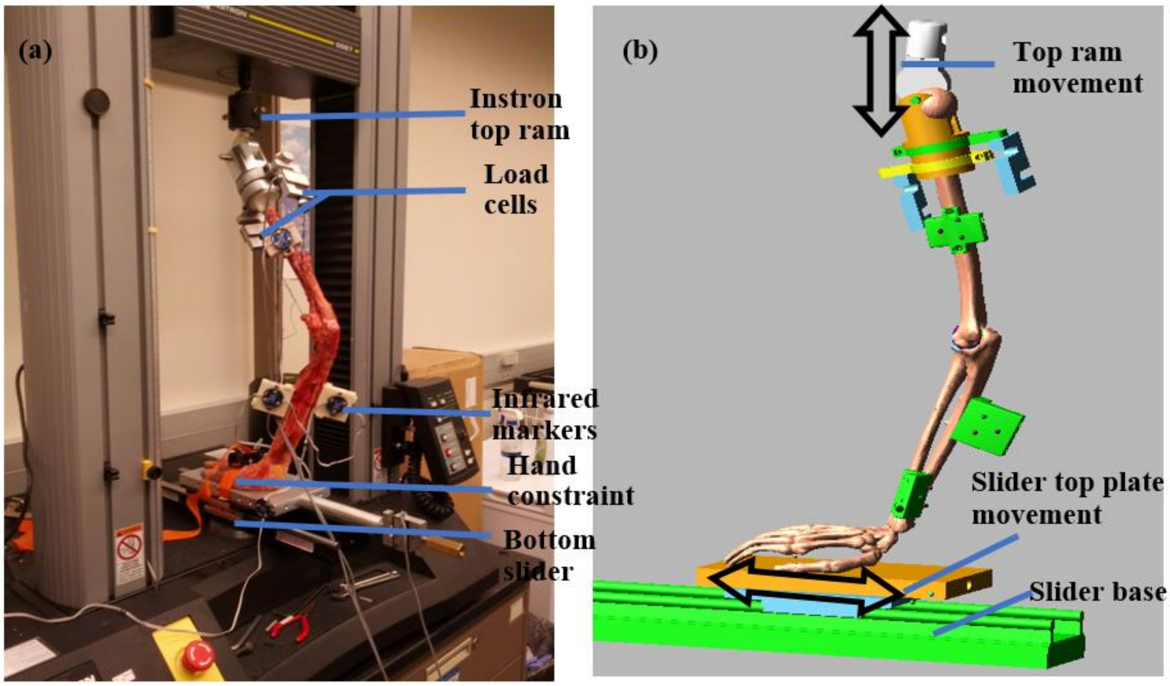

Figure 3.1. (a) Cadaver testing setup in the mechanical tester, and (b) multibody model in ADAMS

After completion of the laxity test, two 100 lb load cells were rigidly attached to the humerus cylinder to measure force in the tendons. The brachialis and triceps tendons were sutured for elbow 1 and biceps and triceps tendon were sutured for elbow 2, and attached to the load cells with a threaded nut and bolt. The sutures were pulled taut and secured to the load cell to provide passive resistance during the test. These tendon forces were measured so that they could be incorporated into the multibody model. The initial position and orientation of the cadaveric bone geometries relative to the mechanical tester were determined by recording multiple points on the localizers, along the bone surfaces, and on the load cells by using an Optotrak probe tool. The elbow joints were positioned at an approximate flexion angle of 20° before starting the test. A motion profile of 285 mm vertical displacement (285 mm downwards from starting position and then return to initial position) was applied and recorded to the top ram of the mechanical tester from the initial elbow position. This downward displacement induced elbow flexion angles from 20° to 120°. For each experimental trial, bone motion as well as tendons forces were recorded. After test completion, the joint was disarticulated and additional points were collected along the ligament insertion and origin sites with the help of an Orthopaedic surgeon using the Optotrak probe.

3.2.2 Multibody model

CT scans were segmented using 3D Slicer (www.slicer.org) to generate three-dimensional geometries of the humerus, ulna, and radius. Cartilage geometries were segmented from the MRI scans by manual segmentation available in 3D Slicer. The bone and cartilage geometries were then imported to Geomagic Studio (Geomagic, Inc., Research Triangle Park, NC, USA) for post-processing that included removing spikes, reducing noise and decimating the meshes to reduce file size. A model was created in ADAMS (MSC Software Corporation, Santa Ana, CA) by importing the geometries of the bones, cartilages, and top and bottom fixtures of the mechanical tester. The geometries were then aligned by using the initial position measurements acquired during the cadaver testing (Fig. 3.1b). The humerus was attached with a fixed joint to the top cylinder which was attached by a hinge joint to the top ram of the mechanical tester. The hand was attached with a six axis spring to the slider top plate. A translational joint was created between slider top plate and slider base. The slider base was attached by a fixed joint to the ground. A spherical joint was attached between radius and hand to represent the wrist joint.

The distal ulna and radius was attached by two force elements to represent the distal radioulnar joint. A density of 1600 kg/m^3 (Donahue, Hull, Rashid, & Jacobs, 2002) was used for bones and 1000 kg/m^3 for the articular cartilages (Zielinska & Donahue, 2006).

The ligaments and tendons were attached to the model according to the insertion and origin point cloud data collected during experimental testing. The ligaments were divided into different bundles according to their structure and function. The model included three bundles for the lateral ulnar collateral ligament (LUCL), three bundles for the radial collateral ligament (RCL) (Spratley & Wayne, 2011), three bundles for the medial collateral ligament (MCL) anterior part, three bundles for MCL posterior part, and two bundles for the annular ligament (Fisk & Wayne, 2009). The interosseous membrane was divided into five bundles; two bundles for accessory band, two bundles of central band, and one for distal band. The ligaments and the interosseous membrane were modeled as non-linear springs using a piecewise function describing the force–length relationship including the non-linear “toe” region. The toe region corresponds to the parabolic transition between the zero strain and the linear region which simulates the crimping effect of the ligament. The force-length relationship is described by equations (3-1) and (3-2) (Blankevoort, Kuiper, Huiskes, & Grootenboer, 1991; Wismans, Veldpaus, Janssen, Huson, & Struben, 1980)

$$f = \begin{cases} \frac{1}{4} k\, \varepsilon^2/\varepsilon_l & 0 \leq \varepsilon \leq 2\varepsilon_l \\ k(\varepsilon - \varepsilon_l) & \varepsilon > 2\varepsilon_l \\ 0 & \varepsilon < 0 \end{cases} \qquad \text{3-1}$$

$$\varepsilon = \left(\frac{l - l_0}{l_0}\right) \qquad \text{3-2}$$

where k is the stiffness parameter, ε_l is a spring parameter assumed to be 0.03 (Li, Gil, Kanamori, & Woo, 1999), and ε is the ligament engineering strain. Literature values for the stiffness parameter of the ligaments and interosseous membrane (Fisk & Wayne, 2009; Regan et al., 1991; Spratley & Wayne, 2011). A damping coefficient of 0.5 Ns/mm was also included in each spring element to remove the possibility of high frequency vibration during simulation (Guess, 2012).

The wrapping of the annular and lateral ulnar collateral ligament (LUCL) around the radial head, prevents definition of these ligaments with direct ligament lines of action. To simulate wrapping for these ligaments, each ligament bundle was divided into multiple elements attached in series according to their path and structure (Fig. 3.2a). For the LUCL, spheres with a diameter equal to ligament thickness were inserted into the ligament. Six degree spring elements were attached between each sphere and the radius cartilage allowing the ligament to slide over the radial head without crossing each other. For the annular ligament wrapping, small spheres were also embedded in the ligament and a line arc for each ligament bundle was placed along the perimeter of the radius head. A point-curve constraint was then defined between the spheres and line arcs, allowing the spheres to move along the path of the curves. Therefore, the radius could rotate inside the annular ligament during forearm rotation, similar to its physiological constraint.

The radial and ulnar cartilages were attached rigidly to the respective bone using fixed joints. A macro was written in ADAMS to automatically divide the humerus cartilage into discrete hexahedral elements (Fig. 3.2b). Each element had an approximate 5 x 5 mm cross-sectional area. The macro connected each cartilage element to the distal humeral articular surface with a fixed joint located at the center of each contact surface. The macro also defined a deformable contact constraint with no friction using modified Hertzian contact law (Eq. 3-3) between each humerus cartilage element with the radius and ulna cartilage geometry.

$$F_c = k_c\delta^n + B_c(\delta)\dot{\delta} \tag{3-3}$$

where F_c is the contact force, k_c is the contact stiffness, δ is the interpenetration of the geometries, n is the nonlinear power exponent, $\dot{\delta}$ is the velocity of interpenetration, and $B_c(\delta)$ is a damping coefficient. To prevent discontinuities in the solution for when the rigid bodies first come in contact, the damping coefficient is a function of interpenetration (Hunt & Crossley, 1975).

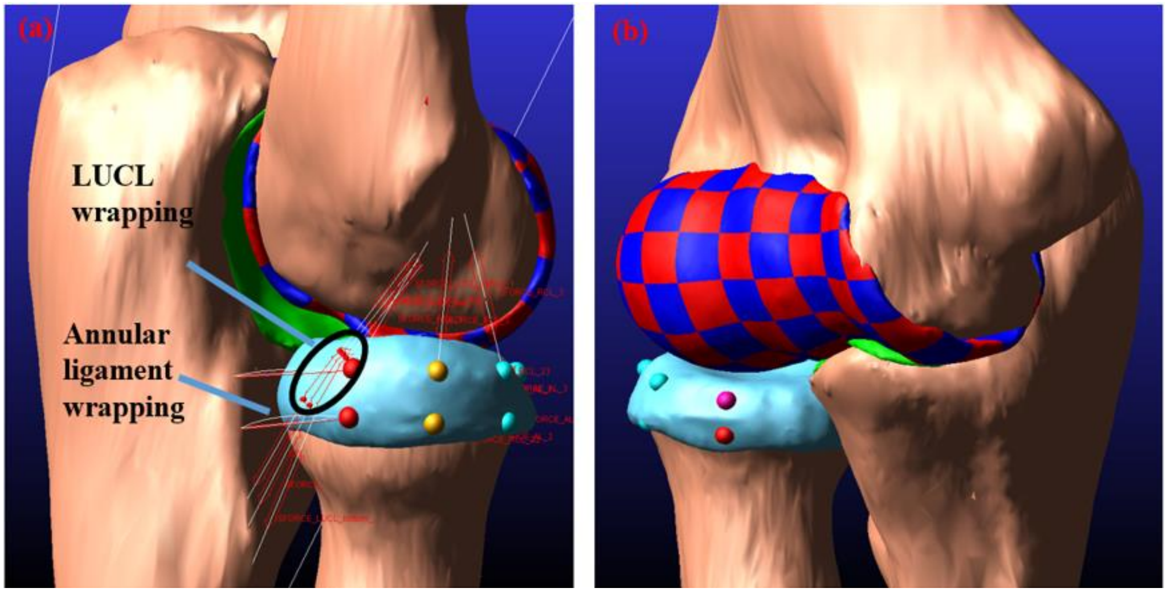

Figure 3.2. (a) Ligament wrapping around the bone, and (b) discrete humerus cartilage

Contact parameters were determined from simplified elastic foundation theory (Bei & Fregly, 2004; Blankevoort et al., 1991):

$$p = \frac{(1-\nu)E}{(1+\nu)(1-2\nu)h}\, d \qquad \text{3-4}$$

where *p* is the contact pressure, *E* is Young's modulus, *v* is Poisson's ratio, *h* is the combined cartilage thickness between the cartilages, and *d* is the spring deformation. The contact pressure *p* was computed for the values of *E* = 0.7 MPa, *v*=0.495, h= 4, 4.8, 3.07 and 3.58 (for humerus-ulna and humerus-radius of elbow 1 and 2 respectively) with *d* as an unknown spring deformation. Since the surface area of the discretized element was 25mm^2, the value of *p/d* was then multiplied by 25 to estimate stiffness of each contact. The compliant contact parameters for equation (3-4) are tabulated below (Table 3.1).

Table 3.1. Contact parameters information

Parameters	Values	
Contact type	Impact (Deformable)	
Friction	No	
Stiffness (k_c)	Elbow 1	126 N/mm (humerus-ulna), 105 N/mm (humerus-radius)
	Elbow 2	192 N/mm (humerus-ulna), 165 N/mm (humerus-radius)
Interpenetration of geometries (δ)	0.1 mm	
Exponent (n)	1.0	
Damping coefficient ($B_c(\delta)$)	2 Ns/mm	

Local coordinate systems for each bone segment were created as described by Ferreira et al. (2011) (Ferreira et al., 2011) and Morrey and Chao (Morrey & Chao, 1976) to measure segment motion. The origin for the humeral coordinate system was placed at the center of the capitellum and the X, Y and Z axes correspond to the superior-inferior (S-I), anterior–posterior (A–P), and medial–lateral (M–L) direction respectively (Fig. 3.3). The local co-ordinate system for radius and ulna were placed at the center of the radial head and greater sigmoid notch respectively. The translations of the radius and ulna were computed from the origin of their respective local coordinate system relative to the humerus local coordinate system and were presented in humerus coordinates. The rotations were represented in body 1, 2 and 3 angles (123 Euler angle sequence) which correspond to internal-external rotation (I-E), varus-valgus (VR-VL), and flexion-extension (F-E) of radius and ulna bone segment. To facilitate data comparison, all experimental data were transformed to the joint coordinate system. The 285 mm vertical downward/upwards motion profile of the top ram, and the force profiles collected from the tendon load cells were used as inputs to the model. Simulations were run for an intact elbow and the predicted kinematics of the ulna and radius were compared with the experimentally collected kinematics. A simulation using the same inputs was run for an LUCL deficient elbow.

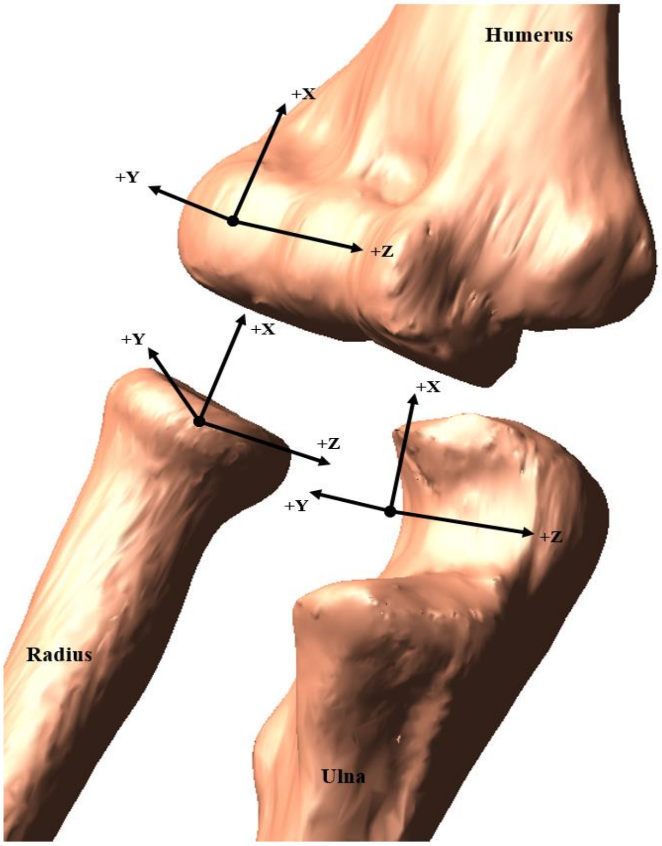

Figure 3.3. Position and orientation of the elbow joint local coordinate systems

3.3 Results

3.3.1 Model validation

Predicted and experimentally measured kinematics for the ulna and the radius are presented in Figs. 3.4 and 3.5. Overall there is good agreement between the model predicted motion patterns and the measured motions. As seen in the figures, the largest deviations from the measured kinematics occurred during low elbow flexion angles. RMS errors and correlation coefficients between the experimental and model predicted kinematics are presented in Table 3.2. The maximum ulna RMS errors were 1.5 mm in medial– lateral displacement and 4.9° in varus–valgus rotation relative to the humerus coordinate system (elbow 2). The maximum radius displacement RMS error was 2.7 mm and occurred in the medial-lateral direction for both elbows. The maximum rotation RMS error was 9.7° varus–valgus rotation of the radius for elbow 2. The largest RMS errors were observed in the radius kinematics for both elbows compared to ulna kinematics. Minimum RMS errors and the highest correlation coefficients were observed for the ulna. Correlation coefficients above 0.7 were observed for 9 out of 12 kinematic variables for both elbows.

Table 3.2. RMS error (deg, mm) and correlation coefficients for ulna and radius kinematics

Kinematics description	Elbow 1		Elbow 2	
	RMS error	Correlation coefficient	RMS error	Correlation coefficient
Ulna internal-external rotation	3.0	0.96	3.4	0.97
Ulna varus-valgus rotation	4.8	0.96	4.9	0.87
Ulna flexion-extension rotation	3.9	0.99	4.5	0.99
Radius internal-external rotation	3.1	0.93	5.3	-0.60
Radius varus-valgus rotation	5.5	0.27	9.7	-0.40
Radius flexion-extension rotation	2.9	0.99	5.9	0.99
Ulna superior-inferior displacement	0.7	0.51	0.5	0.77
Ulna anterior-posterior displacement	0.8	0.98	0.4	0.97
Ulna medial-lateral displacement	1.2	-0.22	1.5	0.83
Radius superior-inferior displacement	2.6	0.99	1.5	0.99
Radius anterior-posterior displacement	1.9	0.91	1.9	0.07
Radius medial-lateral displacement	2.7	0.86	2.7	0.93

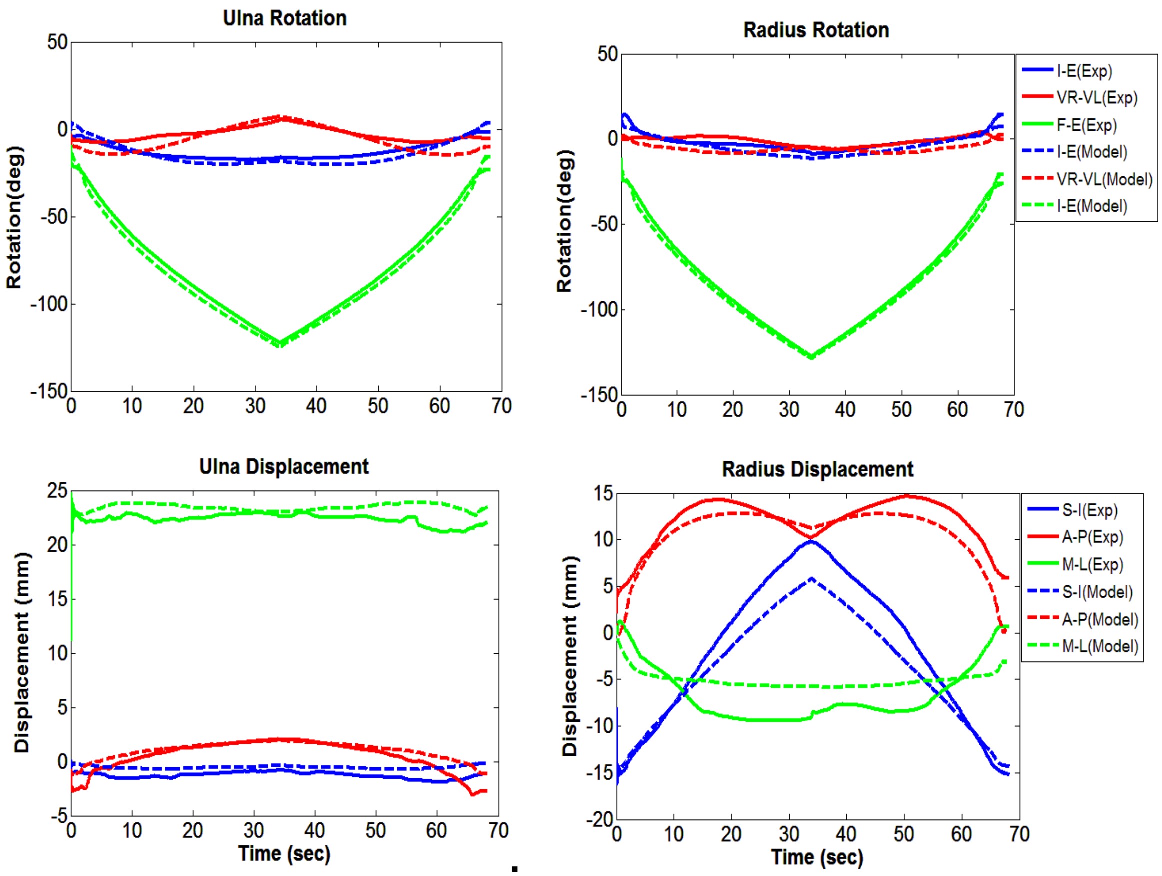

Figure 3.4. Comparison between experimental and model kinematics of the ulna and radius relative to humerus for Elbow 1

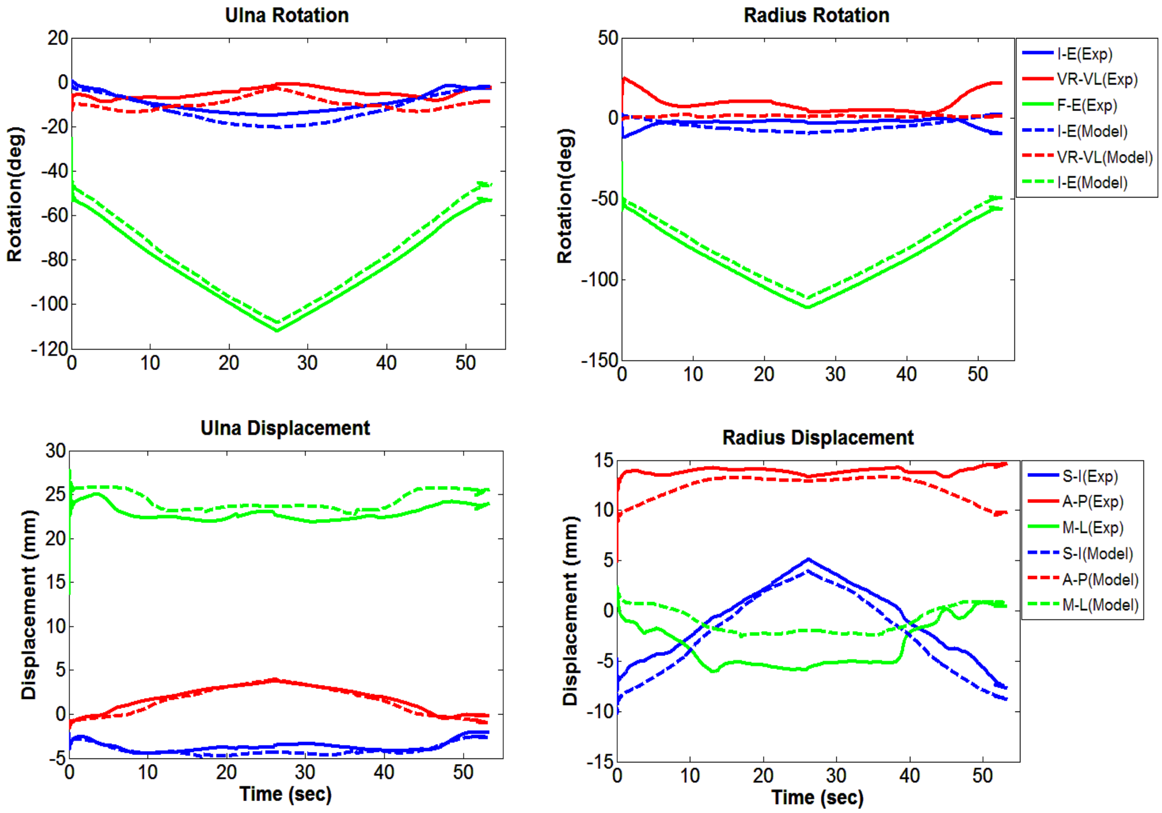

Figure 3.5. Comparison between experimental and model kinematics of the ulna and radius relative to humerus for Elbow 2

3.3.2 Ligament deficiency comparisons

A case study on the effects of LUCL deficiency on the kinematics and articular loading patterns was conducted on elbow 1. The kinematics of the intact elbow joint were used as the baseline. Fig. 3.6 demonstrates the differences in the kinematic variables between intact and LUCL deficient conditions. A noticeable kinematics difference was observed for both the ulna and radius for the LUCL deficient simulation compare to the intact elbow. The maximum ulna rotation difference was about 3.7° for varus–valgus rotation and 0.8 mm in medical–lateral displacement. The maximum difference for radius rotation was 2.7° for varus-valgus rotation and 0.9 mm for superior-inferior displacement.

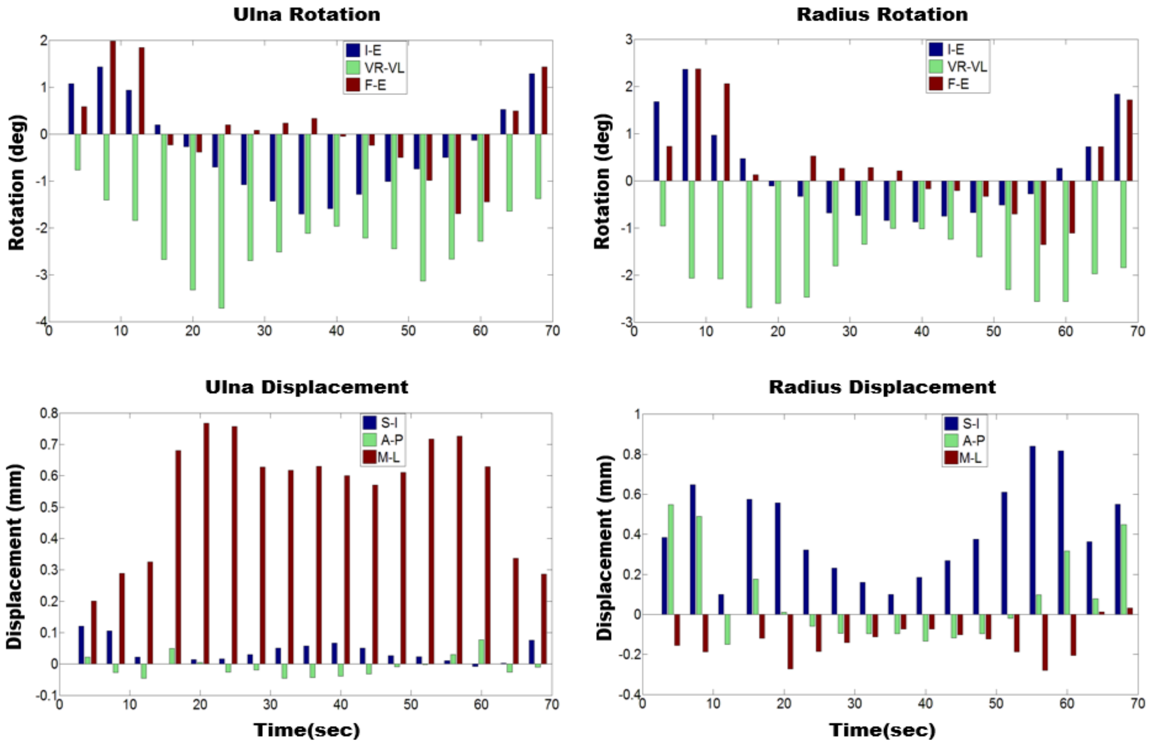

Figure 3.6. Kinematic difference between intact and LUCL deficient conditions for Elbow#1

The differences in the kinematics of the LUCL deficient elbow induced differences in the articular contact pressure distributions (Fig. 3.7). Maximum contact pressure was observed on the medial humerus cartilage (contact with ulna cartilage) for both intact and LUCL deficient conditions. However, removing the LUCL caused a small reduction in the peak contact pressure. Peak contact pressure was 7 MPa for the intact elbow and 6.48 MPa for the LUCL deficient elbow and occurred at about 90° flexion angle. Small differences of contact area were observed between intact and LUCL deficient elbow at high flexion angle.

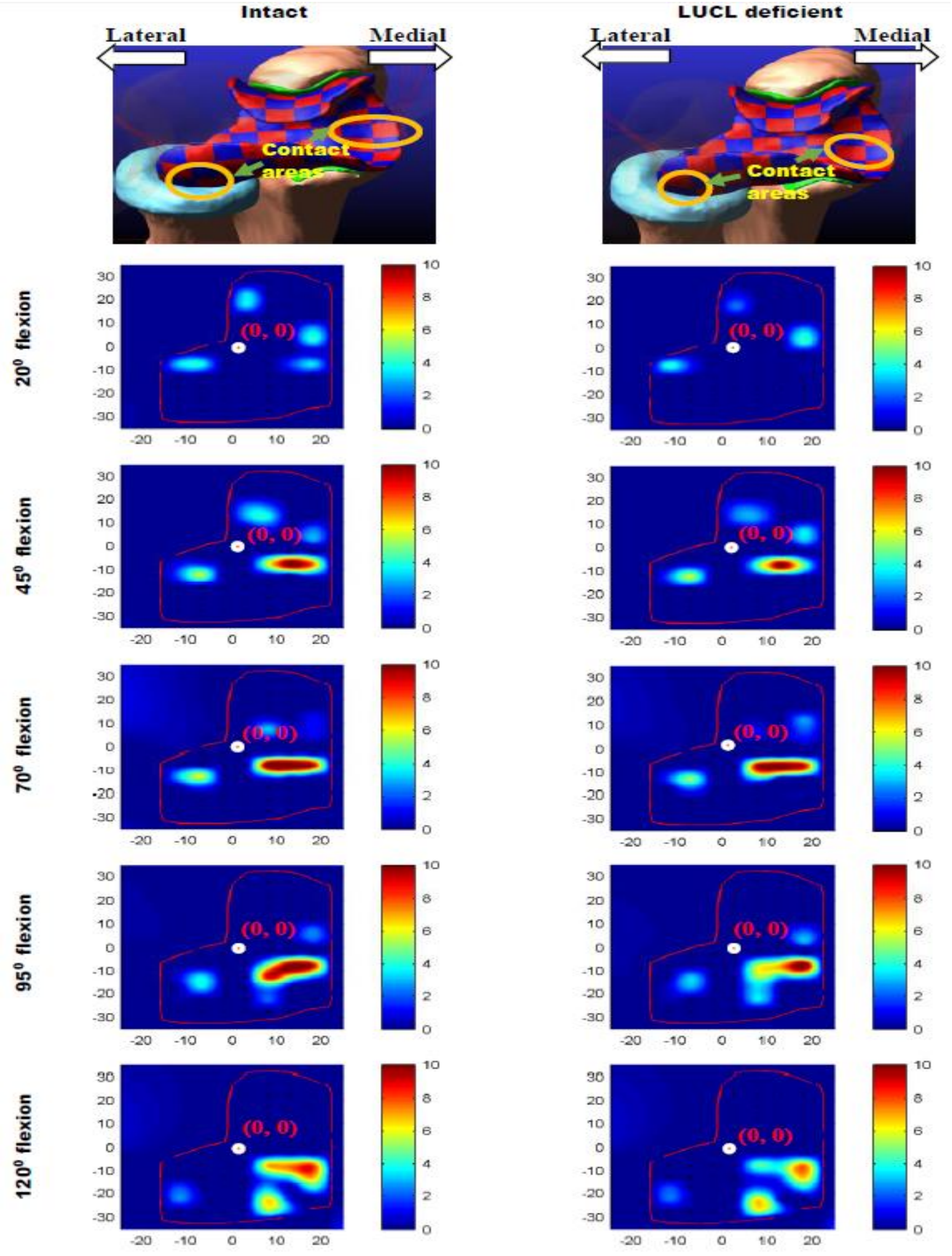

Figure 3.7. Contact pressure on humerus cartilage at different flexion angle for intact and LUCL deficient condition for Elbow#1

The centroids of the contact areas motion for intact and LUCL deficient conditions throughout the flexion–extension motion was computed and presented in Fig. 3.8. The main difference observed is in the movement of the contact between the humerus and ulna. The contact area for the LUCL deficient condition remains concentrated in the medial side of the cartilage.

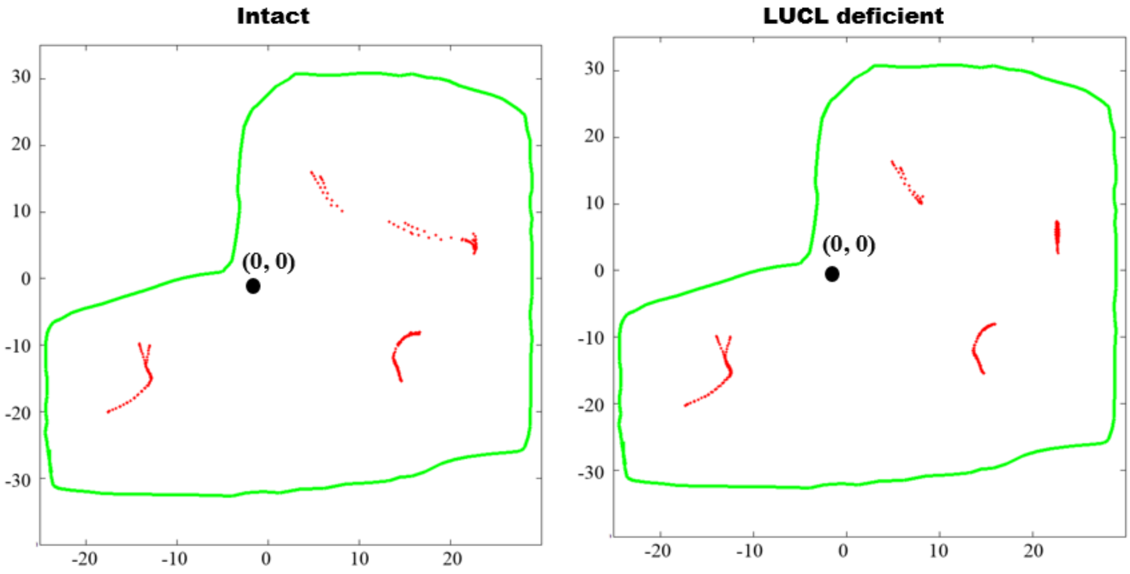

Figure 3.8. Contact area centroid motions for intact and LUCL deficient conditions.

The computational time for 68 s simulation was under 15 min for both the intact and LUCL deficient simulation (0.01 s step size, default ADAMS solver, desktop PC (Intel ® Xenon ® CPU E5-16070 @ 3.00 GHz with 32GB of RAM)).

3.4 Discussion

As a step toward developing subject specific musculoskeletal simulations that predict loading on elbow structures, this study combines a cadaver based model of the elbow joint validated kinematically and a case study on the effects of LUCL ligament deficiency. The purpose of this work was to develop an anatomically correct, subject specific elbow joint and demonstrate the efficacy of using discretized rigid bodies for the humeral cartilage in order to predict articular contact pressure and contact areas. The model predicted ulna displacements and rotations had good agreement with the experimental motions both in terms of RMS error and pattern. The largest RMS errors were observed in the radius kinematics for both elbows. Since the articulation between the radius and the humerus is not as geometrically constrained as the articulation between the ulna and the humerus, the higher errors in the radius kinematics were expected.

The kinematics of the ulna and the radius and the contact pressures on the humerus cartilage were compared for the LUCL deficient condition. The effect of removing the LUCL was noticeable in terms of kinematics of both radius and ulna. Removing the LUCL increased varus rotation significantly for both radius and ulna throughout the movement profile. Flexion–extension changes were not significant for LUCL deficiency, but significant differences on internal–external rotation occurred. The LUCL deficient elbow radius and ulna exhibited higher internal rotations than the intact elbow during deep flexion. Furthermore, the ulna displacement relative to the humerus for the LUCL deficient condition was slightly more lateral than the intact baseline condition. For the radius, a noticeable difference in superior–inferior displacement was observed. The radius in the

LUCL deficient case moved more superiorly compared to the intact case. This combined with the increased internal rotations indicate that the radius exhibits higher instability in the absence of the LUCL ligament. In our model simulations, no dislocation was observed. A small difference in contact pressure and area of contact was seen in the medial side for LUCL deficient conditions. The centroid of the contact area for the ulna stays in a more medial position compared to the intact elbow case.

The kinematic results obtained from this study are consistent with the findings of Morrey (2000), and Fisk and Wayne (2009) that demonstrate that the structures providing most of the stability in elbow flexion–extension are the contact forces between the trochlea and greater sigmoid notch and the medial collateral ligament (MCL). The stability of the radius is therefore not as strong as the ulna resulting in higher errors in the radius kinematics. The predicted contact pressure areas at 20° flexion are in good agreement with the findings of a static finite element model by Willing et al. (2013). Furthermore, our predicted ulnohumeral contact and non-contact areas were consistent with the contact patterns reported by Eckstein et al. (1995).

A limitation of this study was that the contact pressures in the cadaver elbows were not directly measured; the segment motions were captured experimentally therefore, the model was validated only on the resulting kinematics. Future studies will validate the articular contact pressure through direct measurements. The discretized cartilage parameters and discrete cartilage size is not optimized for the current model. As reported in a recent study by Willing et al. (2013), accurate selection of material properties is significant to calculate cartilage contact pressure. Future studies will optimize contact parameters and discretized cartilage size by matching a multibody cartilage model to a finite element model of same cartilage. The LUCL deficiency case study is also influenced by the boundary conditions of the cadaver experiment. In particular, the tendons were sutured and attached to load cells and the measured loads were used as input for the simulations. The tendon loads were much higher than physiological load that resulted in masking some of the effects of removing the LUCL ligament and in very high articular contact pressures.

The main aim of this study was to develop an anatomically correct subject-specific multibody model of elbow joint. The model developed for this project included subject-specific bone and cartilage geometries derived from cadaver upper limb, representation of the ligament bundles crossing the elbow, and wrapping of ligaments around bones. The humerus cartilage was represented by discrete rigid bodies fixed to the humerus bone that interacted with the radius and ulna cartilages through deformable contacts. The model was evaluated kinematically using experimental data taken from a cadaver specimen test. To our knowledge this is the only study in which discretized cartilage geometries were used to predict contact pressure at the elbow joint in a dynamic simulation. The method is computationally efficient, and capable of predicting cartilage contact area, and contact pressure during dynamic conditions while recreating the kinematics of the bony segments accurately. The model presented in this study demonstrates the efficacy of using multi-body models in studying elbow joint function and offers certain capabilities for future studies of elbow joint mechanics in dynamic conditions.

CHAPTER 4

LATERAL COLLATERAL LIGAMENT DEFICIENCY OF THE ELBOW JOINT: A MODELING APPROACH (Rahman, et al., 2016)

4.1 Introduction

The elbow joint is stabilized through the interactions of bone geometries, joint capsule, ligamentous constraints, and muscular contractions (Hildebrand et al., 1999). Deficits in one or more of these structures can have significant negative effects on normal joint performance and can cause substantial insufficiencies in upper extremity function. Computational models capable of predicting lateral collateral ligament deficiency in an anatomical elbow joint would be immensely valuable tools for various surgical procedures, such as replacement of radial head, reconstruction of a fractured radial head, or wear of total elbow arthroplasty.

The lateral collateral ligament (LCL) complex is the primary constraint resisting posterolateral rotatory instability (PLRI) and varus stresses of the elbow joint (Morrey, 2000; Nestor, O'Driscoll, & Morrey, 1992; O'Driscoll, Bell, & Morrey, 1991; O'Driscoll, Horii, Morrey, & Carmichael, 1992; O'Driscoll, Morrey, Korinek, & An, 1992). PLRI is the condition in which the radius and ulna rotate externally relative to the humerus along with posterolateral displacement of the radial head relative to the capitellum (Charalambous & Stanley, 2008; Dunning et al., 2001; O'Driscoll et al., 1991). The proximal radioulnar joint remains intact and both forearm bones rotate as a single unit (Dunning et al., 2001; O'Driscoll et al., 1991). According to some studies, PLRI consist of approximately 15° to 30° of external rotatory subluxation of the ulnohumeral joint (Lee & Rosenwasser, 1999; O'Driscoll, Morrey, et al., 1992). In a cadaver study it was observed that neither the lateral ulnar collateral (LUCL) or radial collateral ligament (RCL) can work as a sole constraint against PLRI (Dunning et al., 2001). This study suggests that when the annular ligament is intact, either the LUCL or RCL can be transected without inducing PLRI of the elbow. It is also believed that the mechanism of elbow dislocation is a continuum of damaged structures, beginning with disruption of LUCL, followed by RCL disruption, then damage to the anterior and posterior capsule (Kuhn & Ross, 2008; Morrey, 2000; O'Driscoll, Morrey, et al., 1992). Therefore, the LCL complex is considered to be the initial weak link in elbow dislocations and makes it an important focus of orthopaedic investigation.

From an anatomical point of view, the lateral collateral ligament (LCL) complex is composed of three components; the RCL, the LUCL, and the annular ligament (AL) (Morrey & An, 1985) (Fig. 4.1). The annular ligament primarily stabilizes the proximal radioulnar joint (King et al., 1993; Morrey & An, 1985). For most lateral elbow dislocations, the proximal radioulnar joint remains stable and the annular ligament remains intact (Dunning et al., 2001; Morrey, 2000; O'Driscoll et al., 1991; Rafee, Rajasekhar, & Shah, 2006). Therefore, the annular ligament deficient condition was not investigated in this study.

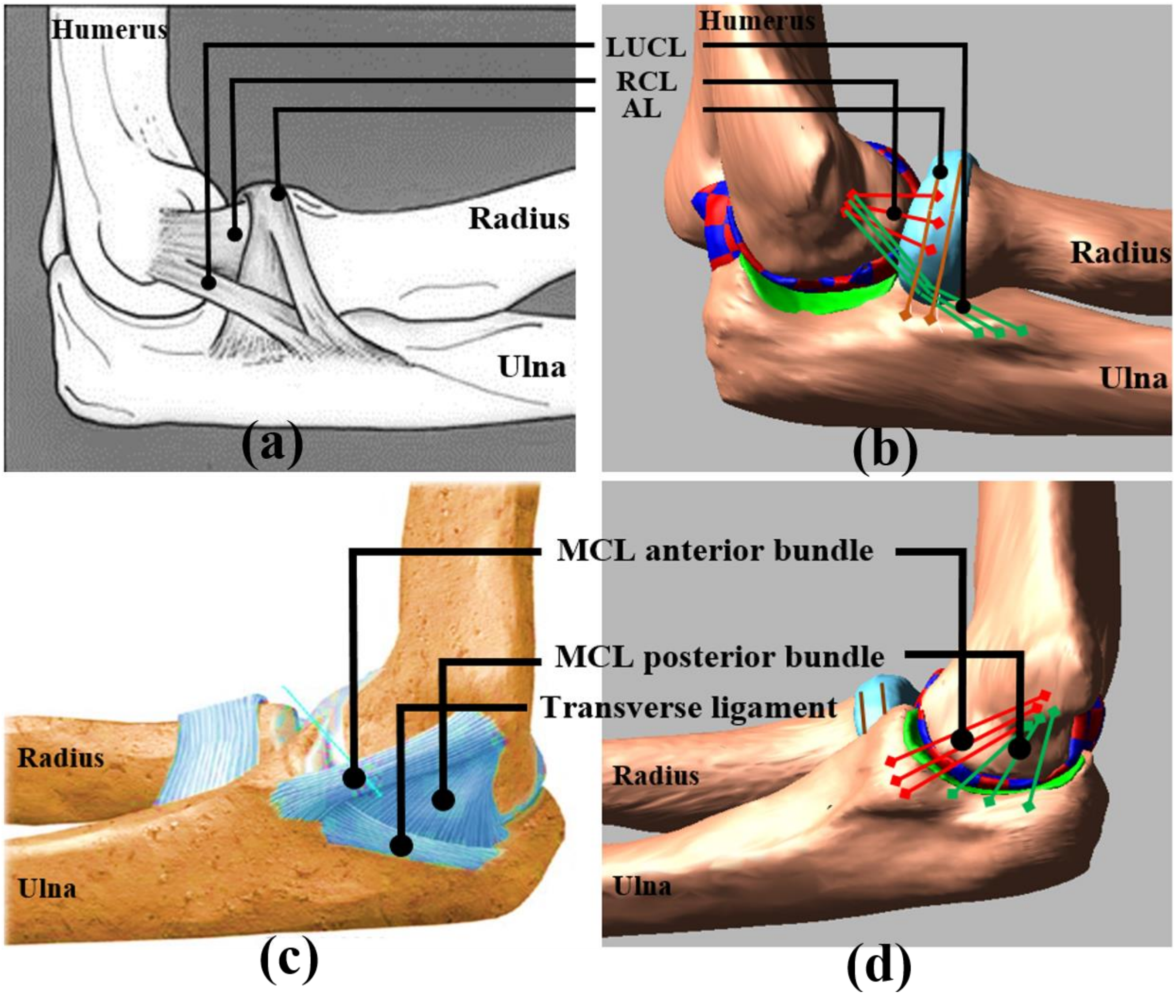

Figure 4.1. The lateral collateral ligament and the medial collateral complex (a),(c), and the corresponding ligament representation in the model (b),(d).

The purpose of this study was to investigate the effects of lateral collateral ligament deficiency on elbow kinematics, ligament loads, and articular contact pressure using an anatomically correct computational multibody elbow joint model. Four different conditions were simulated for this study (i) simulation with all ligaments intact (baseline) (ii) simulation for RCL deficiency (iii) simulation for LUCL deficiency (iv) and simulation for combined RCL & LUCL deficiency (called as ‘Both deficient’ throughout the manuscript).

4.2 Materials and methods

A previously developed anatomically correct computational multibody model created from a cadaver sample (61 yrs, male, right arm) was used as the basis of the model in this study (Rahman, Cil, Johnson, Lu, & Guess, 2014). Discretized cartilage representation was added to allow for calculation of contact characteristics. Three-dimensional bone and cartilage geometries were generated from the CT and MRI images using 3D Slicer (www.slicer.org). Post processing of the geometries such as, removing the spikes and noise, and decimating the geometries to reduce the file size, were done in Geomagic Studio (Geomagic, Inc., Research Triangle Park, NC, USA). The multibody model was created in a commercially available dynamic analysis program ADAMS (MSC Software Corporation, Santa Ana, CA) (Fig. 4.2a). The geometries were imported in ADAMS and aligned at an initial flexion angle of about 20°. The humerus was attached with a translational joint to the ground. A spherical joint was placed between the radius and the hand to represent the wrist joint. Densities of 1600 kg/m^3 (Donahue et al., 2002) and 1000 kg/m^3 (Zielinska & Donahue, 2006) were applied to the bone and cartilage respectively.

The ligament and interosseous membrane attachment sites and orientations were identified and digitized using an Optotrak probe (NDI, Waterloo, Ontario, Canada) during dissection by a shoulder and elbow fellowship trained orthopaedic surgeon, anatomical atlases (Netter & Hansen, 2003), and published studies (Fisk & Wayne, 2009; Morrey, 2000; Morrey & An, 1985; Skahen et al., 1997; Spratley & Wayne, 2011). The model included three bundles for the LUCL, three for RCL, three for the MCL anterior band, three for the MCL posterior band, and two for the annular ligament. The transverse ligament was not included since it has little or no contribution to elbow stability (Morrey, 2000). The interosseous membrane was divided into five bundles; two for the accessory band, two for the central band, and one for the distal oblique band (Fisk & Wayne, 2009; Spratley & Wayne, 2011). The ligaments and interosseous membrane were modeled as non-linear force elements using a piecewise function that describes the force-length relationship including the non-linear "toe" region. The toe region corresponds to the parabolic transition between zero strain and the linear region, which simulates the crimping effect of the ligament fibers (Blankevoort et al., 1991; Wismans et al., 1980). The force-length relationship was described by equations (4-1) and (4-2) as follows:

$$f = \begin{cases} \frac{1}{4} k\, \varepsilon^2 / \varepsilon_l & 0 \le \varepsilon \le 2\varepsilon_l \\ k(\varepsilon - \varepsilon_l) & \varepsilon > 2\varepsilon_l \\ 0 & \varepsilon < 0 \end{cases} \qquad 4\text{-}1$$

$$\varepsilon = \left(\frac{l - l_0}{l_0}\right) \qquad 4\text{-}2$$

where *k* is the stiffness parameter and ε is the ligament engineering strain. The spring parameter ε_l is a constant value and assumed to be 0.03 (Li et al., 1999).

The stiffness parameter *k* was obtained from the literature (Fisk & Wayne, 2009; Regan et al., 1991) (Table 1). The zero-load length, l_0, which is the ligament length where the ligament first becomes taut, was based on a laxity test performed in a previous cadaveric study (Rahman et al., 2014). Briefly, to determine l_0, the humerus was held in a fixed position while the lower arm was manually moved through its full range of motion with minimal force applied (as judged by the experimenter). The resulting bone kinematics were measured with Optotrak rigid body motion markers. The l_0, for each ligament bundle was estimated by computing the maximum straight line distance between origin and insertion sites of the ligament throughout the range of motion and then multiplying by a correction factor of 0.8 (Bloemker et al., 2012; Guess et al., 2013; Rahman et al., 2014). The correction factor was applied to reduce the error inadvertently introduced by the experimenter during the laxity test by applying a small load on the ligaments (Guess et al., 2013). Each ligament force also included a parallel damper with a damping coefficient of 0.5 Ns/mm to remove the possibility of high frequency vibrations during simulation (Guess et al., 2010). A custom subroutine was written in ADAMS to implement equations (4-1) and (4-2).

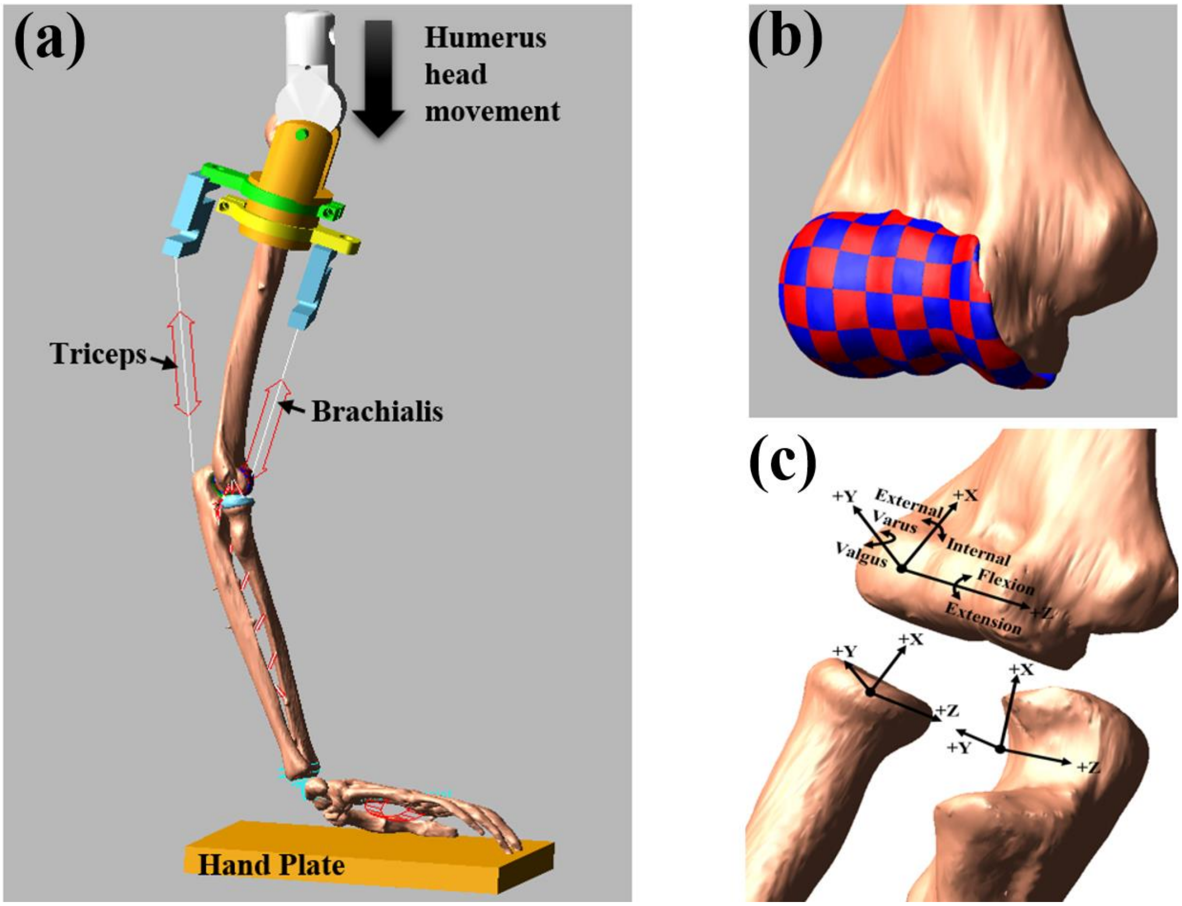

Figure 4.2. (a) Elbow model in ADAMS, (b) discretized humerus cartilage, and (c) joint coordinate system

Inputs to the subroutine were the ligament stiffness and strain, damping coefficient, ligament length at the constructed position, and the ligament zero-load length. Ligament wrapping was employed to better represent the ligament force's lines of action by dividing the ligament into multiple elements attached in series through via points (Rahman et al., 2014). For example, to simulate wrapping around the radius for the annular ligament, two line arcs were placed along the perimeter of the radius head together with the non-linear force elements. This allowed the radius to rotate inside the ligament but did not allow motion in the medial-lateral direction. For the LUCL, ellipsoids with a diameter equal to the ligament thickness were embedded in the ligament (via points) and a contact constraint was applied between the ellipsoid and the radius cartilage so that this via point would stay on the surface of the radius cartilage. The force elements representing the LUCL were then defined between origin, via point and insertion (Fig 4.1b).

Table 4.1. Ligament stiffness properties.

Tissue Complex	Bundle name	Stiffness (N/mm)
Medial collateral ligament (MCL) complex	MCL anterior bundles	24.1
	MCL posterior bundles	17.4
Lateral collateral ligament (LCL) complex	LUCL bundles	19.0
	RCL bundles	15.5
	Annular ligament	57.0
Interosseous membrane	Accessory band	18.9
	Central band	65.0
	Distal oblique band	65.0

Constant muscle tension of 40N for the triceps and 20N for the brachialis were applied in the model (Morrey, Tanaka, & An, 1991). The humerus cartilage was discretized into multiple elements to calculate contact pressure distribution instead of single point contact (Fig. 4.2b). A custom macro was written in ADAMS to automatically divide the humerus cartilage into discrete hexahedral elements of approximate cross-sectional area of 5 x 5 mm (Guess, 2012; Guess et al., 2013; Guess & Stylianou, 2012; Lu, Pulasani, Derakhshani, & Guess, 2013; Stylianou, Guess, & Kia, 2013). The custom macro also connected each cartilage element to the distal humerus surface with a fixed joint. The ulna and radius cartilage were attached with a fixed joint to their respective proximal articulating surfaces. Deformable contact constraints with viscous damping were applied using modified Hertzian contact law (Eq. 4-3) between each humerus cartilage element with the radius and the ulna cartilage geometries (Machado, Moreira, Flores, & Lankarani, 2012).

$$F_c = k_c\delta^n + B_c(\delta)\dot{\delta} \tag{4-3}$$

where F_c is the contact forces, k_c is the contact stiffness, δ is the interpenetration of the geometries (maximum penetration depth between two geometries), n is the nonlinear power exponent, $\dot{\delta}$ is the velocity of interpenetration, and $B_c(\delta)$ is a damping coefficient. The damping coefficient $B_c(\delta)$ is defined as (Machado et al., 2012; Stylianou et al., 2013):

$$B_c(\delta) = \begin{cases} 0 & \delta \leq 0 \\ B_{max}\left(\dfrac{\delta}{d_{max} - \delta}\right)^2\left(3 - \dfrac{2\delta}{d_{max} - \delta}\right) & 0 < \delta < d_{max} \\ B_{max} & \delta \geq d_{max} \end{cases} \tag{4-4}$$

where d_{max} is the penetration at which the maximum damping B_{max} is applied.

Elastic foundation theory was used to estimate the contact parameters (Bei & Fregly, 2004; Blankevoort et al., 1991).

$$p = \frac{(1-\nu)E}{(1+\nu)(1-2\nu)h}\, d \tag{4-5}$$

where p is the contact pressure, E is Young's modulus, ν is Poisson's ratio, h is the combined cartilage thickness in articulation, and d is the spring deformation. The contact pressure p was computed for the values of E = 0.7 MPa (Athanasiou, Rosenwasser, Buckwalter, Malinin, & Mow, 1991), v=0.495, h= 4 (humerus-ulna articulation), 4.8 (humerus-radius articulation) with d as an unknown spring deformation. Since the surface area of the discretized element was 25mm^2, the value of p/d was then multiplied by 25 to estimate stiffness of each contact. A value of 126 N/mm for k_c was obtained for the ulnohumeral contact and 105 N/mm for the radiohumeral contact. Values for d_{max} = 0.1, exponent n=1, and B_{max}= 2 Ns/mm were used in equations (4-3) and (4-4).

Local coordinate systems for each bone segment (Fig. 4.2c) were placed as described in the literature to measure bone motion (Ferreira et al., 2011; Morrey & Chao, 1976).The translations and rotations of the radius and ulna were computed from the origin of their respective local coordinate system relative to the humerus local coordinate system. The translations were represented in superior– inferior (S-I), anterior–posterior (A–P), and medial–lateral (M–L) directions. The rotations were represented in internal–external rotation (I-E), varus–valgus (VR-VL), and flexion–extension (F-E). The elbow was placed initially at approximate 20° flexion angle and a 345 mm vertical downward motion profile was applied over 40 seconds to the humerus head. The vertical displacement induced flexion from the initial position to a maximum flexion angle of 135°. To simulate the ligament deficient conditions, the respective ligament bundles were removed from the model. All ligament deficient conditions and the intact elbow were subjected to the same motion profile.

4.3 Results

No dislocations were observed for either the LUCL or the RCL deficient cases, but a complete elbow dislocation was observed at 110º of flexion when both of them were sectioned together.

4.3.1 Kinematic comparison

Kinematic variations for different ligament conditions are presented in increments of 10° of flexion (Fig. 4.3). The maximum ulna external rotations were 19° (at 110° flexion) for the intact and RCL deficient condition, 18° (at 100° flexion) for the LUCL deficient condition, and 21° (at 70° flexion) for the both deficient condition. The maximum observed ulna varus rotations were 8° (at 130° flexion) for the intact condition, 8° (at 130° flexion) for the RCL deficient condition, 11° (at 130° flexion) for the LUCL deficient condition, and 35° (at 100° flexion) for the both deficient condition. Maximum ulna inferior displacements were 0.4mm, 0.5mm, and 0.9mm for the intact, RCL, and LUCL deficient conditions respectively, and reached 18mm at 110° flexion for the both deficient condition. Maximum inferior displacements of the radius were 13.5mm for the intact condition and 25.3mm for the both deficient condition. Along with inferior displacement, the ulna translated 18.7mm in the posterior direction in the both deficient condition. Medial-lateral translations were not markedly different in any of the ligament deficient conditions.

Table 4.2. Root mean square (absolute and percent to intact) kinematic differences between intact (baseline) and ligament deficient conditions.

	Ulna kinematics					**Radius kinematics**				
	I-E (deg) (%)	VR-VL (deg) (%)	S-I (mm) (%)	A-P (mm) (%)	M-L (mm) (%)	I-E (deg) (%)	VR-VL (deg) (%)	S-I (mm) (%)	A-P (mm) (%)	M-L (mm) (%)
RCL deficient	0.1	0.3	0.1	0.0	0.1	0.4	0.8	0.3	0.1	0.1
	0.4	1.2	7.4	0.0	2.9	1.5	9.2	1.2	0.8	1.7
LUCL deficient	1.9	3.8	0.4	0.2	0.5	3.5	7.6	2.5	1.4	0.3
	8.4	16.1	22.2	7.2	14.7	17.2	87.9	10.4	12.0	5.0
Both deficient	8.9	26.5	8.3	3.6	0.9	3.5	8.4	18.4	7.5	6.8
	39.2	112.7	614.3	130.0	26.5	13.2	97.2	76.5	64.4	114.1

Overall RCL deficiency induced very small changes in the kinematics throughout the flexion profile (Table 4.2). LUCL deficiency induced larger changes in the kinematics than the RCL deficiency with the most significant changes in the internal–external and varus-valgus axes of rotation. The biggest and most significant changes occurred in the both LUCL and RCL deficient condition as a consequence of the elbow dislocation that occurred at 110° flexion (Fig 4.4).

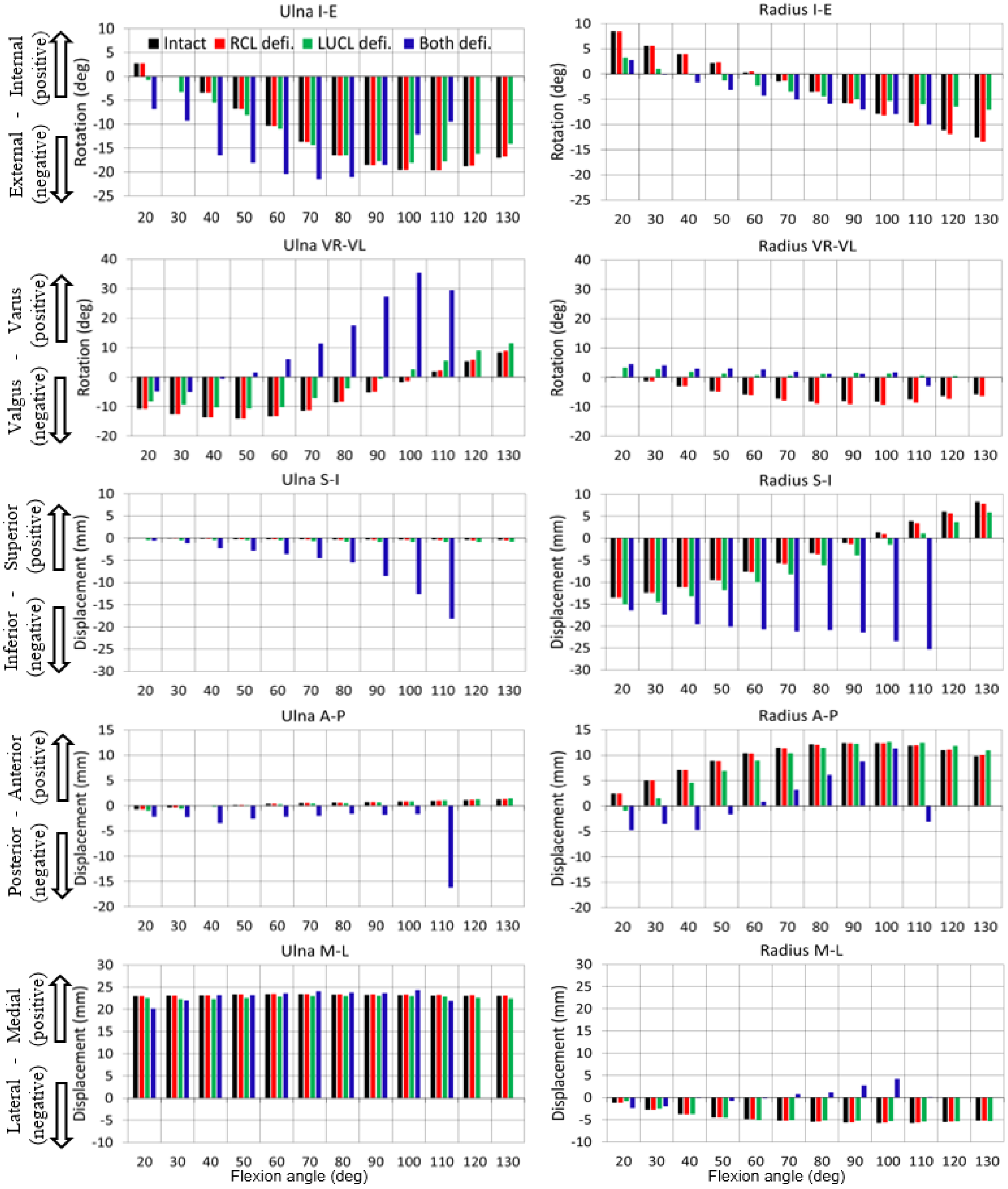

Figure 4.3. Ulna and radius kinematics relative to the humerus for baseline and ligament deficient conditions in 10° flexion angle intervals.

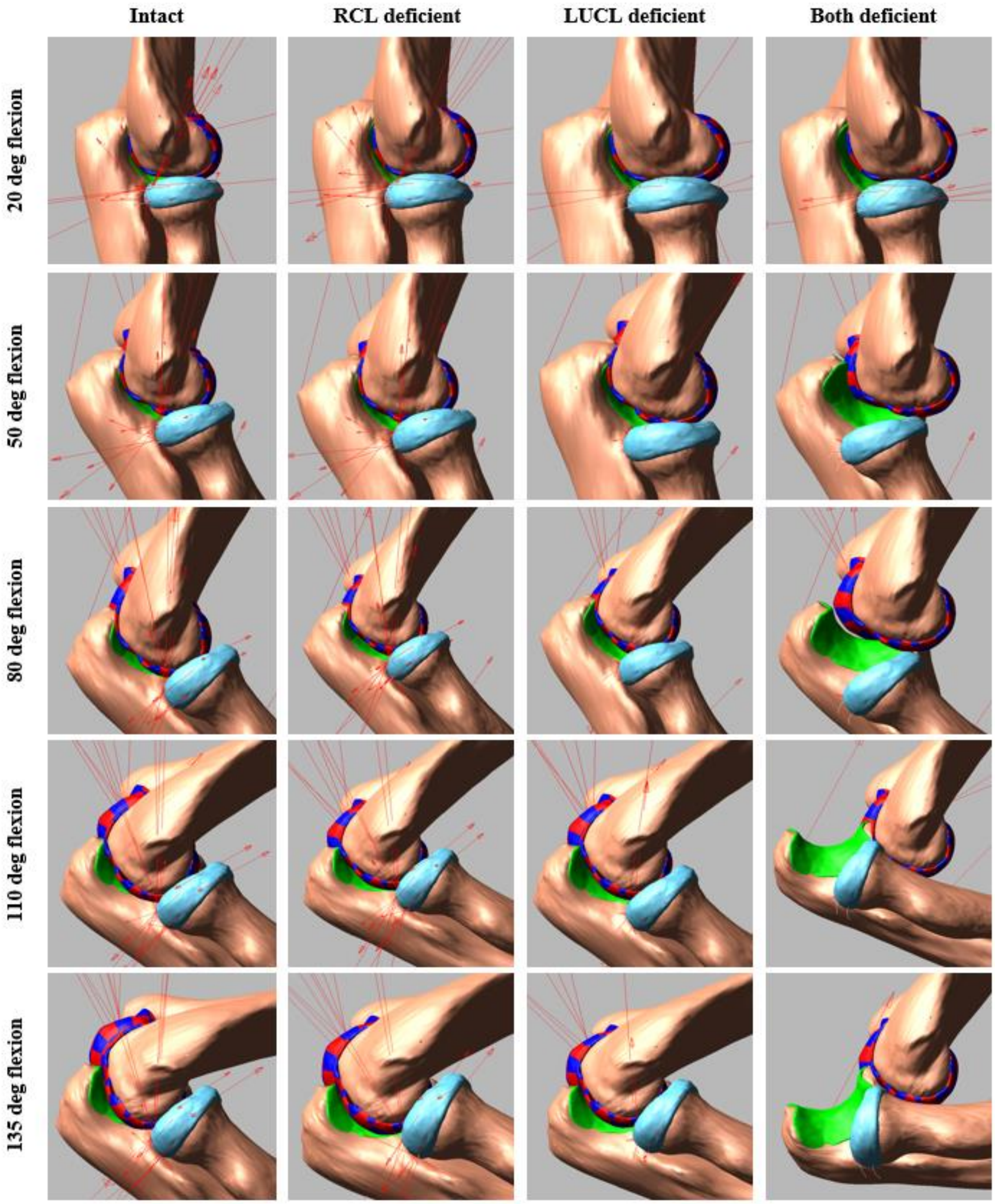

Figure 4.4. Elbow joint configuration at different flexion angles. Red arrows represent the ligament and contact force vectors.

4.3.2 Contact area and pressure comparison

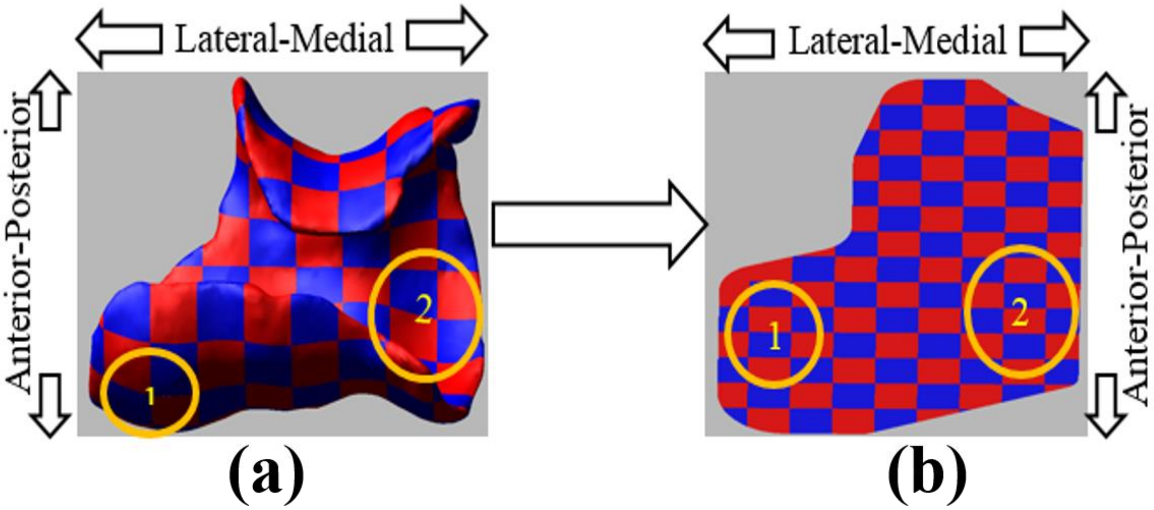

Figure 4.5. (a) Discretized three dimensional humerus cartilage, and (b) approximate flat surface representation. The circles signify the location of the major contact areas. Region 1 is the location of the humerus-radius interface and region 2 is the location of the humerus-ulna interface.

A flat surface approximation of the curved humerus cartilage was used to present the contact pressure and contact areas results (Fig. 4.5). Maximum contact pressures always occurred on the medial humerus cartilage (contact with ulna cartilage) in all ligament conditions. Peak contact pressure was 5.2 MPa for the intact and RCL deficient elbow and occurred at about 90° flexion angle. Peak contact pressure for LUCL deficient elbow was 5.4 MPa and occurred at about 130° flexion angle. Peak contact pressure for both deficient elbow was 6 MPa and occurred at about 90° flexion angle. Consistent with the contact pressure, contact areas for the intact and the RCL deficient elbow were almost identical (Fig. 4.6). Small changes in the contact area were observed for the LUCL deficient elbow at large flexion angles. Contact area changes for the both deficient case were the most pronounced with loss of almost all contacts at large flexion angles. Because of the “perched” elbow configuration at deep flexion angles the olecranon tip touches the humerus cartilage thus creating a small contact area. Contact area centroid motion path of the two major contact areas showed a similar trend. There was no difference of the contact area centroid motion between the intact and the RCL deficient elbow. For the LUCL deficient elbow the contact area centroid for the both ulna and radius contact moved more medially. The most significant change in the contact area time history occurred in the both deficient case with the centroid motion outlining the complete elbow dislocation. Centroid motion further demonstrates that with increasing the flexion angles, contact areas moved to the anterior direction in all simulated cases.

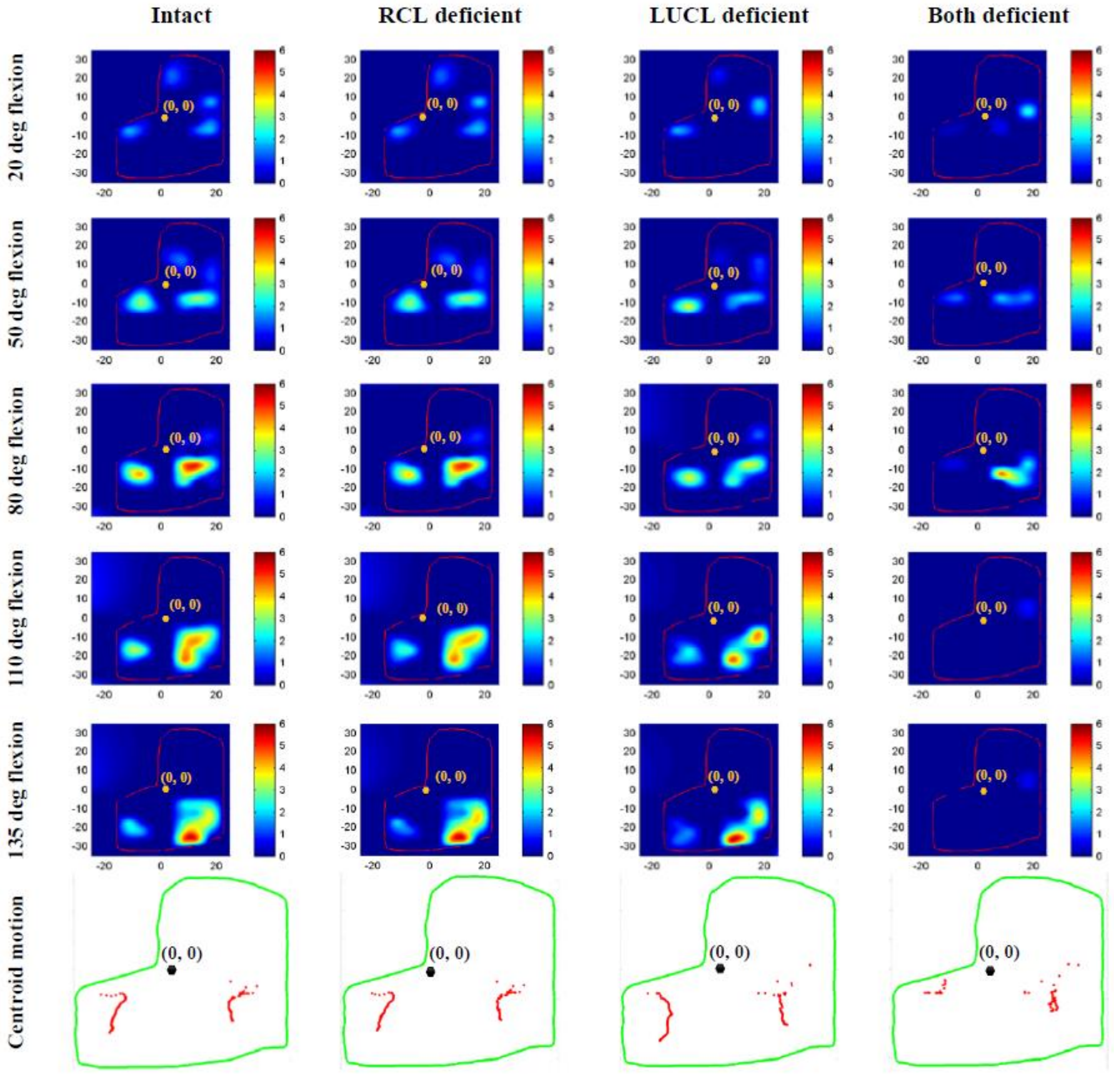

Figure 4.6. Contact pressure distribution on the humerus cartilage at different flexion angles. The centroid path of the two major contact areas during flexion is shown in the bottom panel.

4.3.3 Ligament load observation

For the LUCL deficient elbow, a noticeable increase of the RCL peak load was observed (Table 4.3). However the RCL deficient condition did not increase the LUCL peak load considerably. Peak loads in the intact ligaments were significantly lower in the both LUCL and RCL deficient condition.

Table 4.3. Maximum ligament loads and corresponding flexion angles

Ligament bundle name	Intact		RCL deficient		LUCL deficient		Both deficient	
	Peak load (N)	Flexion angle (deg.)	Peak load (N)	Flexion angle (deg.)	Peak load (N)	Flexion angle (deg.)	Peak load (N)	Flexio n angle (deg.)
MCL anterior band, anterior bundle	204	112	200	110	196	115	135	85
MCL anterior band, central bundle	211	135	210	135	206	135	121	85
MCL anterior band posterior bundle	219	135	218	135	196	115	93	85
MCL post. band, anterior bundle	112	135	111	135	106	135	49	105
MCL posterior band, central bundle	120	135	119	135	113	135	90	108
MCL post. band, posterior bundle	132	135	123	135	114	135	118	110
LUCL, anterior bundle	34	20	34	20	-	-	-	-
LUCL, central bundle	87	95	91	100	-	-	-	-
LUCL, posterior bundle	86	135	93	135	-	-	-	-
RCL, anterior bundle	3	68	-	-	2	25	-	-
RCL central bundle	2	30	-	-	31	100	-	-
RCL, posterior bundle	62	135	-	-	92	135	-	-
Annular ligament, proximal bundle	63	120	24	108	74	125	24	20
Annular ligament, distal bundle	22	120	22	114	10	125	12	30

4.4 Discussion

Many studies have recognized the need to examine lateral collateral ligament injury in the human elbow joint (Charalambous & Stanley, 2008; Z. A. Cohen, Henry, McCarthy, Mow, & Ateshian, 2003; Dunning et al., 2001; Hannouche & Begue, 1999; Nestor et al., 1992; O'Driscoll et al., 1991; O'Driscoll, Horii, et al., 1992; Olsen et al., 1998; Olsen, Vaesel, Sojbjerg, Helmig, & Sneppen, 1996). In this study, a computational multibody model of the elbow was used to investigate elbow joint behavior during flexion in the presence of lateral collateral ligament deficiency. Multibody computational models can predict important parameters that are difficult or not possible to capture experimentally such as ligament forces and cartilage contact pressures. A previously developed anatomically correct computational multibody model was used for this study (Rahman et al., 2014). The model includes discretized humerus cartilage that allows computation of contact pressure distribution and contact area.

Variations of relative bone kinematics were observed for the different ligament deficient conditions simulated with this model (Fig. 4.3). Intact elbow and the RCL deficient condition internal-external rotations were almost identical. A small variation in internal-external rotation between the intact elbow and the LUCL deficient condition was observed, and substantial differences occurred for both RCL and LUCL deficient condition. The both ligament deficient condition induced higher external rotation of the ulna at low flexion angles and lower external rotations at deep flexion compared to the intact case. Varus-valgus rotations were also significantly different for the both deficient condition compared to the other three conditions. Bone displacements for the both deficient condition were significantly different compared to the other conditions except in the medial-lateral direction.

For the LUCL and the RCL deficient cases, no elbow dislocations occurred (Fig. 4.4), but when both the LUCL and RCL ligaments were sectioned the joint was significantly distracted at 40° of flexion and a complete dislocation occurred at approximately 110° of flexion. When the term posterolateral rotatory instability was first described by O'Driscoll et al. (1991), they concluded that the laxity of the LUCL was the cause for this condition. Our study demonstrates that, keeping the annular ligament and the RCL intact while sectioning the LUCL produces some posterior laxity of the joint but does not produce dislocation of the elbow. This observation concurs with the findings of a cadaveric experimental study by Dunning et al. (2001). They reported that sectioning the LUCL initiated more joint laxity than sectioning the RCL, but did not produce complete joint instability until both of them were sectioned together. Hannouche and Begue (1999) also reported that sectioning of the LUCL resulted in only minor elbow laxity where sectioning both LUCL and RCL produced complete ulnohumeral subluxation. A series of studies done by Olsen et al. that investigated the effects of the lateral ligamentous structures on elbow joint kinematics (Olsen, Sojbjerg, et al., 1996; Olsen et al., 1998; Olsen, Vaesel, et al., 1996) demonstrated that transection of the joint capsule and the LUCL did not produce marked laxity until the whole lateral ligament complex was sectioned. Our results are in agreement with their finding that varus-valgus, and internal-external rotations increased dramatically after the entire lateral collateral ligament was sectioned.

Our model also revealed an interesting trend for the LUCL and RCL deficient cases (Fig. 4.3). It suggests that the LUCL may provide somewhat greater varus-valgus and internal-external rotational stability than the RCL. This finding appears to support the results of previous studies indicating the importance of the lateral ulnar collateral ligament in preventing posterolateral rotatory instability of the elbow (O'Driscoll et al., 1991; O'Driscoll, Horii, et al., 1992; O'Driscoll, Morrey, et al., 1992). Dunning et al. (2001) reported that posterior rotatory instability induced external rotation of more than 15°, and our findings concur. However, we observed slightly higher than 15° of external rotation for the intact, RCL, and LUCL deficient cases, especially at deep flexion angles. The reasons for this discrepancy could be the non-inclusion of muscle and other soft tissues in our model that may have allowed slightly higher joint rotations. Furthermore, we report the rotations of the ulna and radius separately instead of combining them into a resultant lower arm rotation as done in other studies. O'Driscoll et al. (1991) noted that for the case of posterolateral rotatory instability the ulna undergoes maximum external rotation at approximately 40° of flexion and additional flexion reduced it. Our model predicted similar trend of motion, however we found maximum ulna external rotation at 70° of elbow flexion during both deficient elbow (Fig. 3.3). This observation closely agrees with the data of Dunning et al. (2001), who demonstrated that external rotation of the ulna relative to the humerus increased until 90° of elbow flexion.

Although contact area patterns were not validated experimentally, our predicted intact contact pressure pattern at 20° flexion is in good agreement with the findings of an experimental and finite element study by Willing et al. (2013). Furthermore, our predicted ulnohumeral contact and non-contact areas are consistent with the contact patterns reported by Eckstein et al. (1995).

Peak ligament loads for the intact elbow revealed that the MCL bundles carry more resistive loads compared to the LCL bundles. MCL bundles carried 2-3 times more ligament load than the LCL. Among the MCL bundles, the anterior bundle carried almost double the load of the posterior bundles. For the LUCL deficient case, a significant increase in the RCL load was observed. These results indicate that in the absence of the LUCL, the RCL supports most of the load of the lateral collateral ligament complex. The small reduction in the MCL ligament load observed for the LUCL deficient case may be the result of elbow subluxation due to the ligament deficiency. Again, consistent with the rest of our results, the RCL deficient case did not induce any significant load changes to the remaining ligaments. Ligament loads were significantly reduced for both the MCL bundles when both the LUCL and RCL were sectioned as the joint experienced posterolateral rotatory instability and complete dislocation.

Even though the computational model used in this study has been shown to accurately represent a true elbow joint in terms of kinematics, there are several limitations and differences between the model and experimental studies. The model is based on a single cadaver specimen and therefore characteristic of a single elbow. The ligament deficiencies investigated here can give us insight into the role of the lateral complex in elbow stability but experimental validation studies involving larger sample sizes are required to generalize the conclusions. The computational model itself also has limitations. In particular, the discretized cartilage parameters and discrete cartilage size was not optimized for the current model but estimated using elastic foundation theory. Future studies will optimize contact parameters and discretized cartilage size by matching the multibody cartilage model to a finite element model. Even with this limitation, our maximum contact pressures were close in range (0.5 – 5 MPa) to the values reported by Brand (2005). Reference strain at which the ligament force-length relationship (Eq. 4.1) transformed from quadratic to linear function has obtained from a computational knee study (Li et al., 1999). Morrey and An (1983) reported that the anterior and posterior capsule provided 32% varus and 33% valgus elbow stability respectively at full extension. The joint capsule works as a secondary static elbow stabilizer and the greatest contribution occurs with the elbow extended (de Haan et al., 2011). Our model did not incorporate the joint capsule contribution to joint stability and that may be one of the reasons for the slightly higher laxity observed in our results. M. S. Cohen and Hastings (1997) reported that the muscles and fascia overlaying the lateral collateral ligament provide an important stabilizing influence against rotatory displacement in the elbow. Our model did not employ muscles or fascia, so the stabilizing influence of these muscle tissues was not quantified in this study. Future studies will incorporate elbow crossing muscles in the model. Wrapping of the ligaments around bony structures was achieved by creating via points where the lines of action for the ligaments would have to pass through. Since the ligaments are modeled as force elements the thickness of the ligaments is not taken into account. Future refinements of this model will include optimization of the discrete cartilage representation, and inclusion of muscles and the joint capsule.

The primary objective of this study was to compare the effects of different combinations of LCL complex deficiency on ligament and contact loads using an anatomical computational multibody model of the elbow joint. Detailed knowledge of the effects of LCL complex deficiency can be of great importance to orthopaedic surgeons planning surgical approaches to the elbow for ligament and fracture repairs or arthroplasty (Morrey, 2000). Our results also concur with the literature with regards to the role of the LUCL in posterolateral rotatory instability since the LUCL has greater influence on the kinematics and contact pressures than the RCL. This current study is a first step in studying ligament deficiency in an anatomically correct computational model of the elbow joint. Anatomically correct computational models are widely used in knees but such models have been under-utilized in elbow studies. The advantages of the multibody modeling framework presented here outweigh its limitations. The model does not constrain the degrees of freedom of the joint, instead three dimensional cartilage contacts capable of contact pressure and contact area predictions along with ligament constraints allow a total of twelve degrees of freedom for the elbow joint (6 for the ulna-humerus articulation and 6 for the radius-humerus articulation). This modeling approach is capable of computing parameters that are very difficult to measure experimentally such as ligament forces, contact pressure distributions, and bone kinematics in a computationally efficient way. Ultimately, such models can be of great use in delivering objective, data-driven, patient-specific care.

CHAPTER 5

A MODELING APPROACH TO SIMULATING MEDIAL COLLATERAL LIGAMENT DEFICIENCY OF THE ELBOW JOINT

5.1 Introduction

Elbow dislocations are very common in adults and children and represent 11-28% of all elbow injuries at an average annual rate of 6-13 cases per 100,000 population (Alolabi et al., 2012; Hildebrand et al., 1999). Therefore, the elbow joint has been an important focus of biomechanics research. Dislocations of the elbow can be simple, where the dislocation occurs with the medical collateral ligament (MCL) and/or lateral collateral ligament injury or can be complex, where the dislocation causes both ligament injury and fracture of the articular surface (Hildebrand et al., 1999).

The medial collateral ligament (MCL) provides resistance to valgus motion of the elbow joint. Although the bone articulation contributes to stability, the MCL complex provides the major medial elbow stabilization. For acute elbow dislocation, MCL injury has been reported as high as 100% (Josefsson, Gentz, Johnell, & Wendeberg, 1987). Occupations or activities where elbows placed under repetitive valgus load can produce MCL microtears and eventually complete disruption of the MCL (Armstrong et al., 2000). Injury to the MCL produce chronic pain in the medial aspect of the elbow and can result in problems in other areas such as the ulnar nerve, the flexor-pronator musculotendinous unit, the radiocapitellar joint, and the posterior compartment of the elbow (Safran et al., 2005). MCL deficiency can cause significant joint morbidity and may end the career for overhead athletes such as baseball pitchers, and javelin throwers.

Simulating medial collateral ligament deficiency in a computer model would be immensely valuable tools for surgical planning and refinement of rehabilitation regimens. Such models would allow us to examine efficient ligament reconstruction techniques by pre-operative assessment and to investigate better rehabilitation post-operative protocols. Literature reviews reveal that computer models have been employed effectively to measure articular cartilage contact pressure distribution, examine muscle and ligament function, investigate joint stability, and injury mechanism(Gonzalez et al., 1996; Kwak, Blankevoort, & Ateshian, 2000; Lemay & Crago, 1996; Li et al., 1999; Willing et al., 2014). Computer models provide flexibility in analyzing different clinical scenarios and are capable of measuring and calculating important parameters that are difficult or not possible to capture experimentally such as ligament force and cartilage contact pressure.

Anatomically, the MCL complex has three components: the anterior, the posterior, and the transverse bundles (Fig.5.1). The anterior bundle originates from the medial epicondyle of the humerus and attaches to the sublime tubercle on the coronoid process of the ulna. The posterior bundle also originates from the humerus medial epicondyle and generally inserts more posteriorly along the medial aspect of the olecranon. The transverse ligament originates from the   ulna and inserts to the ulna. This ligament currently has no known function, therefore, was not included in our study (Morrey, 2000).

The main objective of this study was to simulate medial collateral ligament deficiency in a computational, anatomically correct multibody elbow joint model. Four cases were simulated in this study: (i) keeping all ligament intact (‘Intact’ model) (ii) isolated MCL anterior bundle deficiency (MCL AB deficient) (iii) isolated MCL posterior bundle deficiency (MCL PB deficient) (iv) and combined MCL anterior and posterior bundle deficiency (Both MCL deficient). For each ligament deficiency condition, kinematics, contact area, contact pressure, and ligament forces were calculated and compared to the intact model simulation.

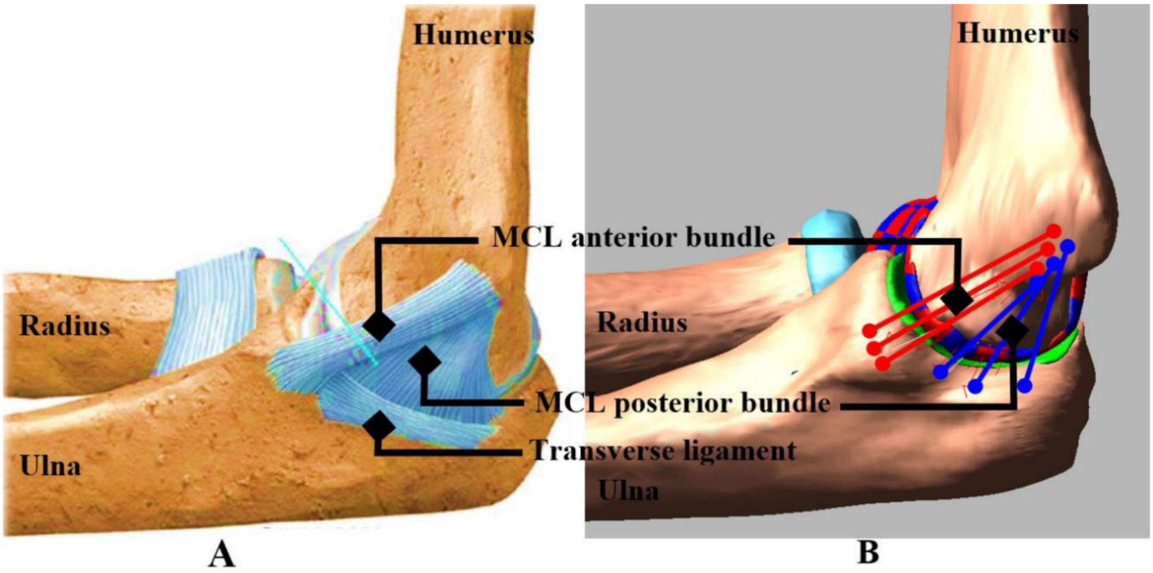

Figure 5.1. (a) Medial collateral ligament (MCL) complex consists of the MCL anterior bundle, MCL posterior bundle, and transverse ligament, and (b) corresponding ligament representation in the model

5.2 Materials and methods

Two previously developed multibody models created from cadaver specimens (Specimen#1, 61year old, male, right arm; Specimen#2, 42 years old, male, right arm) were used for this study (Rahman, Cil, & Stylianou, 2016). The multibody models were created in the commercially available multibody dynamic analysis program ADAMS (MSC Software Corporation, Santa Ana, CA). The three-dimensional geometries of bones and cartilages were derived from computed tomography (Siemens, Siemens Medical Solutions, PA) and magnetic resonance images (Siemens 3T machine with a narrow field fine resolution setting). The program 3D Slicer (www.slicer.org) was used to generate the geometries by using auto threshold segmentation. The geometries were post processed in Geomagic Studio (Geomagic, Inc., Research Triangle Park, NC, USA) that included removing the spikes and noise, and decimating the geometries to reduce the file size. The geometries were then imported and aligned in ADAMS by using the initial position measurements acquired during the cadaver testing. The specimens were placed at forearm pronated position and, 20º initial flexion for specimen 1 and 45º initial flexion for specimen 2 (Fig. 5.2). The humerus was attached with a translational joint to the ground. The radius and ulna were connected to each other through the interosseous membrane, and the distal and proximal radioulnar joint. A spherical joint was placed between hand and radius to represent the wrist joint. The hand was attached to a fixed plate on the ground through a six axis spring. The density of 1600 kg/m^3 (Donahue et al., 2002) was applied for bones and 1000 kg/m^3 (Zielinska & Donahue, 2006) was applied for cartilages.

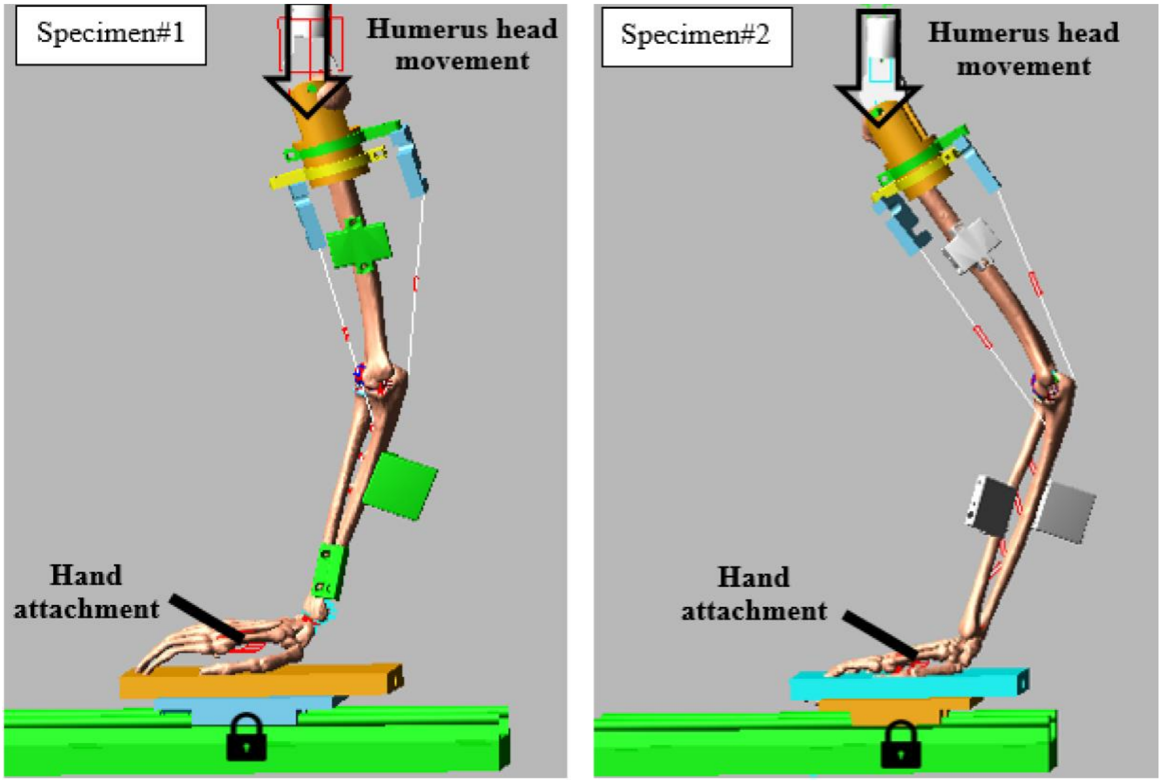

Figure 5.2. Multibody models of the specimens

Instead of defining a single contact force, the humerus cartilage was sectioned into discrete elements to calculate contact pressure distribution (Rahman, Cil, & Stylianou, 2016) (Fig. 5.3). Briefly, a custom macro written in ADAMS automatically divided the humerus cartilage into discrete hexahedral elements with an approximate cross-sectional area of 5 x 5 mm and connected each cartilage element to the distal humerus surface with a fixed joint. The ulna and radius cartilages were rigidly attached to the respective bone articulating surfaces using fixed joints. The macro defined deformable contact constraints between each humerus cartilage element and the radius and ulna cartilage geometries using the modified Hertzian contact law (Eq. 5-1) (Machado et al., 2012).

$$F_c = k_c \delta^n + B_c(\delta)\dot{\delta} \qquad 5\text{-}1$$

where F_c is the contact forces, k_c is the contact stiffness, δ is the interpenetration of the geometries, $\dot{\delta}$ is the velocity of interpenetration, n is the nonlinear power exponent, and $B_c(\delta)$ is a damping coefficient. The damping coefficient is defined as function of interpenetration to prevent discontinuities in the forces of first contact (Hunt & Crossley, 1975).

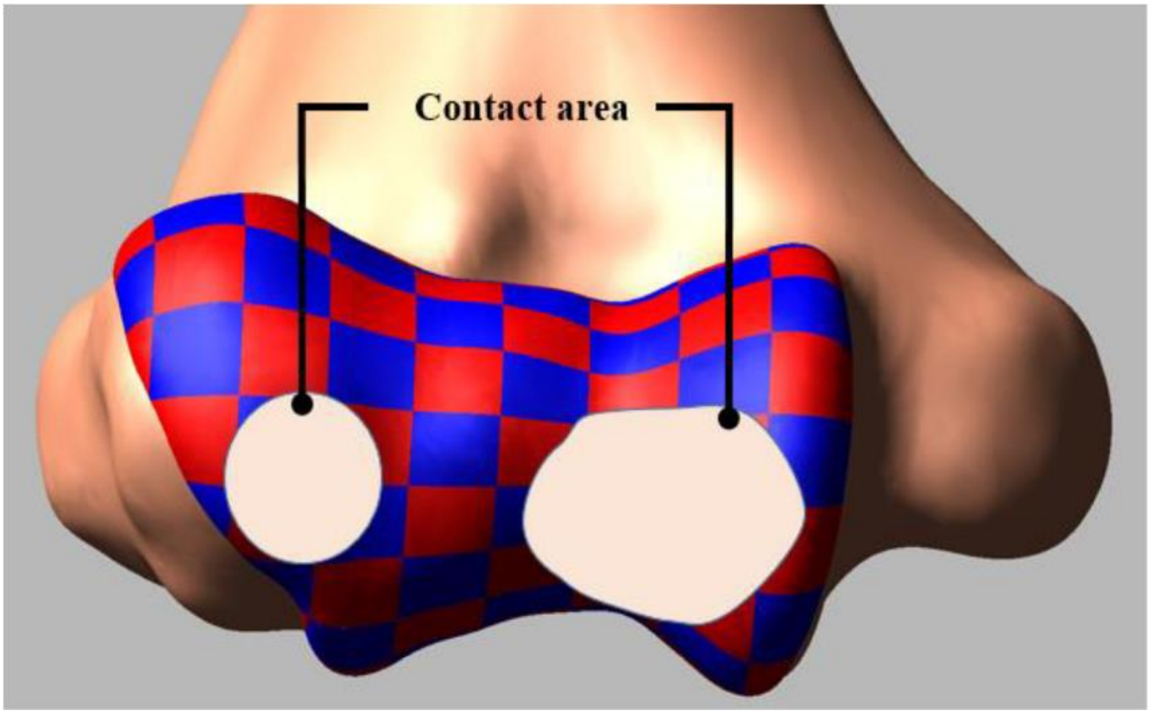

Figure 5.3. Discretized humerus cartilage.

Elastic foundation theory was used to estimate the contact parameters (Bei & Fregly, 2004; Blankevoort et al., 1991).

$$p = \frac{(1-\nu)E}{(1+\ \nu)(1-2\nu)h}\, d \qquad 5\text{-}2$$

where E is Young's modulus, ν is Poisson's ratio, h is the combined cartilage thickness in articulation, and d is the spring deformation. The contact pressure p was computed for the values of $E = 0.7$ MPa (Athanasiou et al., 1991), $\nu=0.495$, $h= 4, 4.8, 3.07, 3.58$ (for humerus–ulna and humerus– radius articulation of specimen 1 and 2 respectively) with d as an unknown spring deformation. Since the humerus cartilage was discretized in 5 x 5 mm, the value of p/d was then multiplied by 25mm^2 to estimate contact stiffness (Rahman, Cil, & Stylianou, 2016).

The ligaments and interosseous membranes were represented as single force elements with nonlinear force-strain curves including the non-linear "toe" region. The attachment sites and orientations were identified and digitized using an Optotrak probe (NDI, Waterloo, Ontario, Canada) during dissection by a shoulder and elbow fellowship trained orthopaedic surgeon, anatomical atlases (Netter & Hansen, 2003), and published studies (Fisk & Wayne, 2009; Morrey, 2000; Morrey & An, 1985; Skahen et al., 1997; Spratley & Wayne, 2011). The model included three bundles for the MCL anterior band, three bundles for the MCL posterior band, three bundles for the lateral ulnar collateral ligament (LUCL), three bundles for the radial collateral ligament, and two bundles for the annular ligament. The force length relationship of each ligament is described by (Blankevoort et al., 1991):

$$f = \begin{cases} \frac{1}{4} k\, \varepsilon^2 / \varepsilon_l & 0 \le \varepsilon \le 2\varepsilon_l \\ k(\varepsilon - \varepsilon_l) & \varepsilon > 2\varepsilon_l \\ 0 & \varepsilon < 0 \end{cases} \qquad \text{5-3}$$

$$\varepsilon = \left(\frac{l - l_0}{l_0}\right) \qquad \text{5-4}$$

where *k* is a stiffness parameter, *ε* is the engineering strain of each ligament part, ε_l is a spring parameter assumed to be 0.03 (Li et al., 1999), *l* is ligament bundle length, and l_0 is the zero-load length. The stiffness parameters *k* was obtained from Fisk and Wayne (2009), and Regan et al. (1991). The l_0 was estimated based on previous cadaveric studies performed by Rahman, Cil, and Stylianou (2016). Each ligament force also included a parallel damper with damping coefficient of 0.5 Ns/mm to remove the possibility of high frequency vibration during simulation (Guess et al., 2010). Ligament wrapping around the bone of LUCL and annular ligament was employed to better represent the ligament force's lines of action. Constant muscle tension of 40N for the triceps and 20N for the brachialis were applied in the model to provide some muscle stabilization (Fisk & Wayne, 2009; Morrey et al., 1991).

Simulated bone motions were measured by defining local coordinate systems for each bone segment as described by Ferreira et al. (2011), and Morrey and Chao (1976). The three translations and rotations of the radius and ulna were computed relative to the humerus. The translations were represented as medial–lateral (M–L), anterior–posterior (A–P), and superior-inferior (S-I) direction and the rotations were represented as flexion-extension (F-E), varus-valgus (VR-VL), and internal-external (I-E) rotation (Rahman, Cil, Bogener, & Stylianou, 2016; Rahman, Cil, & Stylianou, 2016). Vertical downward motion profile of 345mm and 334mm were applied to the humeral head of specimen 1 and 2 respectively for 40 seconds. The motion profiles induced the maximum flexion angle of about 135° for both specimens. To simulate the MCL deficient conditions, the respective ligament bundles were removed from the model. All ligament deficient conditions and the intact elbow were subjected to the same motion profile for a particular specimen.

Kinematic difference between the ligament deficient case and the intact case were used as outcome measures. The differences were calculated for every two degree of flexion angle from the range of 50° to 130° flexion. So, within this 80° flexion range a total 40 sample data points were obtained for each ligament condition to calculate the statistical significance. Statistical analysis was performed using a one-way analysis of variance (ANOVA), with ligament state as variables. Then multiple pairwise comparison test was performed to find the significance difference between groups. Significance was defined at $p \leq 0.01$.

5.3 Results

5.3.1 Kinematic comparison

For both specimens, some ulna and radius kinematics were significantly different for isolated MCL AB and PB deficiency. However, the magnitudes were very small and likely to be clinically insignificant (Tables 5.1-5.2). Sectioning both of them together generated significant differences in almost all elbow joint kinematics.

Table 5.1. Mean kinematics difference ± standard deviation (statistical p-values) between ligament deficient and intact elbow for specimen 1

	Ligament Conditions	I-E (deg)	VR-VL (deg)	S-I (mm)	A-P (mm)	M-L (mm)
Ulna Kinematics	MCL AB Deficient	1.44±0.36 (0.19)	1.18±0.08 (<0.01*)	0.10±0.35 (0.93)	0.73±0.17 (< 0.01*)	-0.28±0.23 (0.94)
	MCL PB Deficient	2.24±0.73 (0.02)	0.40±0.08 (<0.01*)	-0.08±0.06 (0.96)	0.20±0.09 (0.49)	0.15±0.04 (0.99)
	Both MCL Deficient	23.72±6.50 (<0.01*)	2.61±0.76 (<0.01*)	-4.19±1.46 (<0.01*)	2.61±1.26 (<0.01*)	-4.71±4.62 (< 0.01*)
Radius Kinematics	MCL AB Deficient	1.91±0.16 (<0.01*)	0.97±0.07 (<0.01*)	0.43±0.07 (<0.01*)	-0.13±0.19 (0.95)	-0.47±0.15 (0.61)
	MCL PB Deficient	1.41±0.47 (<0.01*)	0.22±0.03 (<0.01*)	0.20±0.05 (0.41)	-0.11±0.11 (0.97)	-0.21±0.90 (0.94)
	Both MCL Deficient	11.42±2.25 (<0.01*)	1.93±0.57 (<0.01*)	2.24±1.14 (<0.01*)	-1.78±2.13 (<0.01*)	-4.21±3.44 (<0.01*)

[I-E= internal-external rotation; VR-VL= varus-valgus rotation; S-I=superior-inferior translation; A-P=anterior-posterior translation; M-L=medial-lateral translation. Positive values indicate more internal for I-E, and more valgus rotation for VR-VL than intact elbow. Similarly, positive values indicate more superior for S-I, more anterior for A-P, and more medial translation for M-L than intact elbow. Negative values indicate the opposite. The asterisk (*) for p-values indicates significance ($p \leq 0.01$)].

Table 5.2. Mean kinematics difference ± standard deviation (statistical p-values) between ligament deficient and intact elbow for specimen 2

	Ligament Conditions	I-E (deg)	VR-VL (deg)	S-I (mm)	A-P (mm)	M-L (mm)
Ulna Kinematics	MCL AB	2.29±0.79	0.99±0.32	-0.23±0.17	0.61±0.35	-0.21±0.31
	Deficient	(<0.01*)	(<0.01*)	(0.38)	(0.35)	(0.78)
	MCL PB	1.17±0.64	0.17±0.16	-0.10±0.03	0.09±0.14	0.05±0.14
	Deficient	(0.03)	(0.13)	(0.89)	(0.99)	(0.99)
	Both MCL	26.89±3.78	4.14±0.62	-6.87±1.27	1.97±3.33	-8.31±2.01
	Deficient	(<0.01*)	(<0.01*)	(<0.01*)	(<0.01*)	(< 0.01*)
Radius Kinematics	MCL AB	2.73±0.77	0.82±0.26	0.41±0.10	-0.07±0.14	-0.43±0.34
	Deficient	(<0.01*)	(<0.01*)	(<0.01*)	(0.47)	(0.24)
	MCL PB	0.84±0.66	0.10±0.12	0.12±0.10	-0.05±0.06	-0.07±0.11
	Deficient	(<0.01*)	(0.06)	(0.41)	(0.73)	(0.99)
	Both MCL	-3.22±1.17	0.28±0.49	-0.05±42	-0.68±0.41	-8.83±2.06
	Deficient	(<0.01*)	(<0.01*)	(0.70)	(<0.01*)	(<0.01*)

[I-E= internal-external rotation; VR-VL= varus-valgus rotation; S-I=superior-inferior translation; A-P=anterior-posterior translation; M-L=medial-lateral translation. Positive values indicate more internal for I-E, and more valgus rotation for VR-VL than intact elbow. Similarly, positive values indicate more superior for S-I, more anterior for A-P, and more medial translation for M-L than intact elbow. Negative values indicate the opposite. The asterisk (*) for p-values indicates significance ($p \leq 0.01$)].

For both specimens, bone kinematics for different ligament conditions are presented at increments of 10º flexion from 50º to 130º flexion range (Fig. 5.4-5.5). Consistent with the previous observation, ulna and radius kinematics for both specimens were significantly different for both MCL deficient elbow. When the entire MCL bundle was sectioned, maximum ulna internal rotation was more than 30º at deep flexion, indicating significant elbow instability. With that, the ulna also laterally translated for more than 8mm.

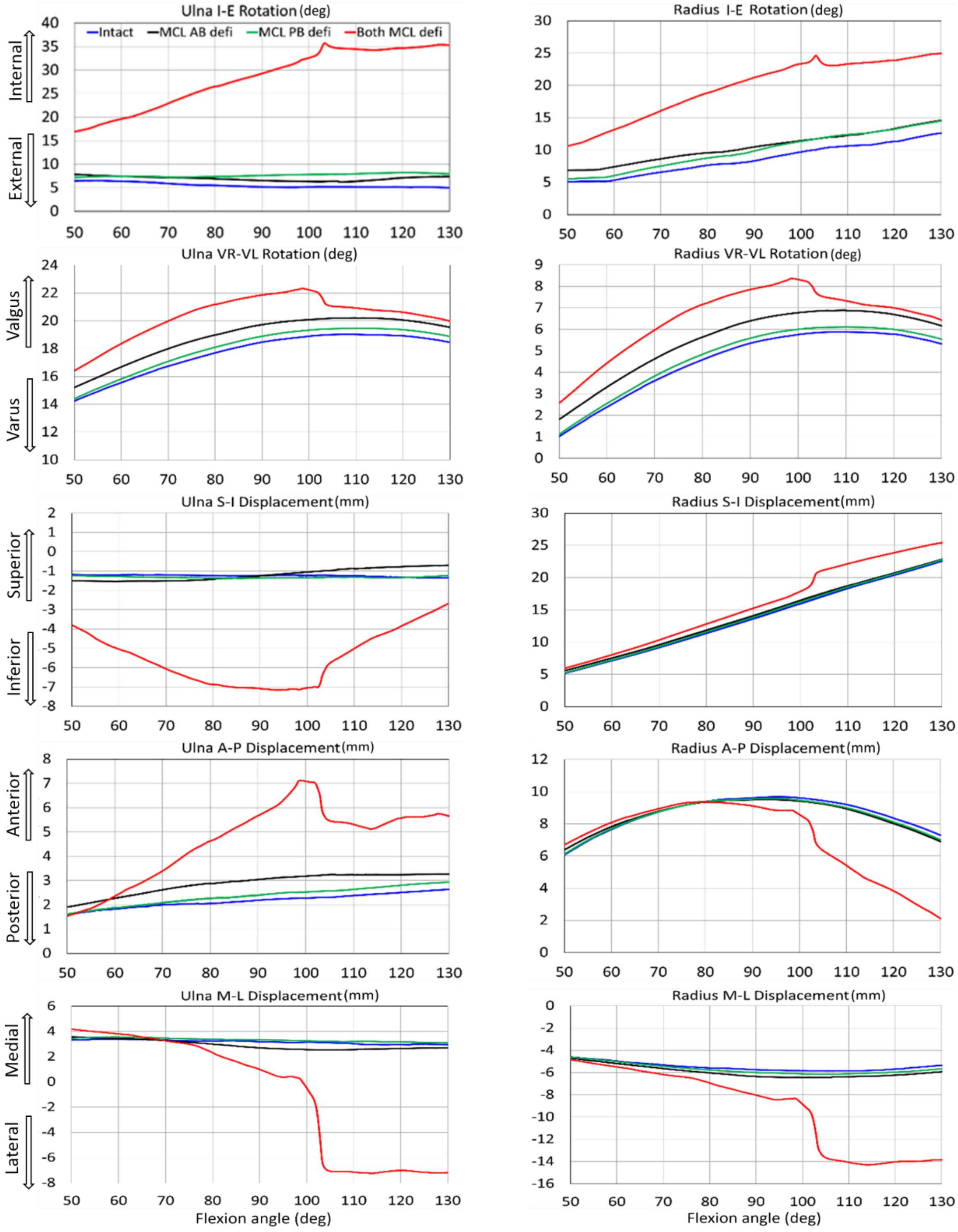

Figure 5.4. Effect of medial collateral ligament deficiency on ulna and radius kinematics relative to humerus for specimen 1.

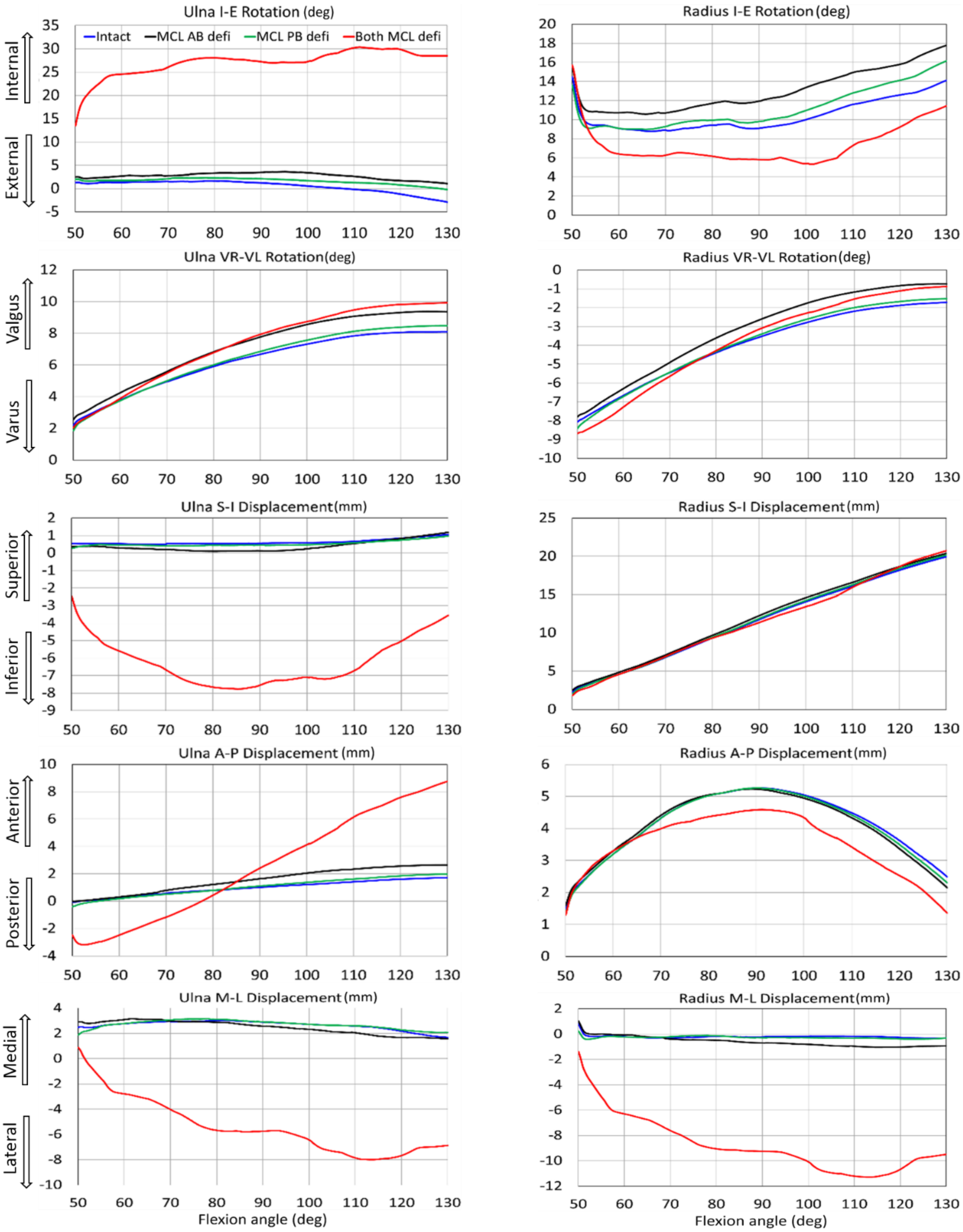

Figure 5.5. Effect of medial collateral ligament deficiency on ulna and radius kinematics relative to humerus for specimen 2.

Complete elbow dislocations were not observed for any ligament deficient cases. However, the joint was significantly distracted at around 80º of flexion when the entire MCL bands were sectioned and continuously reduced with increasing the flexion angle (Fig. 5.6-5.7).

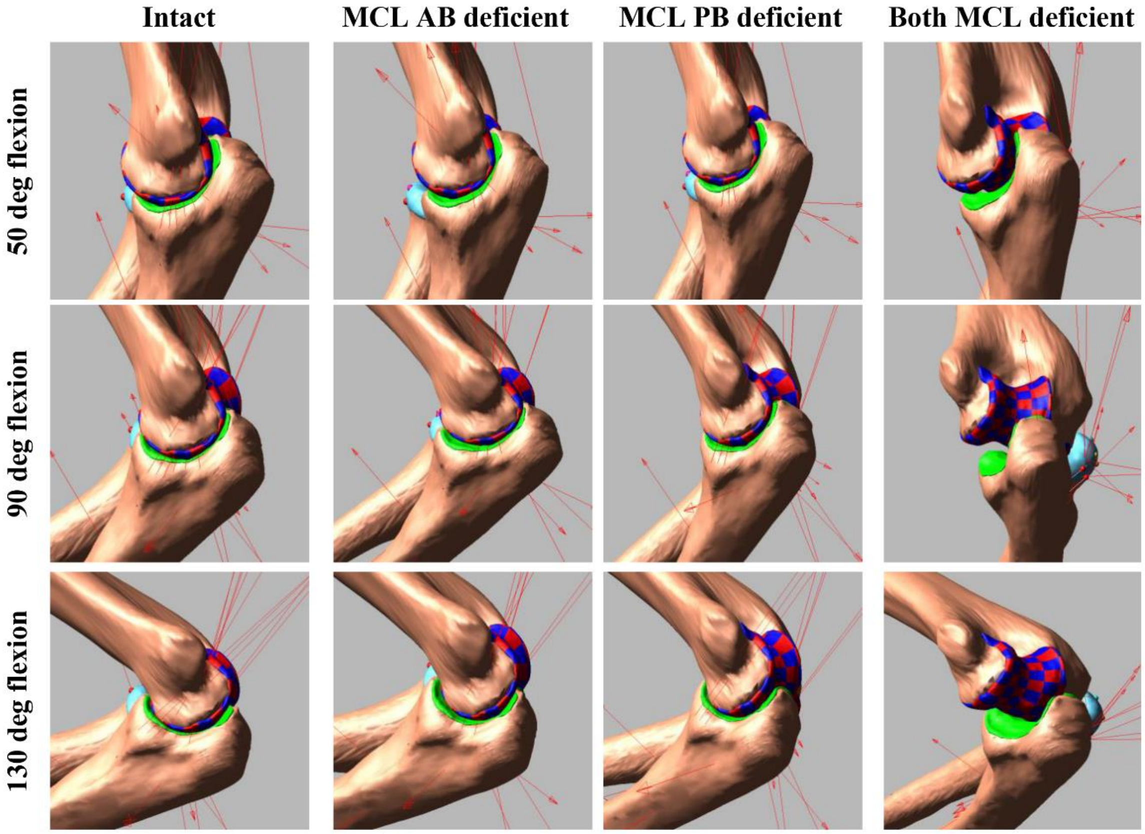

Figure 5.6. Elbow joint configuration at different flexion angles for specimen 1. Red arrows indicate the force vector from ligaments and contacts.

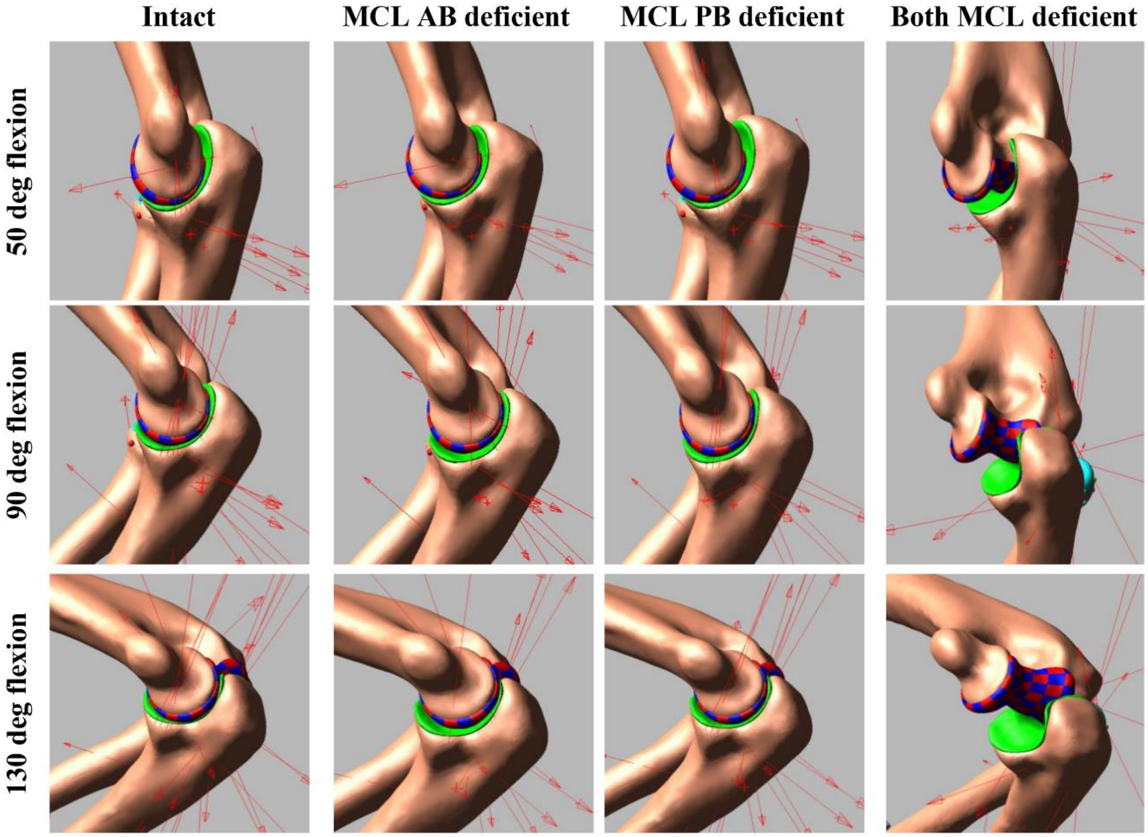

Figure 5.7. Elbow joint configuration at different flexion angles for specimen 2. Red arrows indicate the force vector from ligaments and contacts.

5.3.2 Contact area and pressure comparison

Contact pressure distributions on humeral cartilage changed noticeably for different ligament deficient conditions compared to intact elbow (Fig. 5.8- 5.9). Contact patches were almost identical for intact and MCL PB deficient elbow; minor differences were observed for the MCL AB deficient case. The most significant change in contact characteristics occurred for the entire MCL deficient case for both specimens. In this case, the joint contact was significantly absent on the medial cartilage indicating significant distraction of the joint. Maximum contact pressure for specimen 1 was 5.2 MPa for intact, 4.4 MPa for MCL AB, 4.3 MPa for MCL PB, and 2.8 MPa for both MCL deficient case. For specimen 2, maximum contact pressure was 4.4 MPa for intact, 3.9 MPa for MCL AB, 3.7 MPa for MCL PB, and 3.7 MPa for both MCL deficient case. Maximum contact pressure was observed in medial cartilage for intact, MCL AB, and MCL PB cases, and shifted to lateral side for entire MCL tear cases. Contact patches were moved from posterior to anterior direction as the joint flexion angle increased.

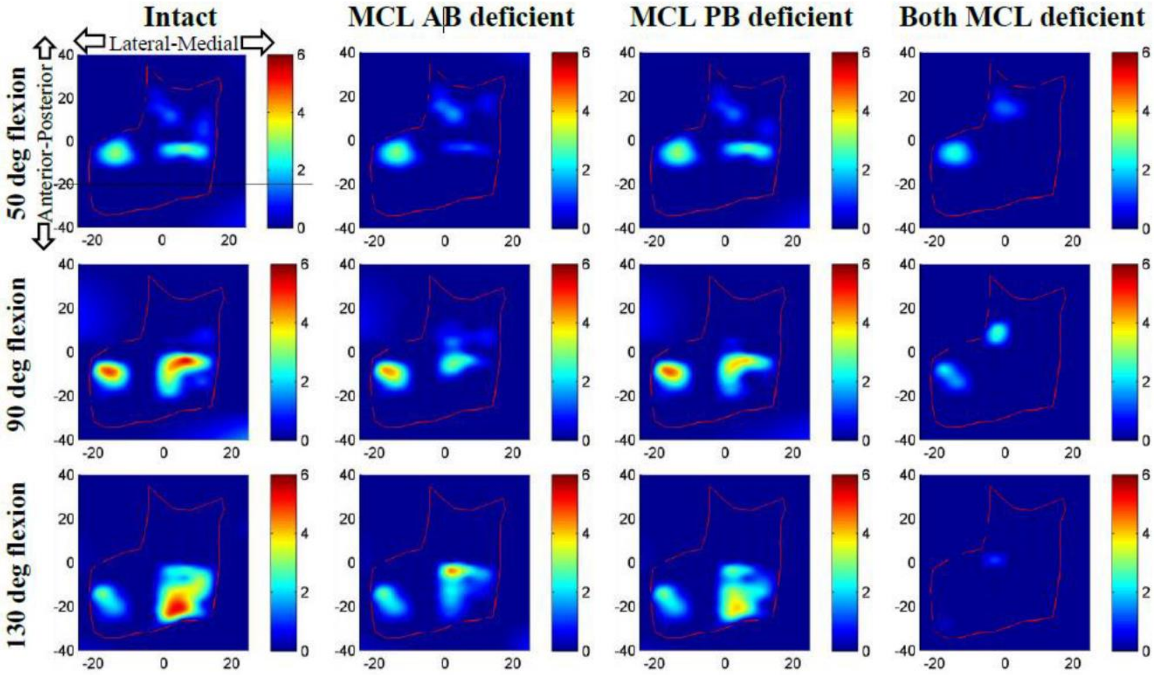

Figure 5.8. Contact pressure distribution on humerus cartilage for specimen 1.

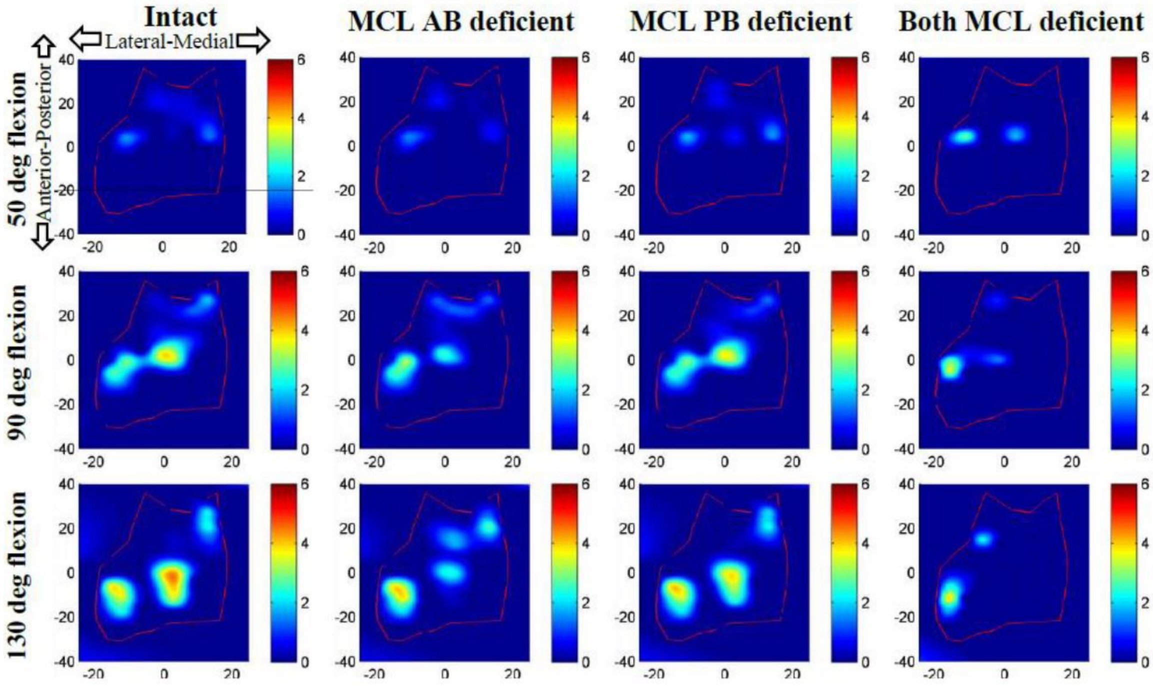

Figure 5.9. Contact pressure distribution on humerus cartilage for specimen 2.

5.3.3 Ligament load comparison

Peak loads for MCL PB ligament considerably increased for the MCL AB deficient elbow (Table 5.3-5.4). Similarly, for the MCL PB deficient elbow, peak loads for MCL AB ligament increased. Peak loads for other intact ligaments substantially decreased for complete MCL deficiency.

Table 5.3. Maximum intact ligament loads and strains for specimen 1

Ligament Band	Intact		MCL AB Deficient		MCL PB Deficient		Both MCL Deficient	
	Peak Load (N)	Max. Strain	Peak Load (N)	Max. Strain	Peak Load (N)	Max. Strain	Peak Load (N)	Max. Strain
Lateral ulnar collateral ligament	62	0.13	59	0.13	54	0.12	44	0.10
Radial collateral ligament	24	0.11	20	0.10	19	0.10	23	0.11
MCL anterior band	211	0.50	-	-	224	0.53	-	-
MCL posterior band	118	0.44	140	0.52	-	-	-	-

Table 5.4. Maximum intact ligament loads and strains for specimen 2

Ligament Band	Intact		MCL AB Deficient		MCL PB Deficient		Both MCL Deficient	
	Peak Load (N)	Max. Strain	Peak Load (N)	Max. Strain	Peak Load (N)	Max. Strain	Peak Load (N)	Max. Strain
Lateral ulnar Collateral ligament	53	0.11	45	0.10	49	0.11	31	0.08
Radial collateral ligament	20	0.10	16	0.09	18	0.09	43	0.18
MCL anterior band	170	0.40	-	-	181	0.43	-	-
MCL posterior band	65	0.26	95	0.36	-	-	-	-

5.4 Discussion

This study investigated the elbow joint behavior during passive flexion in the presence of medial collateral ligament deficiency in a computer model. Two previously validated anatomically correct computational multibody elbow joint models were used for this study (Rahman, Cil, & Stylianou, 2016). The computational models were created from the subject specific bones and cartilage geometries derived from medical images and validated through the experimental cadaver tests. The joints were constrained by non-linear ligaments including ligament zero load length. The ligaments were wrapped around the joint for better representation of ligament physiology and line of action. The model includes discretized humerus cartilage that allows computation of contact pressure distribution and contact area.

Several studies have examined the effect of medial collateral ligament injury in the human elbow joint by using *in vitro* cadaver experiment (Alolabi et al., 2012; Armstrong et al., 2000; Pichora et al., 2007). However, computer model investigation of these injuries is very limited in literature. The advantages of computer models are that they provide flexibility in analyzing different clinical scenarios and can predict what cannot be directly measured such as ligament loading and cartilage contact pressure. This information would allow pre-operative assessment of which ligament should actually be reconstructed, and the anticipated cartilage loading to prevent cartilage degeneration and osteoarthritis. Such pre-operative planning would allow for the most efficient treatment and possibly less invasive surgery of the elbow injury, and may lead to the development of newer elbow ligament reconstruction techniques.

On average, in our study the mean kinematics differences for MCL AB deficient elbow were slightly larger than MCL PB deficient conditions (Table 5.1-5.2). This observation indicates that MCL AB ligament has somewhat bigger influence on kinematic constraints than MCL PB ligament. However, the joint was completely in contact over the simulation period for both cases as there was no valgus stress applied to the elbows. The joint was significantly distracted only when the entire MCL bundle was sectioned even if there was no valgus stress.

The kinematics was slightly varied between the two specimens. Also, ulna translated more laterally for specimen 1 at about 100º flexion, causing a sudden spike in results. The reason of this variation was the differences of initial positioning between the two specimens, along with some geometrical variation among them. Because of the variability between the subjects, other results were also slightly varied.

Our study observed that when the entire MCL bundle was disrupted, ulna generated the maximum internal rotation of about 30-35º (Fig. 5.4-5.5). This result was in good agreement with the cadaveric experimental study reported by Armstrong et al (Armstrong et al., 2000). In their study they demonstrated that for a passive motion of a pronated forearm, the arm rotated internally about 30-35º when the entire MCL bundle was sectioned. However, their reported maximum varus-valgus laxity was about 40-50º, which was higher than our observed maximum valgus rotation of about 20º. The reason of this discrepancy was the difference between their testing system and our model boundary conditions. In their experimental setup, the arm was placed in a gravity loaded position to observe the varus-valgus laxity after sectioning MCL. On the other hand, we placed the arm in a vertical positioned and simulated elbow flexion by providing vertical motion to the humeral head (Fig. 5.2).

None of the ligament deficient conditions induced complete elbow dislocation (Fig. 5.6-5.7). However, entire MCL bundle deficiency significantly reduced elbow stability. Ligament deficiency also induced significant changes to the contact pattern over the simulation period (Fig. 5.8-5.9). Contact area patterns were almost identical for the intact and the MCL PB deficient condition over the simulation period, but this ligament deficiency induced reduction of the peak joint contact pressure, signifying a small amount of joint laxity. On the other hand, contact area pattern and peak contact pressure were markedly different for the MCL AB deficient elbow compared to the intact elbow, indicating joint subluxation. The most important change in the contact area occurred in the both deficient case with significant loss of contact in medial humerus and medial joint distraction. However, the radial head kept contact with the capitellum for all cases.

Peak ligament loads increased for the MCL posterior bundle when the MCL anterior bundle was sectioned (Table 5.3-5.4). This result indicates that in the absence of the anterior bundle, the posterior bundle carried part of the joint load from the anterior side. A similar trend was observed for the MCL PB deficient case where the anterior bundles loads were increased in the absence of the posterior bundle. Peak ligament loads of the lateral collateral ligament complex were less influenced by the MCL deficiency. When the entire MCL bundle was removed peak load decreased in almost all intact ligaments. This is due to the fact that in this ligament deficiency condition the elbow joint opens up in the medial side thus causing a narrowing on the lateral side.

A potential limitation of the present study was that the model did not employ any muscles or fascia. Stabilizing influences from these tissues were not quantified in this study. As reported by An et al. (An, Hui, Morrey, Linscheid, & Chao, 1981) and King et al.(King et al., 1993), muscle loading applied to the elbow during active motion allows axial compressive forces at the joint to enhance joint stabilization. Our study analyzed passive flexion, so muscle stabilizing effects should be less influential. Morrey et al. (Morrey & An, 1983) reported that the anterior and posterior capsule provided 32% varus and 33% valgus elbow stability respectively at full extension. The joint capsule works as a secondary static elbow stabilizer and the greatest contribution occurs with the elbow extended (de Haan et al., 2011). Our model did not incorporate the joint capsule contribution to joint stability and therefore laxity effects may be exaggerated. Future studies will incorporate elbow crossing muscles along with capsule’s stability in the joint.

Secondly, the discretized cartilage contact parameters and discrete cartilage size was not optimized for the current model but estimated based on simplified elastic foundation theory. As reported in a recent study by Willing et al. (2013), accurate selection of material properties is significant for calculating cartilage contact pressures when using a finite element model. Future studies will optimize contact parameters and discretized cartilage size by matching a multibody cartilage model with a finite element model of the same cartilage. Even with this limitation, our maximum contact pressures were close in range (0.5 - 5Mpa) to the values reported by Brand (2005). The predicted intact contact areas at 20º flexion are in good agreement with the findings of a static finite element model by Willing et al. (2013). Furthermore, our predicted ulnohumeral contact and non-contact areas were consistent with the contact patterns reported by Eckstein et al. (1995).

The primary objective of this study was to compare the effects of different combinations of MCL complex deficiency on joint kinematics, contact characteristics, and ligament load by using a computational multibody elbow joint model. The study simulated the passive elbow flexion for intact, MCL AB deficient, MCL PB deficient, and both MCL deficient conditions. Our study suggests that either MCL AB or MCL PB can prevent anterior instability of the elbow joint during passive flexion. However, the MCL AB has a somewhat bigger influence on joint kinematics and contact characteristics compare to the MCL PB. This concurs with the often used and successful practice of reconstructing only the anterior bundle of the MCL for MCL injuries (Andrews, Jelsma, Joyce, & Timmerman; Fleisig et al., 2015). Sectioning both of the bundles together induced significant joint disruption. Detailed knowledge of the effects of MCL complex deficiency can be of great importance to orthopaedic surgeons planning surgical approaches to the medial aspect of the elbow for ligament or fracture repairs. It could also be immensely useful for post-operative rehabilitation protocols.

CHAPTER 6

MUSCLE DRIVEN ELBOW JOINT SIMULATION: A COMPUTATIONAL APPROACH

6.1 Introduction

As the most important joint of upper extremity, the elbow joint serves as a fulcrum of the forearm lever that greatly enhances the spatial positioning of the hand. Because of the centrality of the elbow joint to the upper extremity system, loss or diminished function of the elbow joint results significant deficits in upper extremity function and individual independence. Therefore, biomechanical analysis of the elbow joint is extremely important in reducing elbow injury, and for better execution of trauma management and prosthetic design.

A dynamic computational elbow joint model capable of concurrent prediction of muscle and ligament forces, along with cartilage contact mechanics would be an immensely useful tool in clinical practice. It can enhance our understanding of the interrelationships between joint structures and the musculature facilitating the development of patient specific surgical and no-surgical therapeutic strategies. In addition to providing better biomechanical knowledge of tissue function, a model can be used to provide subject specific intervention strategies aimed at modifying upper extremity movement for targeted outcomes, such as reducing articular cartilage stress. Furthermore, once the validated model is created, it can be used to analyze the biomechanical consequences of surgical reconstructive procedures and can be used for patient-specific preoperative planning, or rehabilitation. In this way, it can mitigate the need for large sample sizes in clinical trials, and can work at a fraction of the cost of cadaveric models.

Computational models of the upper extremity have been employed to study the joint biomechanical behavior and analyze musculoskeletal movement simulations (Fisk & Wayne, 2009; Garner & Pandy, 2001; Gonzalez et al., 1996; Holzbaur et al., 2005; Willing et al., 2013). Garner and Pandy (2001) developed a musculoskeletal upper extremity model to estimate the muscle moment arms and architectural properties such as muscle volume, physiological cross-sectional area, fiber length, pennation angle, and tendon rest length. Holzbaur et al. (2005) developed a three-dimensional model of the upper extremity that comprises all the major muscles of the upper limb, simulate musculoskeletal surgery, and analyze neuromuscular control. However, these models have limited clinical applicability due to idealizing the joint motion (e.g. hinge joint) rather than true anatomical joint constrained by ligament forces and cartilage contacts. In some circumstance such simplification would be helpful, however the human elbow joint has significant laxity that should not be ignored (Benham et al., 2001; Tanaka et al., 1998). The need for dynamic computational models that link muscle forces, motion, and joint contacts characteristics has long been recognized (Chao, 2003; Elias, Wilson, Adamson, & Cosgarea, 2004; Piazza & Delp, 2001). To our knowledge, forward-dynamic movement simulation of upper extremity that combines muscles, ligaments, and contact mechanics of the elbow geometries does not exist in recent literature.

Presented here is a method of developing a multibody elbow joint model within a forward dynamics simulation of elbow flexion-extension. The joint was constrained by multiple ligament bundles and three-dimensional deformable contacts. Moreover, the model includes the natural oblique wrapping of ligaments. Detailed contact force and contact area predictions were achieved by discretizing the humerus cartilage into multiple hexahedral elements. The model was verified by comparing the bone kinematics of a muscle driven forward dynamics with the motion driven inverse kinematics. The muscle activation patterns were also compared to experimental data. This verification lends credibility to the time-varying muscle force predictions and the recruitment of muscles that contribute to elbow flexion-extension.

6.2 Methods

6.2.1 Experimental measures

One healthy volunteer with no history of upper extremity problems was recruited for the project after providing a written informed consent approved by the institution's human subject review board. Two localizers made of ABS plastic were attached to the subject's upper arm and the forearm that included two orthogonal tubes (Fig. 6.1a). The tubes were filled with fluid (mustard) that appeared in the MR images. The localizers along with the tubes were used to register the coordinate system of the bone, cartilage, ligament, and muscle geometries later in the modeling process. High resolution MR images (Siemens 1.5T machine, TR: 14.8, TE: 6.18, slice thickness 0.5mm, imaging frequency 63.63 Hz, and group lengths 178) were acquired on the subject's dominant upper extremity. The localizers were not removed as the subject travelled to the UMKC Human Motion Lab. Two Optotrack motion capture rigid bodies (Northern Digital Inc, Waterloo, Ontario, Canada) were attached to the subject's upper arm and two rigid bodies were attached to the subject’s lower arm to collect the motion data. Each rigid body contains three infrared markers to capture 6 degrees of freedom of body segment. Then, the subject was positioned on a Biodex Multi-Joint Dynamometer system (Biodex Medical Systems, Shirley, NY) where the dominant arm was kept in a supinated rest position. The initial position and orientation of the arm were determined by recording coordinate of multiple points on the localizers, on the bony landmarks, and along the surface of the arm by using an Optotrak probe tool (Fig. 1b).

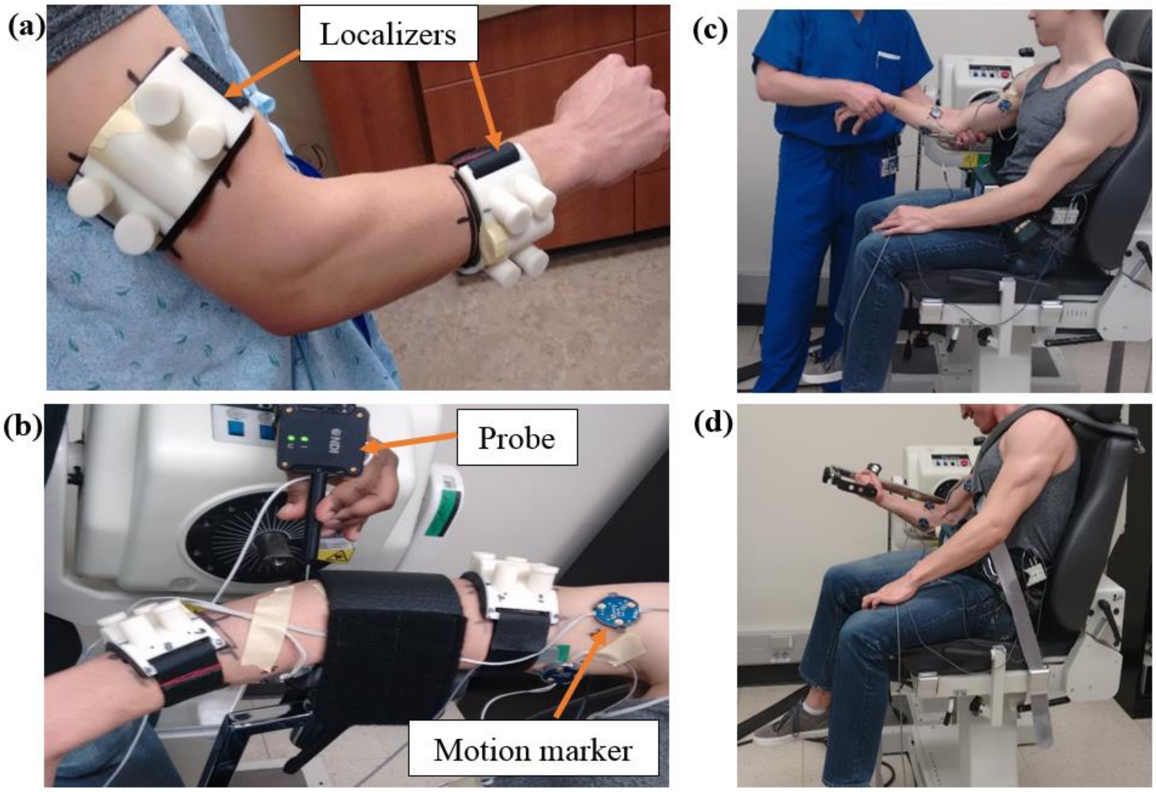

Figure 6.1. Experimental measurement. (a) Two plastic localizers attached to subject upper and lower arm. (b) Initial position collection using Optotrak probe. (c) The experimenter manipulating the arm for laxity test. (d) The subject performing experimental trail.

After that, the localizers were removed and an Orthopaedic surgeon performed a standard laxity test of the elbow. This test involves moving the elbow joint through its full range of motion by applying minimal force in the joint while motion data from the body segments is collected (Fig. 6.1c). This establishes the kinematic envelope of motion (KEM) from where the ligament zero-load lengths are extracted. Dynamic testing of the elbow was performed in the dynamometer (Fig. 6.1d). Along with the Optotrack markers the subject was also outfitted with two surface electromyography (EMG) sensors (Delsys Myomonitor IV wireless EMG system) on the biceps and triceps muscles to record muscle activity. First an isometric elbow flexion at maximum voluntary contraction (MVC) was performed to collect MVC EMG data. Then, the subject performed three seated elbow flexion/extension trials in three different protocols: 1) isokinetic at 10 deg/sec, 2) isokinetic at 60 deg/sec, and 3) at self-selected angular velocity (as fast as possible by the subject). For each trial, arm segment motion and EMG voltage were recorded.

6.3.2 Computational model

Three-dimensional bone and cartilage geometries were generated from the MR images using 3D Slicer (www.slicer.org). The geometries were then imported to MeshLab for post processing that included removing the spikes, reducing the noise, and smoothing the meshes (Cignoni et al., 2008). Finally, the multibody model was created in ADAMS (MSC Software Corporation, Santa Ana, CA) by aligning these geometries using the initial position and orientation obtained during experimental study (Fig. 6.2a). The applied material density of the bones and cartilages were 1600 kg/m^3 (Donahue et al., 2002) and 1000 kg/m^3 (Zielinska & Donahue, 2006) respectively.

The ligaments and membrane were modeled by different number of bundles based on their structure and function. The model included three bundles for the medial collateral ligament (MCL) anterior part, three bundles for the MCL posterior part, three bundles for the lateral ulnar collateral ligament (LUCL) (Rahman, Cil, Bogener, et al., 2016), three bundles for the radial collateral ligament (RCL) (Fisk & Wayne, 2009), and two bundles for the annular ligament (Fig. 6.2b-6.2c). The ligaments were attached to the bone, according to the attachment sites identified in the MRI and published literature studies (Fisk & Wayne, 2009; Miyake et al., 2012; Morrey, 2000; Morrey & An, 1985). Each ligament bundle was modeled as a tension only non-linear spring using a piecewise function that includes the "toe" region (Blankevoort & Huiskes, 1991; Wismans et al., 1980). The force-length relationship for each ligament bundle were described by equations (6-1) and (6-2):

$$f = \begin{cases} \frac{1}{4} k\, \varepsilon^2 / \varepsilon_l & 0 \le \varepsilon \le 2\varepsilon_l \\ k(\varepsilon - \varepsilon_l) & \varepsilon > 2\varepsilon_l \\ 0 & \varepsilon < 0 \end{cases} \qquad 6\text{-}1$$

$$\varepsilon = \left(\frac{l - l_0}{l_0} \right) \qquad 6\text{-}2$$

where, k is the stiffness parameter, ε_l is a spring parameter assumed to be 0.03 (Li et al., 1999), l is the length of the each bundle, and l_0 is the zero-load length (Blankevoort et al., 1991; Wismans et al., 1980). The ligament stiffness parameters were obtained from the literature (Fisk & Wayne, 2009; Regan et al., 1991), and the zero-load length was calculated from the laxity test. The zero load length for each ligament bundle was determined by taking the maximum distance measurement between ligament insertion and origin sites throughout the motion range and then multiplying by a correction factor (80% of max. length). This correction factor reduces the error unintentionally introduced by the experimenter by applying small amount of ligament force. Each ligament bundle also included a damping coefficient of 0.5 Ns/mm to remove the possibility of high frequency vibration during simulation (Guess, 2012). The ligaments were wrapped around the bone to represent their anatomical physiology, and to prevent the penetration of the ligament into the bone (Rahman, Cil, & Stylianou, 2016).

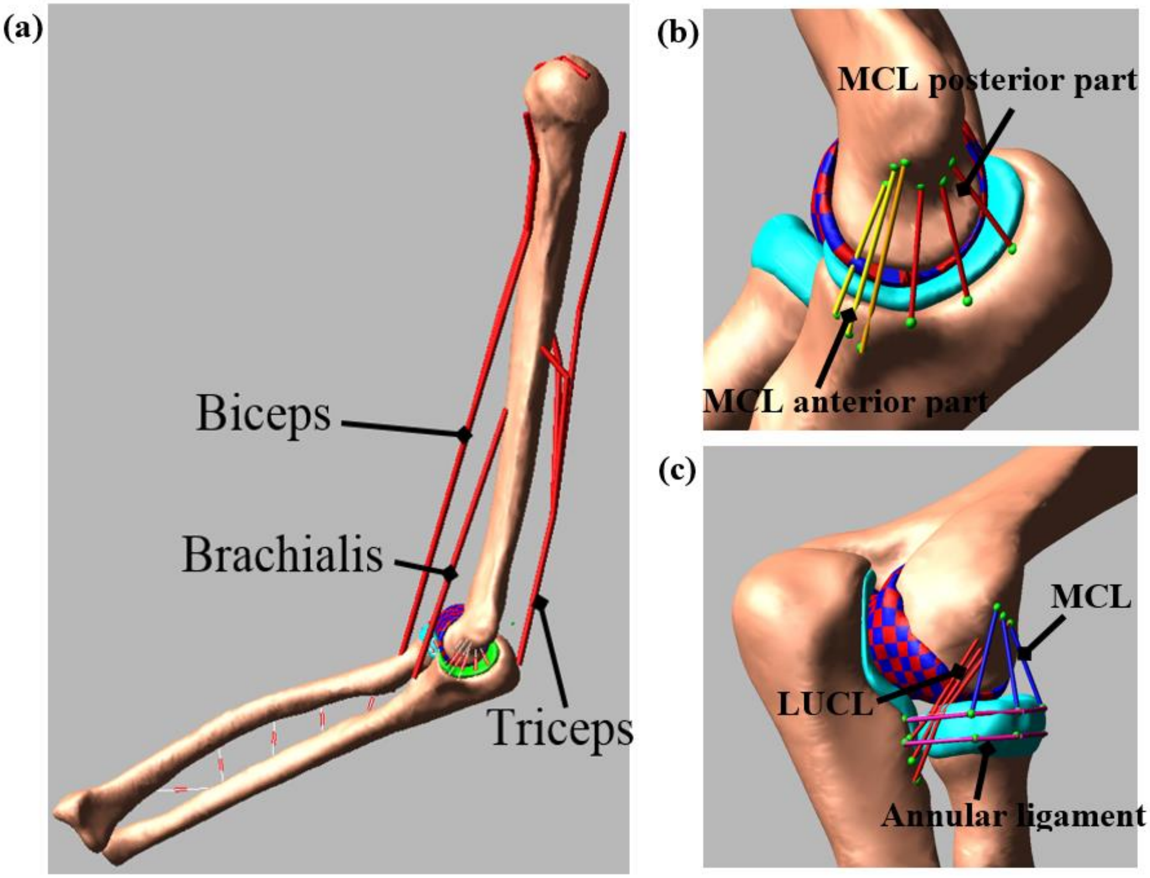

Figure 6.2. Multibody Model. (a) Subject specific model representing bones and major muscles crossing the elbow joint. (b) Medial collateral ligament complex, and (c) lateral collateral ligament complex in the model.

A custom macro was written in ADAMS to automatically divide the humerus cartilage into discrete hexahedral elements. Each element had an approximate 3 x 3 mm cross-sectional area (Fig. 6.3a). The macro connected each cartilage element to the humerus bone with a fixed joint located at the center of each element. The radial and ulnar cartilages were attached rigidly to the proximal surfaces of the respective bone. The macro also defined a deformable contact constraint with no friction using ADAMS compliant contact model (Eq. 6-3) between each humerus cartilage element with the radius and ulna cartilage geometry.

$$F_c = k_c\delta^n + B_c(\delta)\dot{\delta} \qquad \text{6-3}$$

where k_c is the contact stiffness, δ is the interpenetration of the geometries, and $B_c(\delta)$ is a damping coefficient. The damping coefficient was modeled as a function of penetration to prevent the discontinuities in the solution when two rigid bodies first came in contact (Hunt & Crossley, 1975). An optimization and design of experiment approach was used to determine the contact parameters and the size of discretized cartilage elements from another cadaver study. The optimization was done in such a way so that the maximum contact pressure and contact area errors were minimized between a multibody model and an identically loaded finite element model (Fig. 6.3b).

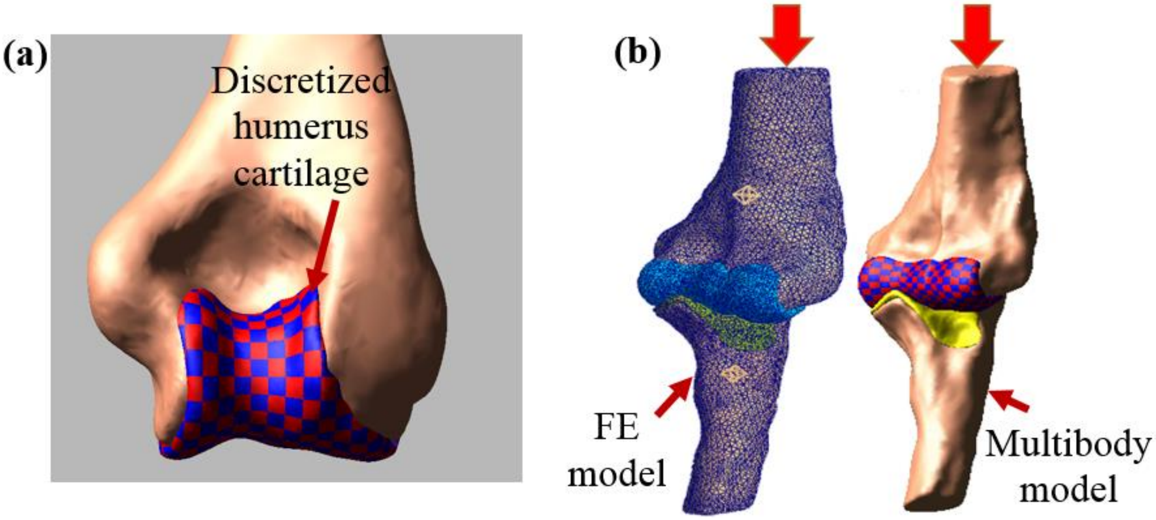

Figure 6.3. (a) Discretized humerus cartilage, and (b) optimization of the multibody model cartilage parameters by using identically loaded finite element model.

The model included three major muscles that cross elbow joint: triceps (long, lateral, and medial), biceps (long, short), and brachialis. Muscle parameters, insertions, origins, and via-points were obtained from the literature (Holzbaur et al., 2005). Point-to-point length measurements were created from origin to insertion through all via points to record the total length for each muscle. Then, the force elements were added for all muscles between origins to insertions through all via points. During inverse kinematics simulation, all muscle force magnitudes were set to zero. For the forward dynamics, the muscle force was computed using a feedback controller that used the inverse kinematics muscle length as a target to generate the forces.

Simulation of the computational model was done in two phases. First, the measured segment kinematics were used to move the model as constrained by the joint contacts and ligaments. The shortening/lengthening pattern of each muscle element was recorded during this step. Next the kinematic constraints were removed and muscles served as actuators to replicate the motions during forward dynamics. The muscle forces were calculated via feedback controllers implemented in Simulink (The MathWorks, Inc., Natick, MA). During forward dynamics simulation, ADAMS and Simulink were linked in co-simulation. In the process, ADAMS sent the current muscle lengths to Simulink and then Simulink sent muscle forces to ADAMS for the next calculation step. The error signal between the current forward dynamics muscle length and the muscle length measured during the inverse kinematics simulation was fed into a proportional–integral-derivative (PID) feedback controller. The output of the PID controller were the muscle forces required to track the inverse kinematics muscle lengths during the forward dynamic simulation. The muscle force was limited such that it can only pull, but not push. In addition, the PID parameters for each individual muscle were scaled based on the following equation:

$$\mathrm{P^i} = \frac{\mathrm{PCSA^i}}{\mathrm{Reference\ PCSA}} * \mathrm{Global\ P} \quad \mathrm{i} = 1{,}2 \ldots .\ \#\mathrm{of\ muscles} \tag{6-4}$$

where P^i is the proportional gain for muscle i. The $PCSA^i$ is the physiological cross-sectional area of each muscle and originate from the work by Holzbaur et al (Holzbaur et al., 2005). The Reference PCSA=487 mm^2, was calculated as the average of all muscles. Similar equations were applied for the integral and derivative gains. The global PID values for the muscle controller were: P= 50, I= 5, D=0.0005 (Guess, Stylianou, & Kia, 2014). Muscles with a PCSA less than the reference PCSA will have smaller PID gains while larger muscles will have larger PID gains. Furthermore, the force generated by an individual muscle is limited by its maximum force generating potential given by the following equation (Kia, Stylianou, & Guess, 2014):

$$F_{i-max} = PCSA_i \times \sigma_{max} \qquad 6\text{-}5$$

where F_{i-max} is the muscle maximum force, and σ_{max} = 1.4 N/mm^2 is the maximum tissue stress.

Local coordinate systems for the each bone segments were created as described by Ferreira, King [6], and Morrey and Chao [7] to measure the ulna and radius motions relative to the humerus coordinate system. The translations were represented in medial–lateral (M–L), anterior–posterior (A–P), and superior-inferior (S-I) directions and the rotations were represented as flexion- extension (F-E), varus-valgus (VR-VL), and internal-external (I-E) rotation (Rahman, Cil, Bogener, et al., 2016; Rahman, Cil, & Stylianou, 2016).The forward dynamic model was evaluated by comparing the model predicted kinematics to the experimental measurements. The predicted muscle activation patterns were also compared to the experimental EMG measurements. The experimental EMG signals were demeaned, rectified and then low-pass filtered to eliminate measurement noise using a second order Butterworth low-pass filter with a cutoff frequency of 6 Hz. Then, the filtered EMG signals were normalized to the maximum value of the specific trial for each muscle. To compare the kinematics between model and experiments, we calculated the root mean square (RMS) error using the following equation:

$$RMS = \sqrt{\frac{\sum_{i=1}^{n}(m_i - e_i)^2}{n}} \qquad 6\text{-}6$$

where *m* is the model value and *e* is the experimental value at each time point *i*, and *n* is the number of time points. We also computed the correlation coefficient between the model and experimental kinematics to increase the credibility of the evaluation. After model evaluation, joint contact locations, contact area, and pressures were predicted from the muscle driven forward dynamic simulation.

6.3 Results

Kinematic comparison between experiment and model prediction were presented in each anatomical direction for ulna and radius relative to humerus (Fig. 6.4-6.6). Both forearm bones rotated more internally in the model prediction than the experiment, and the difference was more pronounced at slower speeds of flexion-extension. The model also predicted slight greater valgus rotation of the forearm than the experimental measurement. Furthermore, both ulna and radius translated less laterally in the forward dynamics model prediction than the experiment with the difference being greater for slower speed. Overall, the models were in agreement with the experiment for each condition such as 10 deg/s, 60 deg/s and free velocity.

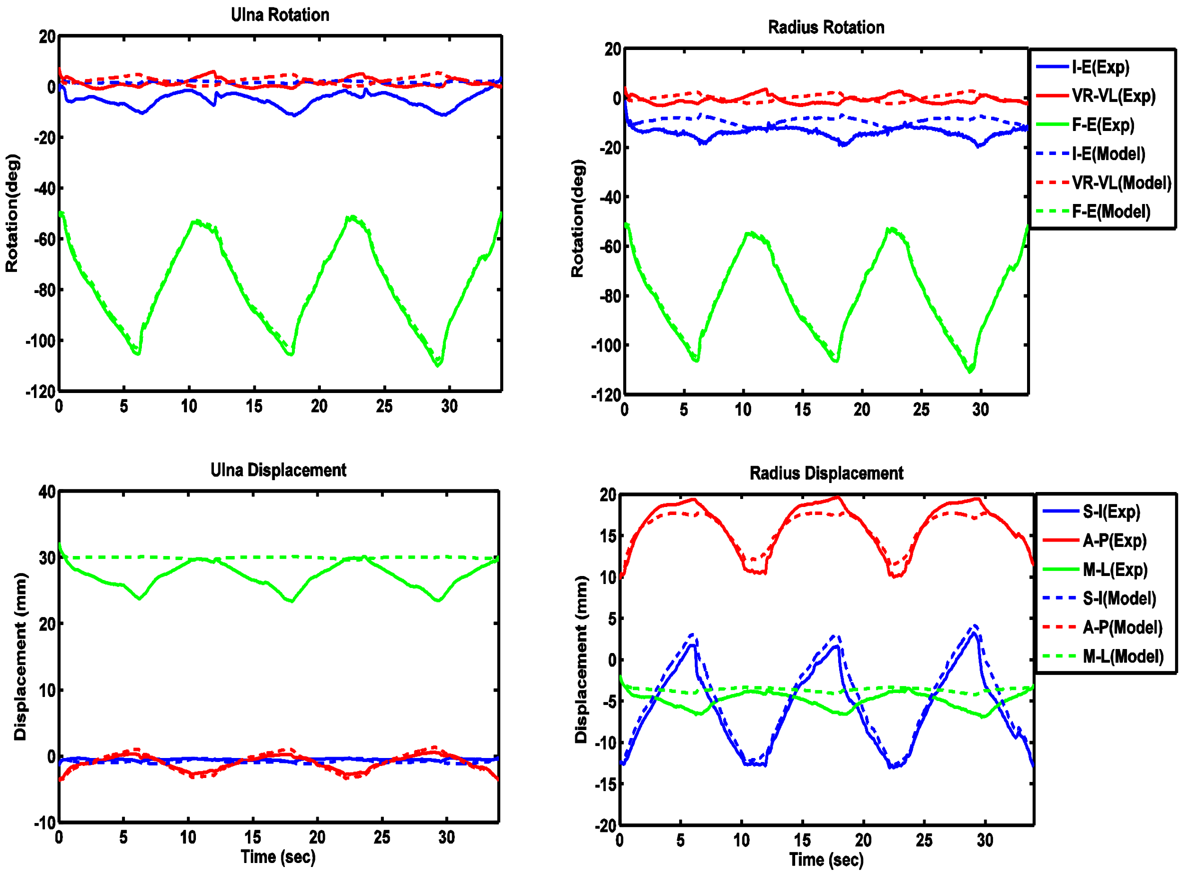

Figure 6.4. Comparison of bone kinematics between experiment and model prediction for 10 deg/s trial. Increasing trend of the graph indicates more internal rotation for I-E, more valgus rotation for VR-VL, more extension for F-E. Similarly, it indicates more superior translation for S-I, more anterior translation for A-P, and more medial translation for M-L. Decreasing trend of the graph indicates the opposite.

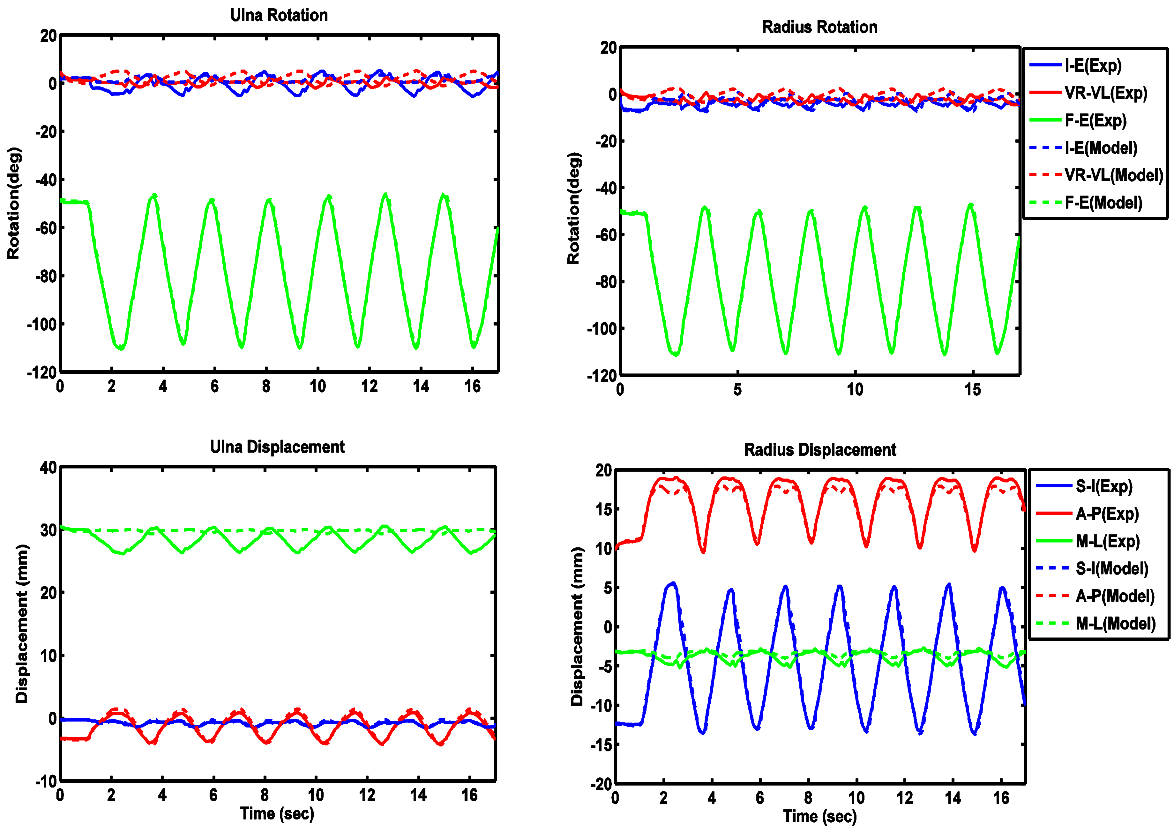

Figure 6.5. Comparison of bone kinematics between experiment and model prediction for 60 deg/s trial. Increasing trend of the graph indicates more internal rotation for I-E, more valgus rotation for VR-VL, more extension for F-E. Similarly, it indicates more superior translation for S-I, more anterior translation for A-P, and more medial translation for M-L. Decreasing trend of the graph indicates the opposite.

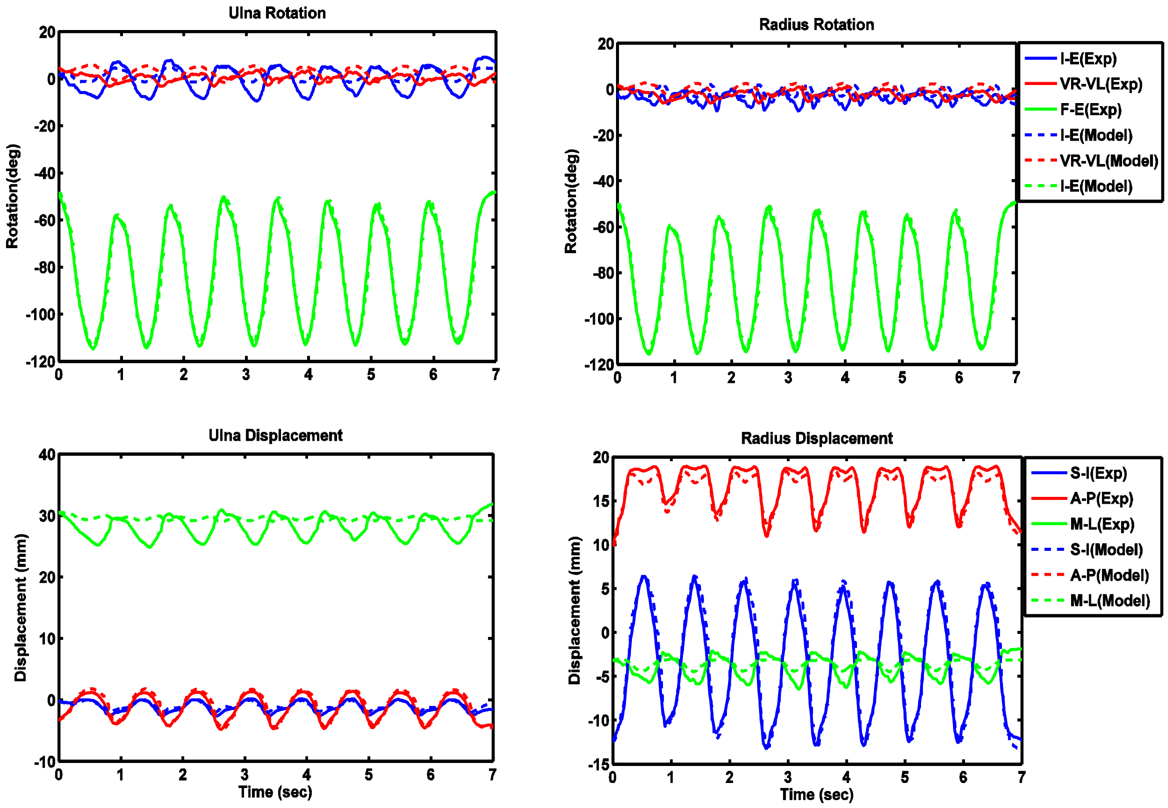

Figure 6.6. Relative bone kinematics for experiment and model prediction for free velocity trial. Increasing trend of the graph indicates more internal rotation for I-E, more valgus rotation for VR-VL, more extension for F-E. Similarly, it indicates more superior translation for S-I, more anterior translation for A-P, and more medial translation for M-L. Decreasing trend of the graph indicates the opposite.

The maximum RMS error was less than 8° for all the rotations of radius and ulna in all velocity conditions (Table 6.1). The maximum translational RMS error was less than 4mm for all condition and observed in medial-lateral direction. Overall, the RMS errors were higher at lower speed of flexion-extension than higher speed. Eight out of 12 kinematics had good correlation between model and experiment. Three kinematics for varus-valgus rotation and medial-lateral translation had less correlation and showed higher RMS error.

Table 6.1. RMS error (deg, mm) and correlation coefficients for ulna and radius kinematics.

Kinematics description	**10 deg/sec**		**60 deg/sec**		**Free motion**	
	RMS error	Correlation coefficient	RMS error	Correlation coefficient	RMS error	Correlation coefficient
Ulna internal-external rotation	7.4	0.48	2.9	0.86	4.0	0.92
Ulna varus-valgus rotation	2.8	-0.63	2.9	-0.13	2.7	0.57
Ulna flexion-extension rotation	1.3	0.99	1.2	0.99	2.7	0.99
Radius internal-external rotation	5.5	0.44	2.3	0.55	3.6	0.08
Radius varus-valgus rotation	2.6	-0.60	2.8	-0.15	2.6	0.61
Radius flexion-extension rotation	1.1	0.99	1.1	0.99	2.7	0.99
Ulna superior-inferior displacement	0.4	0.07	0.2	0.90	0.4	0.97
Ulna anterior-posterior displacement	0.4	0.98	0.4	0.99	0.6	0.98
Ulna medial-lateral displacement	3.4	-0.45	2.0	-0.62	2.3	-0.14
Radius superior-inferior displacement	1.3	0.99	0.6	0.99	1.3	0.99
Radius anterior-posterior displacement	1.0	0.98	0.8	0.99	0.8	0.97
Radius medial-lateral displacement	1.5	0.86	0.6	0.91	0.9	0.91

In general, the timing of predicted muscle forces followed the experimental muscle excitation pattern measured from the EMG for all velocity conditions (Fig. 6.7). Total number of muscle activations were consistent between the model and experimental measurement for all forearm velocity conditions. The normalized peak forces were also in agreement between model and experiment. However, model predicted maximum muscle forces reached their peaks faster which means the slopes were higher for model prediction than the experimental measurement.

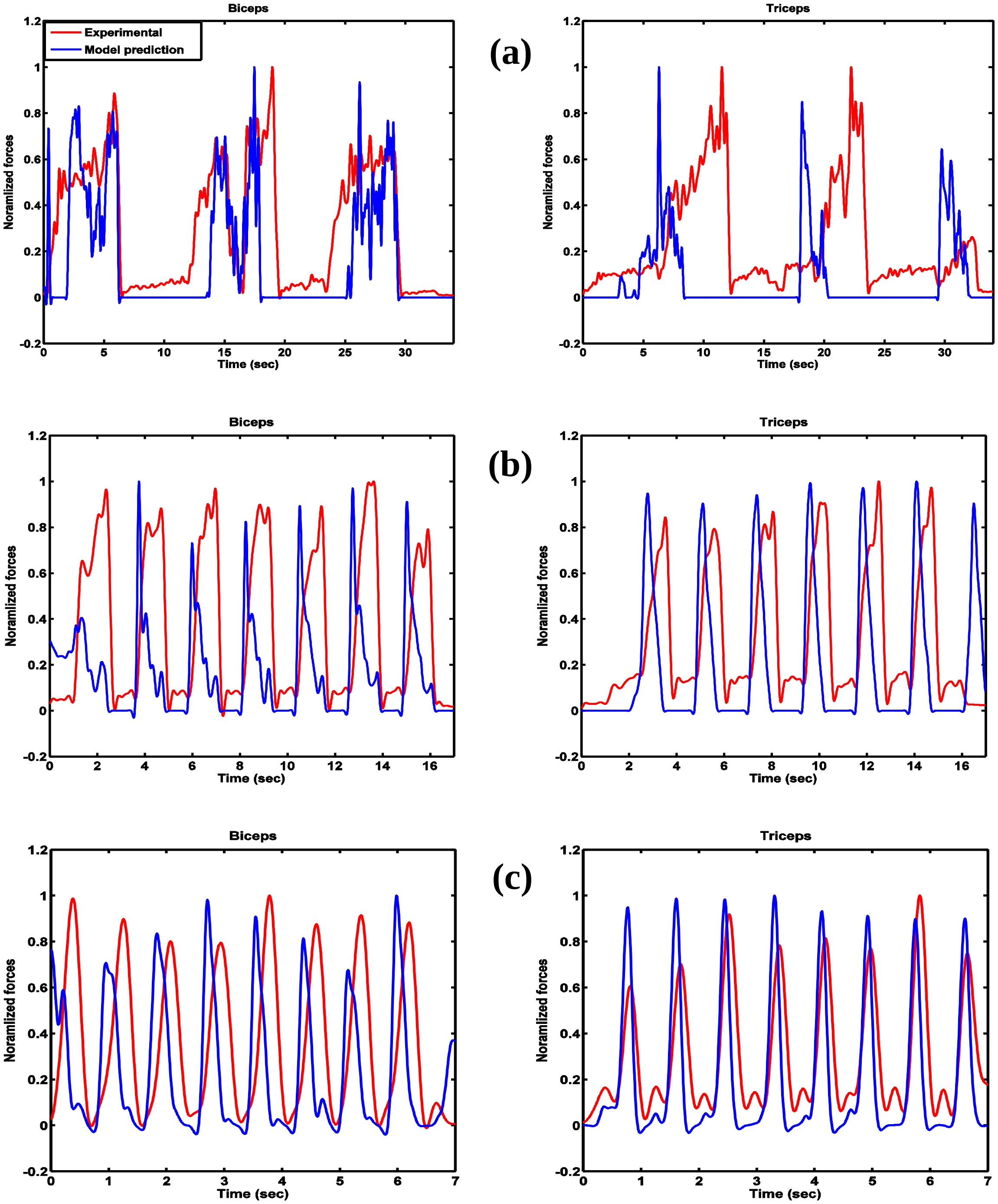

Figure 6.7. Normalized experimental EMG and normalized muscle forces from model prediction. 10 deg/s (a), 60 deg/s (b), and free velocity (c). Muscle forces are normalized to the maximum force produced by each muscle for the specific trial.

Contact pressure distributions on humeral cartilage were considerably different for various velocity conditions (Fig. 6.8). Both contact area and contact pressure were noticeably increased with increasing velocity. Peak contact pressure (on medial cartilage) was 3.7 MPa for 10deg/sec, 4.2 MPa for 60 deg/sec, and 5.5 MPa for free velocity. As expected, contact areas were much higher for the ulnohumeral joint than the radiohumeral joint.

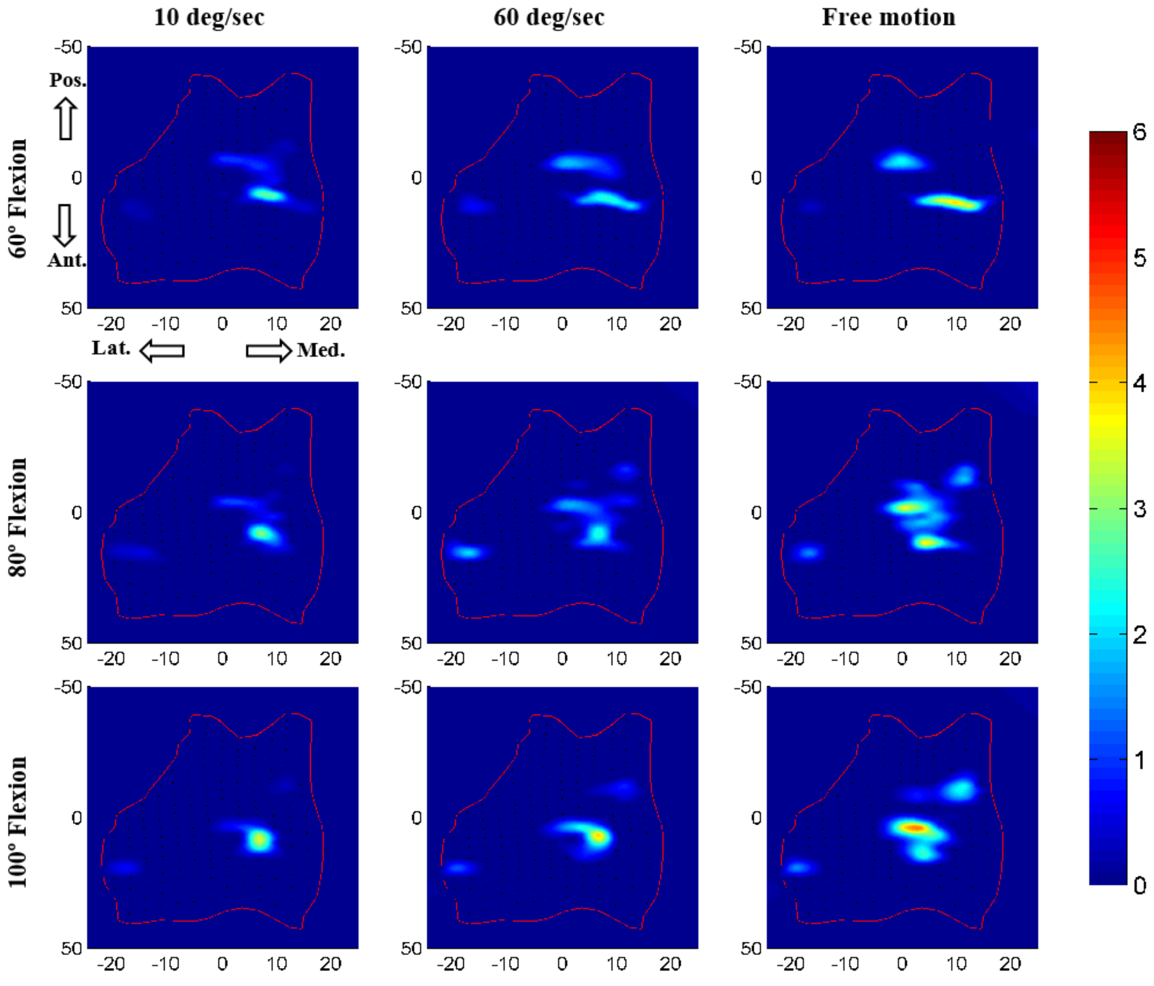

Figure 6.8. Contact pressure distribution on humeral cartilage for muscle driven forward dynamic simulation

6.4 Discussion

Concurrent prediction of muscle forces, joint kinematics, and cartilage contact mechanics from an anatomical model has the potential to be a powerful tool in Orthopaedics. This study developed an anatomical subject specific musculoskeletal model of the elbow joint in the multibody framework. The model also included discretized humerus cartilage that allowed computation of contact pressure distribution and location of contact areas. An optimization and design of experiment approach was used to determine the contact parameters and the size of discretized cartilage elements from a cadaver study. The model was evaluated by comparing the bone kinematics of a muscle driven forward dynamics to the experimental motion captured kinematics. The normalized muscle forces were also compared to experimental data. The developed musculoskeletal model is capable of predicting muscle and ligament forces, along with cartilage contact mechanics during dynamic activities. The model is computationally efficient for body level dynamic simulation and included multiple bones, joints, and tissues within muscle driven forward dynamics simulations.

Previously, computational musculoskeletal models had been employed to predict the muscle activation and upper limb strength estimation by constraining the elbow joint as a single one degree of freedom mechanical joint (Carmichael & Liu, 2015; Gonzalez, Abraham, Barr, & Buchanan, 1999; Gonzalez, Andritsos, Barr, & Abraham, 1993). This assumption removes the influence of contact forces on muscle forces and muscle contributions to motion beyond the sagittal plane. Because of the interdependency between articular contact and muscle forces, those forces need to be computed concurrently.

Furthermore, the three-dimensional measurement of simulated active elbow motion by an electromagnetic tracking device revealed that the amount of potential varus-valgus laxity that occurs during elbow flexion to average about 3 to 4 degrees (Tanaka et al., 1998). Ignoring this laxity by placing a mechanical joint can also affect the muscle force measurement. Omission of this normal laxity in implant designs is also the reason behind the failure of fully constraint elbow replacement implants. It increases the stress transfer to the implant-cement-bone interfaces and results in aseptic loosening (O'Driscoll, An, et al., 1992). Therefore, an accurate elbow model should reflect the intrinsic laxity of the elbow especially for clinical applications. In this study, the elbow joint was constrained by ligaments and, ulnohumeral, radiohumeral, and radioulnar contact forces allowing a total of 18 degrees-of-freedom.

The majority of the forward muscle driven kinematics showed good agreement with the experimental measurements. However, some of the forward dynamic predicted motions deviated from the recorded kinematics, especially the varus-valgus directions (Table 6.1). Not including the joint capsule in our model may be one of the contributing factors to this error. Morrey and An (1983) reported that the anterior and posterior capsule provided 32% varus and 33% valgus elbow stability respectively. Incorporating the joint capsule may reduce the error for internal-external rotation as well by providing the constrained in anterior and posterior direction. Furthermore, adding more muscle around the joint may also improve the overall kinematics, especially in varus-valgus angulation. In addition, because of the large range of flexion-extension, the Optotrak cameras could lose sight of the ired markers and caused some motion data loss, which can be another contributing factor to the errors. Therefore, including the joint capsule and better motion data collection are recommended for future studies to determine the joint kinematics with more confidence.

The activation patterns of the each contributing major muscles were correctly identified for all velocity conditions and favorably compared with experimental EMG measurement (Fig. 6.7). However, the normalized muscle forces were directly compared with the measured EMG, but EMG is not the force produced by the muscle but the measure of muscle activation. However, the joint kinematics computed in muscle driven forward dynamics simulation replicated the experimental joint motion which give confidence to our muscle force prediction. The little deviation of the muscle activation pattern may be the indicative of inaccurate measurement of EMG voltage due to surface EMG crosstalk. During experiment, it was hard to isolate the specific muscle group from other muscle which might induce some cross signal in EMG measurement.

Our predicted joint contact pressure increased by increasing the arm flexion-extension velocity. This appears reasonable since at higher velocity the muscle forces and the intensity of muscle activation increased which would lead to higher compression at the joint and increase the contact pressure. Since experimental joint contact pressure measurement from a live subject is not feasible, we could not compare our prediction with the experiment. However, our external prediction of joint kinematics and muscle activation replicate the experiment which gives confidence to our internal joint contact pressure prediction. Furthermore, our predicted ulnohumeral contact and non-contact areas were consistent with the contact patterns reported by Eckstein et al. (1995) and the maximum contact pressures were close in range (0.5 - 5Mpa) to the values reported by Brand (2005). The little over estimation of the pressure may be explained by how the ligament zero-load lengths were estimated. The correction factor used in our study was constant which may not be ideal for all ligament bundles (Bloemker et al., 2012) and may introduce some ligament tightness. More thorough study is needed to find the appropriate correction factor for each ligament bundle.

A potential limitation of the present model was that it was developed based on single subject experiment and therefore characteristic of a single elbow. Larger sample size is required to generalize the conclusions and for clinical applications. However, the modeling techniques and scheme were successfully applied by the research team for 5 cadaver studies (Rahman et al., 2014; Rahman, Cil, & Stylianou, 2016). The muscle modeling scheme was limited by not including the muscle force-length and force-velocity relationship and only using a feedback controller to compute muscle forces during the forward dynamics simulation. A potential problem of using the feedback controller is that it cannot correctly predict the muscle forces from antagonistic muscles since there can be muscle force production without significant change in muscle length. Hybrid control methods where some EMG signals are used as input to the model may solve this issue. As demonstrated previously, *in vivo* joint contact force estimation is highly dependent on correct prediction of muscle forces. Muscle force calculations depend on resolving the muscle redundancy problem. This problem occurs because the muscle forces necessary to produce a certain motion are not unique. Some additional optimization of muscle forces would be required to solve these issues.

In conclusion, the detailed dynamics model and methodology presented in this study provides a versatile tool in studying elbow joint kinematics, musculature, and contact characteristics. The model includes the true anatomical constrained joint instead of an idealized mechanical joint and allowed computation of contact pressure distribution instead of single point contact. The model accuracy was evaluated by the experimental measurement obtained from kinematics and muscle activation. The model in this study allows concurrent prediction of muscle and ligament forces along with cartilage contact pressure. More detailed subject specific measurements and refinement of the musculature can further improve its accuracy and clinical applicability.

CHAPTER 7

CONCLUSION

This manuscript presents 4 separate studies involving computational modeling of the human elbow joint. The main advantages of the computer model is that it can predict what cannot be measured experimentally in a human body such as joint forces, ligament tension, and muscle forces. Furthermore, once the validated model is created, it can be used to analyze the biomechanical consequences of surgical reconstructive procedures, and can be used for patient-specific preoperative planning, or rehabilitation. It can mitigate the need for large sample sizes in clinical trials, and can work at a fraction of the cost of cadaveric models.

The first phase of the work was to develop the multibody model of the human elbow joint based on two separate cadaver specimens (Chapter 3). The developed model for this project included subject-specific bone and cartilage geometries derived from cadaver upper limb, representation of the non-linear ligament bundles crossing the elbow, and wrapping of ligaments around bones. The humerus cartilage was represented by discrete rigid bodies’ fixed to the humerus bone that interacted with the radius and ulna cartilages through deformable contacts. The contact parameters for the compliant contact law were derived using simplified elastic foundation contact theory. Finally, the model performances were evaluated by comparing the model predicted bone segment kinematics against experimental measurements.

The difference between experiment and model predictions were considerably low and gave confidence of the model validation. The maximum RMS error between the predicted and measured kinematics during the complete testing cycle was 2.7 mm medial-lateral translation and 9.7° varus–valgus rotation of radius relative to humerus (for elbow 2). After model validation, a lateral ulnar collateral ligament (LUCL) deficient condition was simulated and, contact pressures and kinematics were compared to the intact elbow model. A noticeable difference in kinematics, contact area, and contact pressure were observed for LUCL deficient condition. LUCL deficiency induced higher internal rotations for both the radius and ulna during flexion and an associated medial shift of the articular contact area.

To our knowledge this was the only study in which discretized cartilage geometries were used to predict contact pressure at the elbow joint in a dynamic simulation. The method was computationally efficient, and capable of predicting cartilage contact area, and contact pressure during dynamic conditions while recreating the kinematics of the bony segments accurately. The model presented in this study demonstrates the efficacy of using multibody models in studying elbow joint function and offers certain capabilities for future studies of elbow joint mechanics in dynamic conditions.

The second phase of this work was to use the previously validated model to observe the ligament deficiency on joint kinematics and contact characteristics. The main goals of the study presented in Chapter 4 were to investigate the effects of lateral collateral ligament deficiency on elbow kinematics, ligament loads, and articular contact pressure using an anatomically correct computational multibody elbow joint model. Four different conditions were simulated for this study (i) simulation with all ligaments intact (baseline)

(ii) simulation for RCL deficiency (iii) simulation for LUCL deficiency (iv) and simulation for combined RCL & LUCL deficiency.

One of the previously validated anatomically correct computational multibody model (61 yrs, male, right arm) was the basis of this study. The three-dimensional bone and cartilage geometries came from the CT and MR images. The elbow was placed initially at approximately 20° of flexion and a 345 mm vertical downward motion profile was applied over 40 seconds to the humerus head. The vertical displacement induced flexion from the initial position to a maximum flexion angle of 135°. The input motion profile was identical for all ligament condition. For each condition, relative bone kinematics, contact pressure, contact area, and intact ligament forces were predicted. We found that intact and isolated radial collateral ligament deficient elbow simulations were almost identical for all observed outcomes. Minor differences in kinematics, contact area and pressure were observed for the isolated lateral ulnar collateral ligament deficient elbow compared to the intact elbow, but no elbow dislocation was detected. However, sectioning both ligaments together induced substantial differences in kinematics, contact area and contact pressure, and caused complete dislocation of the elbow joint.

Detailed knowledge of the effects of lateral collateral ligament deficiency can be of great importance to orthopaedic surgeons planning surgical approaches to the elbow for ligament and fracture repairs or arthroplasty. Our results also concur with the literature with regards to the role of the LUCL in posterolateral rotatory instability since the LUCL has greater influence on the kinematics and contact pressures than the RCL. This current study is a first step in studying ligament deficiency in an anatomically correct computational model of the elbow joint. Anatomically correct computational models are widely used in knees but such models have been under-utilized in elbow studies. The advantages of the multibody modeling framework presented here outweigh its limitations. Ultimately, such models can be of great use in delivering objective, data-driven, patient-specific care.

The primary purpose of the study presented in Chapter 5 was to simulate medial collateral ligament deficiency in a computational, anatomically correct multibody elbow joint model. Four cases were simulated in this study: (i) keeping all ligament intact (‘Intact’ model) (ii) isolated MCL anterior bundle deficiency (MCL AB deficient) (iii) isolated MCL posterior bundle deficiency (MCL PB deficient) (iv) and combined MCL anterior and posterior bundle deficiency (Both MCL deficient). For each ligament deficiency condition, kinematics, contact area, contact pressure, and ligament forces were calculated and compared to the intact model simulation.

Two previously validated subject specific joint models were passively flexed by applying a vertical downward motion on the humeral head that induced the final joint flexion of about 135° for both specimens. The motion profile was identical for all simulations. We found the minimal differences of bone kinematics for isolated anterior and posterior bundle deficient elbow compared to intact elbow. However, sectioning the entire medial collateral ligament generated significant differences in all joint kinematics for both specimens and induced substantial elbow instability. The joint contact characteristics were nearly similar for intact and isolated posterior bundle deficiency. Minor differences were observed for the isolated anterior bundle deficiency and significant differences were detected for the entire medial collateral ligament deficient case. Complete elbow dislocations were not observed for any ligament deficient elbow.

The results of our study suggest that either MCL AB or MCL PB can prevent anterior instability of the elbow joint during passive flexion. However, the MCL AB has a somewhat bigger influence on joint kinematics and contact characteristics compare to the MCL PB. This concurs with the often used and successful practice of reconstructing only the anterior bundle of the MCL for MCL injuries. Sectioning both of the bundles together induced significant joint disruption. Detailed knowledge of the effects of MCL complex deficiency can be of great importance to orthopaedic surgeons planning surgical approaches to the medial aspect of the elbow for ligament or fracture repairs. It could also be immensely useful for post-operative rehabilitation protocols.

The final phase of this treatise was to apply the modeling technique, tools, and parameters acquired from the cadaver studies to a live subject study and obtain a musculoskeletal model of human elbow joint. Therefore, the primary goal of the study presented in Chapter 6 was to develop the musculoskeletal model of the human elbow joint based on live subject experimental measurements. One healthy volunteer with no history of upper extremity problems was recruited for the project after providing a written informed consent approved by the institution’s human subject review board. The three dimensional bone and cartilages geometries were obtained from the MR images of the subject. The joint was constrained by multiple ligament bundles and three-dimensional deformable contact. Moreover, the model included the natural oblique wrapping of ligaments. Detailed contact force and contact area predictions are achieved by discretizing the humerus cartilage into multiple hexahedral elements.

The model was verified by comparing the bone kinematics of a muscle driven forward dynamics with a motion driven inverse kinematics for three different velocity conditions of the forearm: 1) isokinetic at 10 deg/sec, 2) isokinetic at 60 deg/sec, and 3) at self-selected angular velocity (as fast as possible by the subject). The maximum RMS error was less than 8° for all the rotations of radius and ulna in all velocity conditions. The maximum translational RMS error was less than 4mm for all condition and observed in medial-lateral direction. Eight out of 12 kinematics had good correlation between model and experiment. The muscle activation patterns were also compared between model and experiment. The timing of predicted muscle forces followed the experimental muscle excitation pattern measured from EMG. The normalized peak forces also showed a good agreement. This verification lends credibility to the time-varying muscle force predictions and the recruitment of muscle that contribute to elbow flexion-extension. After getting confidence on validation, the joint contact area and pressure distribution were predicted from the forward dynamic simulation.

In conclusion, the detailed dynamics of the model and methodology presented in this study provided a versatile tool in studying elbow joint kinematics, musculatures, and contact characteristics. The model included the true anatomical constrained joint instead of an idealized mechanical joint and allowed computation of contact pressure distribution instead of single point contact. The model in this study provided the capability of concurrent prediction of muscle and ligament forces along with cartilage contact pressure.

It is extremely important to calculate the muscle and joint contact forces concurrently because of their interdependency. More detailed subject specific measurement and refinement of the musculature can further improve the model accuracy and its clinical applicability.

REFERENCES

Alcid, J. G., Ahmad, C. S., & Lee, T. Q. (2004). Elbow anatomy and structural biomechanics. *Clinics in Sports Medicine, 23*(4), 503-517, vii. doi: 10.1016/j.csm.2004.06.008

Alolabi, B., Gray, A., Ferreira, L. M., Johnson, J. A., Athwal, G. S., & King, G. J. (2012). Rehabilitation of the medial- and lateral collateral ligament-deficient elbow: an in vitro biomechanical study. *Journal of Hand Therapy, 25*(4), 363-372;. doi: 10.1016/j.jht.2012.06.001

Amis, A. A., Dowson, D., & Wright, V. (1979). Muscle strengths and musculoskeletal geometry of the upper limb. *Engineering in Medicine, 8*(1), 41-48.

Amis, A. A., Dowson, D., Wright, V., & Miller, J. H. (1979). The derivation of elbow joint forces, and their relation to prosthesis design. *Journal of Medical Engineering and Technology, 3*(5), 229-234.

An, K. N. (2005). Kinematics and constraint of total elbow arthroplasty. *Journal of Shoulder and Elbow Surgery, 14*(1 Suppl S), 168S-173S. doi: 10.1016/j.jse.2004.09.035

An, K. N., Hui, F. C., Morrey, B. F., Linscheid, R. L., & Chao, E. Y. (1981). Muscles across the elbow joint: a biomechanical analysis. *Journal of Biomechanics, 14*(10), 659-669.

Anderst, W. J., & Tashman, S. (2003). A method to estimate in vivo dynamic articular surface interaction. *Journal of Biomechanics, 36*(9), 1291-1299.

Andrews, J. R., Jelsma, R. D., Joyce, M. E., & Timmerman, L. A. Open surgical procedures for injuriesto the elbow in throwers. *Operative Techniques in Sports Medicine, 4*(2), 109-113. doi: 10.1016/S1060-1872(96)80056-6

Armstrong, A. D., Dunning, C. E., Faber, K. J., Duck, T. R., Johnson, J. A., & King, G. J. (2000). Rehabilitation of the medial collateral ligament-deficient elbow: an in vitro biomechanical study. *Journal of Hand Surgery, 25*(6), 1051-1057. doi: 10.1053/jhsu.2000.17819

Ateshian, G. A., Ark, J. W., Rosenwasser, M. P., Pawluk, R. J., Soslowsky, L. J., & Mow, V. C. (1995). Contact areas in the thumb carpometacarpal joint. *Journal of Orthopaedic Research, 13*(3), 450-458. doi: 10.1002/jor.1100130320

Athanasiou, K. A., Rosenwasser, M. P., Buckwalter, J. A., Malinin, T. I., & Mow, V. C. (1991). Interspecies comparisons of in situ intrinsic mechanical properties of distal femoral cartilage. *Journal of Orthopaedic Research, 9*(3), 330-340. doi: 10.1002/jor.1100090304

Bei, Y., & Fregly, B. J. (2004). Multibody dynamic simulation of knee contact mechanics. *Medical Engineering and Physics, 26*(9), 777-789. doi: 10.1016/j.medengphy.2004.07.004

Benham, M. P., Wright, D. K., & Bibb, R. (2001). Modelling soft tissue for kinematic analysis of multi-segment human body models. *Biomedical Sciences Instrumentation, 37*, 111-116.

Blankevoort, L., & Huiskes, R. (1991). Ligament-bone interaction in a three-dimensional model of the knee. *Journal of Biomechanical Engineering, 113*(3), 263-269.

Blankevoort, L., Kuiper, J. H., Huiskes, R., & Grootenboer, H. J. (1991). Articular contact in a three-dimensional model of the knee. *Journal of Biomechanics, 24*(11), 1019-1031.

Bloemker, K. H., Guess, T. M., Maletsky, L., & Dodd, K. (2012). Computational knee ligament modeling using experimentally determined zero-load lengths. *Open Biomed Eng J, 6*, 33-41. doi: 10.2174/1874230001206010033

Brand, R. A. (2005). Joint contact stress: a reasonable surrogate for biological processes? *Iowa Orthopaedic Journal, 25*, 82-94.

Brown, T. D., Rudert, M. J., & Grosland, N. M. (2004). New methods for assessing cartilage contact stress after articular fracture. *Clinical Orthopaedics and Related Research*(423), 52-58.

Carmichael, M. G., & Liu, D. (2015). Upper limb strength estimation of physically impaired persons using a musculoskeletal model: A sensitivity analysis. *Conference Proceedings of the Annual International Conference of the IEEE Engineering in Medicine and Biology Society, 2015*, 2438-2441. doi: 10.1109/embc.2015.7318886

Cavalheiro, C. S., Filho, M. R., Rozas, J., Wey, J., de Andrade, A. M., & Caetano, E. B. (2015). Anatomical study on the innervation of the elbow capsule. *Rev Bras Ortop, 50*(6), 673-679. doi: 10.1016/j.rboe.2015.10.001

Chao, E. Y. (2003). Graphic-based musculoskeletal model for biomechanical analyses and animation. *Medical Engineering and Physics, 25*(3), 201-212.

Charalambous, C. P., & Stanley, J. K. (2008). Posterolateral rotatory instability of the elbow. *Journal of Bone and Joint Surgery (British Volume), 90*(3), 272-279. doi: 10.1302/0301-620X.90B3.19868

Choi, Y. S., Lee, Y. H., Kim, S., Cho, H. W., Song, H. T., & Suh, J. S. (2013). Four-dimensional real-time cine images of wrist joint kinematics using dual source CT with minimal time increment scanning. *Yonsei Medical Journal, 54*(4), 1026-1032. doi: 10.3349/ymj.2013.54.4.1026

Chuang, L. L., Wu, C. Y., Lin, K. C., & Lur, S. Y. (2012). Quantitative mechanical properties of the relaxed biceps and triceps brachii muscles in patients with subacute stroke: a reliability study of the myoton-3 myometer. *Stroke Res Treat, 2012*, 617694. doi: 10.1155/2012/617694

Cignoni, P., Callieri, M., Corsini, M., Dellepiane, M., Ganovelli, F., & Ranzuglia, G. (2008). MeshLab: an Open-Source Mesh Processing Tool. *Sixth Eurographics Italian Chapter Conference*, 129-136.

Cohen, M. S., & Bruno, R. J. (2001). The collateral ligaments of the elbow: anatomy and clinical correlation. *Clinical Orthopaedics and Related Research*(383), 123-130.

Cohen, M. S., & Hastings, H., 2nd. (1997). Rotatory instability of the elbow. The anatomy and role of the lateral stabilizers. *Journal of Bone and Joint Surgery (American Volume), 79*(2), 225-233.

Cohen, Z. A., Henry, J. H., McCarthy, D. M., Mow, V. C., & Ateshian, G. A. (2003). Computer simulations of patellofemoral joint surgery. Patient-specific models for tuberosity transfer. *American Journal of Sports Medicine, 31*(1), 87-98.

Currier, D. P. (1972). Maximal isometric tension of the elbow extensors at varied positions. I. Assessment by cable tensiometer. *Physical Therapy, 52*(10), 1043-1049.

de Haan, J., Schep, N. W., Eygendaal, D., Kleinrensink, G. J., Tuinebreijer, W. E., & den Hartog, D. (2011). Stability of the elbow joint: relevant anatomy and clinical implications of in vitro biomechanical studies. *Open Orthopaedics Journal, 5*, 168-176. doi: 10.2174/1874325001105010168

Donahue, T. L., Hull, M. L., Rashid, M. M., & Jacobs, C. R. (2002). A finite element model of the human knee joint for the study of tibio-femoral contact. *Journal of Biomechanical Engineering, 124*(3), 273-280.

Dunning, C. E., Zarzour, Z. D., Patterson, S. D., Johnson, J. A., & King, G. J. (2001). Ligamentous stabilizers against posterolateral rotatory instability of the elbow. *Journal of Bone and Joint Surgery (American Volume), 83-A*(12), 1823-1828.

Eckstein, F., Hudelmaier, M., & Putz, R. (2006). The effects of exercise on human articular cartilage. *Journal of Anatomy, 208*(4), 491-512. doi: 10.1111/j.1469-7580.2006.00546.x

Eckstein, F., Merz, B., Muller-Gerbl, M., Holzknecht, N., Pleier, M., & Putz, R. (1995). Morphomechanics of the humero-ulnar joint: II. Concave incongruity determines the distribution of load and subchondral mineralization. *Anatomical Record, 243*(3), 327-335. doi: 10.1002/ar.1092430307

Elias, J. J., Wilson, D. R., Adamson, R., & Cosgarea, A. J. (2004). Evaluation of a computational model used to predict the patellofemoral contact pressure distribution. *Journal of Biomechanics, 37*(3), 295-302.

Ferreira, L. M. (2011). *Development of an Active Elbow Motion Simulator and Coordinate Systems to Evaluate Kinematics in Multiple Positions.* (University of Western Ontario - Electronic Thesis and Dissertation Repository). Retrieved from http://ir.lib.uwo.ca/etd/84

Ferreira, L. M., King, G. J., & Johnson, J. A. (2011). Motion-derived coordinate systems reduce inter-subject variability of elbow flexion kinematics. *Journal of Orthopaedic Research, 29*(4), 596-601. doi: 10.1002/jor.21278

Fisk, J. P. (2007). *Development and Validation of a Computational Musculoskeletal Model of the Elbow Joint.* Virginia Commonwealth University. Retrieved from http://books.google.com/books?id=z1CmtgAACAAJ

Fisk, J. P., & Wayne, J. S. (2009). Development and validation of a computational musculoskeletal model of the elbow and forearm. *Annals of Biomedical Engineering, 37*(4), 803-812. doi: 10.1007/s10439-009-9637-x

Fleisig, G. S., Leddon, C. E., Laughlin, W. A., Ciccotti, M. G., Mandelbaum, B. R., Aune, K. T., . . . Andrews, J. R. (2015). Biomechanical performance of baseball pitchers with a history of ulnar collateral ligament reconstruction. *American Journal of Sports Medicine, 43*(5), 1045-1050. doi: 10.1177/0363546515570464

Fuss, F. K. (1991). The ulnar collateral ligament of the human elbow joint. Anatomy, function and biomechanics. *Journal of Anatomy, 175*, 203-212.

Garner, B. A., & Pandy, M. G. (2001). Musculoskeletal model of the upper limb based on the visible human male dataset. *Comput Methods Biomech Biomed Engin, 4*(2), 93-126. doi: 10.1080/10255840008908000

Gonzalez, R. V., Abraham, L. D., Barr, R. E., & Buchanan, T. S. (1999). Muscle activity in rapid multi-degree-of-freedom elbow movements: solutions from a musculoskeletal model. *Biological Cybernetics, 80*(5), 357-367.

Gonzalez, R. V., Andritsos, M. J., Barr, R. E., & Abraham, L. D. (1993). Comparison of experimental and predicted muscle activation patterns in ballistic elbow joint movements. *Biomedical Sciences Instrumentation, 29*, 9-16.

Gonzalez, R. V., Hutchins, E. L., Barr, R. E., & Abraham, L. D. (1996). Development and evaluation of a musculoskeletal model of the elbow joint complex. *Journal of Biomechanical Engineering, 118*(1), 32-40.

Gordon, K. D., Kedgley, A. E., Ferreira, L. M., King, G. J., & Johnson, J. A. (2006). Design and implementation of an instrumented ulnar head prosthesis to measure loads in vitro. *Journal of Biomechanics, 39*(7), 1335-1341. doi: 10.1016/j.jbiomech.2005.03.002

Guess, T. M. (2012). Forward dynamics simulation using a natural knee with menisci in the multibody framework. *Multibody System Dynamics, 28*(1-2), 37-53. doi: 10.1007/s11044-011-9293-4

Guess, T. M., Liu, H., Bhashyam, S., & Thiagarajan, G. (2013). A multibody knee model with discrete cartilage prediction of tibio-femoral contact mechanics. *Comput Methods Biomech Biomed Engin, 16*(3), 256-270. doi: 10.1080/10255842.2011.617004

Guess, T. M., & Stylianou, A. (2012). Simulation of anterior cruciate ligament deficiency in a musculoskeletal model with anatomical knees. *Open Biomed Eng J, 6*, 23-32. doi: 10.2174/1874230001206010023

Guess, T. M., Stylianou, A. P., & Kia, M. (2014). Concurrent prediction of muscle and tibiofemoral contact forces during treadmill gait. *Journal of Biomechanical Engineering, 136*(2), 021032. doi: 10.1115/1.4026359

Guess, T. M., Thiagarajan, G., Kia, M., & Mishra, M. (2010). A subject specific multibody model of the knee with menisci. *Medical Engineering and Physics, 32*(5), 505-515. doi: 10.1016/j.medengphy.2010.02.020

Hannouche, D., & Begue, T. (1999). Functional anatomy of the lateral collateral ligament complex of the elbow. *Surgical and Radiologic Anatomy, 21*(3), 187-191.

Hildebrand, K. A., Patterson, S. D., & King, G. J. (1999). Acute elbow dislocations: simple and complex. *Orthopedic Clinics of North America, 30*(1), 63-79.

Holzbaur, K. R., Murray, W. M., & Delp, S. L. (2005). A model of the upper extremity for simulating musculoskeletal surgery and analyzing neuromuscular control. *Annals of Biomedical Engineering, 33*(6), 829-840.

Hotchkiss, R. N., An, K. N., Sowa, D. T., Basta, S., & Weiland, A. J. (1989). An anatomic and mechanical study of the interosseous membrane of the forearm: pathomechanics of proximal migration of the radius. *Journal of Hand Surgery, 14*(2 Pt 1), 256-261.

Hunt, K. H., & Crossley, F. R. E. (1975). Coefficient of Restitution Interpreted as Damping in Vibroimpact. *Journal of Applied Mechanics, 42*(2), 440. doi: 10.1115/1.3423596

Josefsson, P. O., Gentz, C. F., Johnell, O., & Wendeberg, B. (1987). Surgical versus non-surgical treatment of ligamentous injuries following dislocation of the elbow joint. A prospective randomized study. *Journal of Bone and Joint Surgery (American Volume), 69*(4), 605-608.

Kaiser, J., Bradford, R., Johnson, K., Wieben, O., & Thelen, D. G. (2013). Measurement of tibiofemoral kinematics using highly accelerated 3D radial sampling. *Magnetic Resonance in Medicine, 69*(5), 1310-1316. doi: 10.1002/mrm.24362

Kia, M., Stylianou, A. P., & Guess, T. M. (2014). Evaluation of a musculoskeletal model with prosthetic knee through six experimental gait trials. *Medical Engineering and Physics, 36*(3), 335-344. doi: 10.1016/j.medengphy.2013.12.007

King, G. J., Morrey, B. F., & An, K. N. (1993). Stabilizers of the elbow. *Journal of Shoulder and Elbow Surgery, 2*(3), 165-174. doi: 10.1016/s1058-2746(09)80053-0

Kuhn, M. A., & Ross, G. (2008). Acute elbow dislocations. *Orthopedic Clinics of North America, 39*(2), 155-161, v. doi: 10.1016/j.ocl.2007.12.004

Kura, H., Kitaoka, H. B., Luo, Z. P., & An, K. N. (1998). Measurement of surface contact area of the ankle joint. *Clinical Biomechanics (Bristol, Avon), 13*(4-5), 365-370.

Kwak, S. D., Blankevoort, L., & Ateshian, G. A. (2000). A Mathematical Formulation for 3D Quasi-Static Multibody Models of Diarthrodial Joints. *Comput Methods Biomech Biomed Engin, 3*(1), 41-64. doi: 10.1080/10255840008915253

Lalone, E. A., Giles, J. W., Alolabi, B., Peters, T. M., Johnson, J. A., & King, G. J. (2013). Utility of an image-based technique to detect changes in joint congruency following simulated joint injury and repair: an in vitro study of the elbow. *Journal of Biomechanics, 46*(4), 677-682. doi: 10.1016/j.jbiomech.2012.11.047

Lee, M. L., & Rosenwasser, M. P. (1999). Chronic elbow instability. *Orthopedic Clinics of North America, 30*(1), 81-89.

Lemay, M. A., & Crago, P. E. (1996). A dynamic model for simulating movements of the elbow, forearm, an wrist. *Journal of Biomechanics, 29*(10), 1319-1330.

Li, G., Gil, J., Kanamori, A., & Woo, S. L. (1999). A validated three-dimensional computational model of a human knee joint. *Journal of Biomechanical Engineering, 121*(6), 657-662.

Lu, Y., Pulasani, P. R., Derakhshani, R., & Guess, T. M. (2013). Application of neural networks for the prediction of cartilage stress in a musculoskeletal system. *Biomed Signal Process Control, 8*(6), 475-482. doi: 10.1016/j.bspc.2013.04.004

Machado, M., Moreira, P., Flores, P., & Lankarani, H. M. (2012). Compliant contact force models in multibody dynamics: Evolution of the Hertz contact theory. *Mechanism and Machine Theory, 53*, 99-121.

Marieb, E. N., & Hoehn, K. (2013). *Human anatomy & physiology*. Boston: Pearson.

McGinley, J. C., & Kozin, S. H. (2001). Interosseous membrane anatomy and functional mechanics. *Clinical Orthopaedics and Related Research*(383), 108-122.

Mehta, J. A., & Bain, G. I. (2004). Elbow dislocations in adults and children. *Clinics in Sports Medicine, 23*(4), 609-627, ix. doi: 10.1016/j.csm.2004.04.014

Miyake, J., Moritomo, H., Masatomi, T., Kataoka, T., Murase, T., Yoshikawa, H., & Sugamoto, K. (2012). In vivo and 3-dimensional functional anatomy of the anterior bundle of the medial collateral ligament of the elbow. *Journal of Shoulder and Elbow Surgery, 21*(8), 1006-1012. doi: 10.1016/j.jse.2011.07.018

Morrey, B. F. (2000). *The Elbow and Its Disorders*: W.B. Saunders.

Morrey, B. F., & An, K. N. (1983). Articular and ligamentous contributions to the stability of the elbow joint. *American Journal of Sports Medicine, 11*(5), 315-319.

Morrey, B. F., & An, K. N. (1985). Functional anatomy of the ligaments of the elbow. *Clinical Orthopaedics and Related Research*(201), 84-90.

Morrey, B. F., & Chao, E. Y. (1976). Passive motion of the elbow joint. *Journal of Bone and Joint Surgery (American Volume), 58*(4), 501-508.

Morrey, B. F., Tanaka, S., & An, K. N. (1991). Valgus stability of the elbow. A definition of primary and secondary constraints. *Clinical Orthopaedics and Related Research*(265), 187-195.

Murray, W. M., Delp, S. L., & Buchanan, T. S. (1995). Variation of muscle moment arms with elbow and forearm position. *Journal of Biomechanics, 28*(5), 513-525.

Nestor, B. J., O'Driscoll, S. W., & Morrey, B. F. (1992). Ligamentous reconstruction for posterolateral rotatory instability of the elbow. *Journal of Bone and Joint Surgery (American Volume), 74*(8), 1235-1241.

Netter, F. H., & Hansen, J. T. (2003). *Atlas of human anatomy* (3rd ed.). Teterboro, N.J.: Icon Learning Systems.

O'Driscoll, S. W., An, K. N., Korinek, S., & Morrey, B. F. (1992). Kinematics of semi-constrained total elbow arthroplasty. *Journal of Bone and Joint Surgery (British Volume), 74*(2), 297-299.

O'Driscoll, S. W., Bell, D. F., & Morrey, B. F. (1991). Posterolateral rotatory instability of the elbow. *Journal of Bone and Joint Surgery (American Volume), 73*(3), 440-446.

O'Driscoll, S. W., Horii, E., Morrey, B. F., & Carmichael, S. W. (1992). Anatomy of the ulnar part of the lateral collateral ligament of the elbow. *Clinical Anatomy, 5*(4), 296-303. doi: 10.1002/ca.980050406

O'Driscoll, S. W., Morrey, B. F., Korinek, S., & An, K. N. (1992). Elbow subluxation and dislocation. A spectrum of instability. *Clinical Orthopaedics and Related Research*(280), 186-197.

Olsen, B. S., Sojbjerg, J. O., Dalstra, M., & Sneppen, O. (1996). Kinematics of the lateral ligamentous constraints of the elbow joint. *Journal of Shoulder and Elbow Surgery, 5*(5), 333-341.

Olsen, B. S., Sojbjerg, J. O., Nielsen, K. K., Vaesel, M. T., Dalstra, M., & Sneppen, O. (1998). Posterolateral elbow joint instability: the basic kinematics. *Journal of Shoulder and Elbow Surgery, 7*(1), 19-29.

Olsen, B. S., Vaesel, M. T., Sojbjerg, J. O., Helmig, P., & Sneppen, O. (1996). Lateral collateral ligament of the elbow joint: anatomy and kinematics. *Journal of Shoulder and Elbow Surgery, 5*(2 Pt 1), 103-112.

Piazza, S. J., & Delp, S. L. (2001). Three-dimensional dynamic simulation of total knee replacement motion during a step-up task. *Journal of Biomechanical Engineering, 123*(6), 599-606.

Pichora, J. E., Fraser, G. S., Ferreira, L. F., Brownhill, J. R., Johnson, J. A., & King, G. J. (2007). The effect of medial collateral ligament repair tension on elbow joint kinematics and stability. *Journal of Hand Surgery, 32*(8), 1210-1217. doi: 10.1016/j.jhsa.2007.05.025

Pigeon, P., Yahia, L., & Feldman, A. G. (1996). Moment arms and lengths of human upper limb muscles as functions of joint angles. *Journal of Biomechanics, 29*(10), 1365-1370.

Podgorski, A., Kordasiewicz, B., Urban, M., Michalik, D., & Pomianowski, S. (2012). Biomechanical assessment of varus-valgus range of motion of normal elbow joint using prototype measuring device. *Ortop Traumatol Rehabil, 14*(2), 137-144. doi: 10.5604/15093492.992295

Rafee, A., Rajasekhar, C., & Shah, S. V. (2006). Simultaneous dislocation of the proximal and distal radioulnar joints. *Injury Extra, 37*(6), 233-236. doi: 10.1016/j.injury.2005.12.011

Rafehi, S., Lalone, E., Johnson, M., King, G. J., & Athwal, G. S. (2012). An anatomic study of coronoid cartilage thickness with special reference to fractures. *Journal of Shoulder and Elbow Surgery, 21*(7), 961-968. doi: 10.1016/j.jse.2011.05.015

Raghuraman, S., Schrauth, J. H., Weber, D. L., Resmer, F., Haddad-Weber, M., Breuer, F. A., . . . Haddad, D. (2013). Dynamic MR imaging of a minipig's knee using a high-density multi-channel receive array and a movement device. *MAGMA, 26*(2), 215-228. doi: 10.1007/s10334-012-0341-8

Rahman, M., Cil, A., Bogener, J. W., & Stylianou, A. P. (2016). Lateral collateral ligament deficiency of the elbow joint: A modeling approach. *Journal of Orthopaedic Research*. doi: 10.1002/jor.23165

Rahman, M., Cil, A., Johnson, M., Lu, Y., & Guess, T. M. (2014). Development and validation of a computational multibody model of the elbow joint. *Advances in Biomechanics & Applications, 1*(3), 169-185. doi: 10.12989/aba.2014.1.3.169

Rahman, M., Cil, A., & Stylianou, A. P. (2016). Prediction of elbow joint contact mechanics in the multibody framework. *Medical Engineering and Physics*, *38*(3), 257-266. doi: 10.1016/j.medengphy.2015.12.012

Raikova, R. (1996). A model of the flexion-extension motion in the elbow joint some problems concerning muscle forces modelling and computation. *Journal of Biomechanics, 29*(6), 763-772.

Regan, W. D., Korinek, S. L., Morrey, B. F., & An, K. N. (1991). Biomechanical study of ligaments around the elbow joint. *Clinical Orthopaedics and Related Research*(271), 170-179.

Safran, M., Ahmad, C. S., & Elattrache, N. S. (2005). Ulnar collateral ligament of the elbow. *Arthroscopy, 21*(11), 1381-1395. doi: 10.1016/j.arthro.2005.07.001

Schuind, F., An, K. N., Berglund, L., Rey, R., Cooney, W. P., 3rd, Linscheid, R. L., & Chao, E. Y. (1991). The distal radioulnar ligaments: a biomechanical study. *Journal of Hand Surgery, 16*(6), 1106-1114.

Shiba, R., Sorbie, C., Siu, D. W., Bryant, J. T., Cooke, T. D., & Wevers, H. W. (1988). Geometry of the humeroulnar joint. *Journal of Orthopaedic Research, 6*(6), 897-906. doi: 10.1002/jor.1100060614

Skahen, J. R., 3rd, Palmer, A. K., Werner, F. W., & Fortino, M. D. (1997). The interosseous membrane of the forearm: anatomy and function. *Journal of Hand Surgery, 22*(6), 981-985. doi: 10.1016/s0363-5023(97)80036-6

Soslowsky, L. J., Flatow, E. L., Bigliani, L. U., Pawluk, R. J., Ateshian, G. A., & Mow, V. C. (1992). Quantitation of in situ contact areas at the glenohumeral joint: a biomechanical study. *Journal of Orthopaedic Research, 10*(4), 524-534. doi: 10.1002/jor.1100100407

Spratley, E. M., & Wayne, J. S. (2011). Computational model of the human elbow and forearm: application to complex varus instability. *Annals of Biomedical Engineering, 39*(3), 1084-1091. doi: 10.1007/s10439-010-0224-y

Stormont, T. J., An, K. N., Morrey, B. F., & Chao, E. Y. (1985). Elbow joint contact study: comparison of techniques. *Journal of Biomechanics, 18*(5), 329-336.

Stylianou, A. P., Guess, T. M., & Cook, J. L. (2014). Development and validation of a multi-body model of the canine stifle joint. *Comput Methods Biomech Biomed Engin, 17*(4), 370-377. doi: 10.1080/10255842.2012.684243

Stylianou, A. P., Guess, T. M., & Kia, M. (2013). Multibody muscle driven model of an instrumented prosthetic knee during squat and toe rise motions. *Journal of Biomechanical Engineering, 135*(4), 041008. doi: 10.1115/1.4023982

Tanaka, S., An, K.-N., & Morrey, B. F. (1998). Kinematics and Laxity of Ulnohumeral Joint Under Valgus-Varus Stress. *Journal of Musculoskeletal Research, 02*(01), 45-54. doi: 10.1142/S021895779800007X

Willing, R. T., Lalone, E. A., Shannon, H., Johnson, J. A., & King, G. J. (2013). Validation of a finite element model of the human elbow for determining cartilage contact mechanics. *Journal of Biomechanics, 46*(10), 1767-1771. doi: 10.1016/j.jbiomech.2013.04.001

Willing, R. T., Lapner, M., Lalone, E. A., King, G. J., & Johnson, J. A. (2014). Development of a computational technique to measure cartilage contact area. *Journal of Biomechanics, 47*(5), 1193-1197. doi: 10.1016/j.jbiomech.2014.01.047

Wismans, J., Veldpaus, F., Janssen, J., Huson, A., & Struben, P. (1980). A three-dimensional mathematical model of the knee-joint. *Journal of Biomechanics, 13*(8), 677-685.

Zielinska, B., & Donahue, T. L. (2006). 3D finite element model of meniscectomy: changes in joint contact behavior. *Journal of Biomechanical Engineering, 128*(1), 115-123.

VITA

Munsur Rahman was born and grown up in Joypurhat, Bangladesh. He attended Kalai Moin Uddin school and finished his tenth grade in 2001. Same year, he enrolled at the Kalai Degree high school and graduated from twelfth grade with “outstanding honors” in 2003. The following year, he enrolled in Mechanical Engineering department of Bangladesh University of Engineering and Technology (BUET). In the Spring of 2009, he graduated with a Bachelor of Science degree in Mechanical Engineering.

After finishing the graduation, he started working with a famous refrigeration and air condition manufacturing company in Bangladesh. There, he had a chance to work closely with the manufacturing process and obtained a firsthand experience on industrial environment. After getting admission in University of Missouri-Kansas City (UMKC) in Spring 2012, he moved to the United States and started pursuing his M.S in Mechanical Engineering, with an emphasis in Biomechanics. He graduated with his M.S degree from UMKC in December, 2013.

In June 2014, Munsur began working on his Ph.D. at UMKC and was named the department’s Outstanding Ph.D. student in 2015. Same time, he started working at the Musculoskeletal Biomechanics Research Laboratory as a graduate research assistant and spent three full years working in the lab under the supervision of Dr. Antonis Stylianou. Throughout his academic years, he gained considerable experience at developing a musculoskeletal modeling of human joints. Upon completion of his Ph.D. degree requirements in Mechanical Engineering, Munsur plans to use his education to follow a career in biomechanics and computational modeling.